# GLASS FORMING SPIN LIQUID DYNAMICS IN THE FRUSTRATED PYROCHLORE MAGNETS $Ho_2Ti_2O_7$ AND $Dy_2Ti_2O_7$

A Dissertation

Presented to the Faculty of the Graduate School

of Cornell University

in Partial Fulfillment of the Requirements for the Degree of

Doctor of Philosophy

by

Azar Eyvazov

August 2017

GLASS FORMING SPIN LIQUID DYNAMICS IN THE FRUSTRATED PYROCHLORE MAGNETS $HO_2TI_2O_7$ AND $DY_2TI_2O_7$

Azar Eyvazov, Ph.D.

Cornell University 2017

Pyrochlore oxides with a rare earth ion in the A site have been subjects of intense research for the last two decades. In this crystal structure, the magnetic rare earth ions create a corner sharing tetrahedral network and the magnetic state of the system is determined by the combination of multitude of different interactions. $Ho_2Ti_2O_7$ and $Dy_2Ti_2O_7$, frequently called spin ices, have interesting configuration of spins at very low temperatures. Due to the geometrical frustration created by the tetrahedral lattice, the strong crystal field interactions and significant dipolar interactions between the spins, the ground state in these materials is not known to be ordered at very low temperatures. Theoretical models have proposed that the lowest energy state has two spins pointing into each tetrahedron and two spins pointing out, and the spin flips from this ground state is equated to magnetic monopole like quasi particles that should propagate through the system by flipping more spins.

We created a boundary free, superconducting toroidal experiment to detect the effects of monopole motion, or more generally the magnetization dynamics in these two systems. Our design allows as us to measure the AC susceptibility very precisely and probe the time domain relaxation of magnetization to temperatures as low as 0.6 K. The boundary free geometry removes the ambiguity of the data that comes from demagnetization effects at sample boundaries, which have to be considered when studying rod shaped sample.

The time domain magnetization relaxation experiments show Kohlrausch-Williams-Watts (KWW) stretched exponential decay of the rate of change of magnetization with time. This result disagrees with the predictions of the simple monopole model, which expects a regular exponential, however the data from all measured temperatures and for both materials show clearly show this behavior. The AC measurements performed in the temperature range 0.9-2 K and frequency range 10 Hz-100 kHz show that the AC susceptibility of both materials can be explained by the Havriliak-Negami (HN) functional form. The unified analysis of the temperature dependence of the relaxation time from time domain and frequency domain show that at low temperatures $T < 2K$ the relaxation time increases faster than Arrhenius law, and is well described by the Vogel-Tammann-Fulcher (VTF) form. These forms, KWW stretched exponential relaxation, HN susceptibility and VTF trajectory of relaxation time are dynamical identifiers of the glass forming liquids.

The liquids cooled below freezing temperature without long range crystalline ordering stay as a metastable liquid, and the functional forms described above are used to characterize such glass forming liquids. Our discoveries show that the magnetic state in $Ho_2Ti_2O_7$ and $Dy_2Ti_2O_7$ is the first example of glass forming liquid state in the magnetic systems. This is different from a common frustrated magnetic state, the spin glass, as the latter is usually associated with sharp change in AC susceptibility at some critical freezing temperature and the position of this temperature is sensitive to experimental parameters like the external field and frequency. The magnetic state in the non doped $Ho_2Ti_2O_7$ and $Dy_2Ti_2O_7$ does not show characteristics of a spin glass, instead it is better described as the glass forming liquid that one usually associated with liquid silica. Both materials have similar VTF temperature, $T_0 \approx 200mK$. We expect that at

such low temperature, the magnetic state will completely fall out of equilibrium and the system cannot reach equilibrium regardless of the wait times of the experiment. The Kramers vs non Kramers nature of spins in these materials affects the quantum mechanical transition probability between different ground state configurations. $Dy_2Ti_2O_7$ which has only Kramers doublets has lower attempt frequency than $Ho_2Ti_2O_7$ which has both singlets and doublets. The dipolar interactions which act as transverse fields in these materials are able to induce transition more efficiently (proportional to square of the field) in $Ho_2Ti_2O_7$ when compared to $Dy_2Ti_2O_7$(proportional to cube of the field). Additionally, the abundance of the monopoles in $Dy_2Ti_2O_7$ compared to $Ho_2Ti_2O_7$ leads to segmentation of the subsystems of spins and makes the magnetic liquid in $Dy_2Ti_2O_7$ more heterogeneous and more fragile.

These intriguing discoveries in systems expected to show magnetic monopole dynamics lead to a profound question, are these glass forming liquid properties the result of the monopole dynamics? Perhaps a more detailed monopole theory of the dynamics in these systems is necessary to understand such a state in magnetic pyrochlores. This is something that has to be studied both theoretically and experimentally; in the latter by going to different experimental systems, other magnetic pyrochlore oxides, to see the universality of glass forming liquids properties and by doing measurements that can directly probe the disordered state like tests of two step relaxation.

## BIOGRAPHICAL SKETCH

Azar Eyvazov grew up in Baku, Azerbaijan in the years following the collapse of USSR. As a kid he was intrigued with mathematics and science, and is told that he would annoy older people by asking too many questions about how the world worked. His first introduction to science came from his father, Huseyin Eyvazov, who was chemist by training. The science themed conversations with his father have encouraged Azar to pursue a career that promotes scientific inquiry and research.

A key person in developing Azar's interest in physics was his first physics teacher in high school, Ayhan Yaman. Despite studying with Ayhan for only two quarters, Azar was convinced that physics was the path that he wants to pursue because among all natural sciences physics is most rigorous and successful in making quantitative predictions. Soon after, Azar joined the training program for Physics Olympiads, a rigorous problem solving contest for high school students at both national and international level. The interaction with other students that he encountered in this program, the depth of topics covered and the competitive intellectual atmosphere created by the Olympiad helped Azar pick Physics as the major in college. This was a controversial decision according to his friends, as in Azerbaijan the main perspective of pursuing Physics in college is to follow up being a Physics teacher in high school.

Azar was further interested in Physics when he joined Assistant Professor Rainer Dumke in Nanyang Technological University as an undergraduate research student to work on atomic physics. The goal of the project was to develop cooling and trapping systems, and to eventually create Bose Einstein Condensate of Rubidium and Potassium atoms. The one year that Azar spent with Rainer proved very productive as he developed laser shutter circuits for con-

trol, systems to move atoms between cooling and experimental chambers and simulated the possibility of trapping and control of different elements over superconducting films. After this project Azar also tried working with Dr. Sum Tze Chien on photoluminescence of semiconductors, however it was after he joined Associate Professor Christos Panagopoulos in late 2008 when he started his journey into research in condensed matter physics. As part of his project, Azar frequently visited National Institute for Advanced Industrial Science and Tehcnology (AIST) in Tsukuba, Japan to collaborate with Dr. Isao H. Inoue to develop Field Effect Transistor devices on Strontium Titanate to explore the charge heterogeneity on the surface of these materials. This proved a very valuable experience and Azar continued to work on this project for more than two years after finishing college. Over this project Azar experienced many ingredients that go into successful research; choosing the field to study, doing key experiments, learning from other researcher's work and collaboration. These skills have been useful since then and will likely be useful for many years to come.

It was in during one of his visits to Japan that Azar applied to the graduate program in Cornell and to pleasant surprise was accepted to this program. Azar still remembers the email he received from Professor Jeevak Parpia soon after the 2011 Tohoku earthquake and was deeply touched with the attention received from Cornell Physics department. In Cornell Azar worked with Assistant Professor Michael Niemack for about a year on detection of polarization of Cosmic Microwave Background light with superconducting transition edge sensors. In January of 2014 Azar joined professor J. C. Séamus Davis and started his work on geometrically frustrated magnets $Ho_2Ti_2O_7$ and $Dy_2Ti_2O_7$. During his time in Davis group Azar learned about low temperature physics, how to maintain the system and not let it break, and how to do experiments at low

temperatures. With the skills and experience he has so far acquired, Azar aspires to go into superconducting quantum computing research after PhD.

This thesis is dedicated to my parents and my brother who have always supported me.

**ACKNOWLEDGEMENTS**

First and foremost I want to thank my advisor Séamus Davis for helping me to navigate the challenges and requirements of the graduate school and teaching me lots of useful skills necessary to conduct successful low temperature physics research. From the initial days of designing the experiments and considering even the most minute details (experience showed that even the most minute details were crucial for the final product), to actual implementation of the plan, to the construction of the experimental setup, to conducting successful experiments at cryogenic temperatures, to data analysis, and to comparison of existing bodies of data and how my work contributes to the field as a whole I can wholeheartedly say that without Séamus's guidance it would be very difficult to produce this work. The trust Séamus put on me and advise he provided helped me to become a researcher who can perform useful research in a successful collaboration.

I also would like to thank my colleagues Ethan Kassner, Anna Eyal, Ritika Dusad and Yi Xue Chong. As a senior graduate student, Ethan helped me learn lots of technical skills from operating the dilution refrigerator to successfully controlling many instruments remotely for our measurements. Anna has always lent a helping hand when I had questions about both the experimental challenges as well as discussion of the importance of our work. With frequent discussions with Anna we were able to quickly move through our analysis and formulate the physical picture important to understand our material. Both Ritika and Yi Xue have helped substantially, especially in the last one year with taking care of the lab, making sure the cryostat is always fueled (with liquid helium) and everything is running smoothly. I also would like to thank my other colleagues, Peter Sprau, Andrey Kostin, Stephen Edkins, Rahul Sharma,

Mohammad Hamidian, Freek Massee, Andrew Parmet, Tabatha Felter and Ben Pichler.

I also want to thank the Physics Department personnel Nathan Ellis, Jeff Koski, Stan McFall, Chris Cowulich and Barry Robinson, whom I have sought for all sort of advise at different times and they have always been very friendly and helpful. Many thanks to Kacey Acquilano and rest of the Physics Department administrative personnel who have always accommodated my (sometimes) conflicting semester plans and have been extremely helpful in helping me with the administrative details of graduate student life.

I want to thank my committee members, Professor Erich Mueller and Professor Kyle Shen for helpful discussions about physics that I occasionally had with them. The conversations were always eye opening and have helped me to look at my problem from different angles. I want to thank the Director of Graduate Studies, Professor Lawrence Gibbons who was always willing to sit down with me and discuss my challenges and plans.

I absolutely want to thank my family, my mother Naila Eyvazova and my brother Parviz Eyvazov. Even though we were ten thousand kilometers apart for most of my PhD and even though occasionally I couldn't even make time to properly talk to them, they have always shown sympathy and have supported me during the arduous PhD journey. My father Huseyin Eyvazov has passed away more than ten years ago, but I sure hope he would be proud of me to see me at this stage.

Last but not least I would like to thank my friends who made the graduate school experience pleasant. Times I have spent with (in no particular order) Shao Min Tan, Jennifer Chu, Jonathan Gibbons, Jennifer Grab, Jordan Moxon, Alexander Grant, Brian Koopman, Shawn Henderson, Daniyar Saparov, Hakan

Atakisi, Abdurrahman Gumus, Radwan Tajeddine, Mohamed Ismail, Turki Baroud, Mahmud Burton, Humna Awan, Eric Clay and Andrew Hocking have been my fondest memories. And they know that I will always remember them, since I have the reputation of remembering lots of metadata.

## TABLE OF CONTENTS

## LIST OF TABLES

## LIST OF FIGURES

CHAPTER 1

# SUPERCOOLED LIQUIDS AND GLASSES

Supercooled liquids are metastable states that occur when liquid is cooled below its freezing temperature but is not allowed to crystallize. When cooling is performed quickly, nucleation process necessary for generation of large crystalline regions does not occur and instead just below the freezing temperature the system retains the translational symmetry that the liquid state had. As the temperature is reduced further, the viscosity of the supercooled liquid increases exponentially, and larger and larger groups of molecules have to relax simultaneously for the system to equilibrate. At some temperature, the relaxation process becomes so slow that it becomes difficult to observe dynamics of the system under laboratory conditions. This temperature is called the glass temperature, $T_g$.

Below we first give information about relationship between viscosity and relaxation time, and how nucleation can be avoided. We then move on to talk about the defining properties of supercooled liquids, both dynamic and thermodynamic, and briefly talk about the current theories developed to study the supercooled liquids and glasses. Although spin glasses are not similar to the supercooled liquids or glasses, some brief information is given about spin glasses in the last section of this chapter.

## 1.1 Relaxation time and Viscosity

Before we develop the relationship between relaxation time and viscosity, we first look at how different systems, solids and liquids, react to applied shear. When a solid with shear modulus $G$ is subject to an external shear stress it will

deform under this force. Assuming the stress is applied in $x$ direction and the height of the solid is $y$ the shear strain experienced is

$$u_{xy} = \frac{\partial u_x}{\partial y} \tag{1.1}$$

where $u_x$ is the displacement generated in the $x$ direction. The displacement is directly proportional to the height of the solid ($u_x = \gamma y$) and this results in uniform strain over the entire height of the solid, $u_{xy} = \gamma$. The stress required to generate this is directly proportional to the strain with the the elastic shear modulus $G$ as the proportionality constant

$$\sigma_{xy} = G u_{xy} = G\gamma. \tag{1.2}$$

As long as the stress is present, the solid will have the uniform strain given by Eqn. 1.2 and this strain will not change with time because the solids don't flow. Liquids on the other hand will not maintain a uniform shape after application of external strain. If a liquid is subject to an initial strain $\gamma$ at time $t$, the stress experienced at a later time $t' > t$ will be partly relaxed,

$$\sigma_{xy} = G(t' - t)\gamma \tag{1.3}$$

where $G(t' - t)$ is the time dependent shear modulus of the liquid. This is expected to decay with time with some characteristic time scale $\tau_r$ and the simplest form is given by the Maxwell model [1]

$$G(\delta t) = G_\infty e^{-\delta t/\tau_r}. \tag{1.4}$$

At short times, $t < \tau_r$, the liquid responds to shear like a solid, however this response decays with time. The stress created when the liquid experiences a variable strain with rate $\dot{\gamma}(t)$ for time $dt$ is

$$\delta\sigma_{xy} = G(t' - t)\dot{\gamma}(t)dt. \tag{1.5}$$

Assuming a constant rate of shear strain $\dot{\gamma}$, the shear stress experienced by liquid becomes

$$\sigma_{xy}(t) = \dot{\gamma} \int_0^t G(t' - t)dt'. \tag{1.6}$$

The proportionality constant between the experienced shear stress and the rate of strain is the definition of viscosity [1], $\sigma_{xy} = \eta\dot{\gamma}$. Then, viscosity of the liquid becomes

$$\eta = \int_0^\infty G(t)dt = \tau_r G_\infty. \tag{1.7}$$

The linear relationship between the viscosity of the liquid and the relaxation time is used frequently and almost interchangeably when studying temperature dependent dynamics of liquids and supercooled liquids.

## 1.2 Nucleation vs Glass Transition

When cooled to low temperatures, liquids display a first order phase transition to the crystalline solid phase below the melting temperature, $T_m$. The crystal has lower energy than the liquid, but since it is more ordered, it also has lower entropy. At temperatures above the melting temperature, the state with higher entropy, hence the liquid phase is more stable. Below the melting temperature, the lower energy crystalline phase is the stable phase of matter. Thus, nucleation of crystalline grains is expected when the system is cooled to $T < T_m$. Supercooled liquid is the continuation of the liquid phase below the melting temperature, however it has higher entropy and consequently higher free energy, it is only a metastable state at $T < T_m$. The crystal nuclei can grow inside the supercooled liquid subject to free energy conditions. ( [1], [34], [35]) Since the crystal phase is the stable phase below $T_m$ it has lower free energy, however there will also be

positive energy cost associated with having volume crystal nucleus. This energy cost comes from the energy mismatch between the liquid and crystal phase at the phase boundary and is proportional to the surface area of the nucleus. For a nucleus of radius $R$ the Gibbs free energy difference between crystal and liquid phase is

$$\Delta G(R) = \sigma R^{d-1} - \delta g R^d, \tag{1.8}$$

where $\sigma$ is the surface tension and $\delta g$ is the free energy difference between the metastable supercooled liquid and stable crystalline solid phases

$$\delta g = g_{liq} - g_{solid}. \tag{1.9}$$

At the melting temperature $\delta g = 0$ and it is often assumed to increase linearly with decreasing temperature below $T_m$ [36]

$$\delta g = \frac{\delta h}{v}\left(1 - \frac{T}{T_m}\right) \tag{1.10}$$

where $\delta h$ is the molar enthalpy of fusion and $v$ is molar volume of the crystal. According to Eqn. 1.8 when the nucleus is small, energy cost associated with the surface tension is big compared to the energy gain from nucleation. At large sizes however, free energy saved from developing a crystal becomes significant and the nucleus is stable. The critical size and the energy barrier to the creation of crystal nucleus is

$$R_c = \frac{\sigma}{\delta g}\left(1 - \frac{1}{d}\right) \tag{1.11}$$

$$\Delta G(R_c) = \frac{\sigma^d}{d\delta g^{d-1}}\left(1 - \frac{1}{d}\right)^{d-1}. \tag{1.12}$$

At the melting temperature, $\delta g = 0$ and the barrier for the formation of nucleus becomes infinitely large. This is because at this critical temperature, both liquid and crystal phases have the same free energy and the system doesn't save energy when it becomes crystal, but there is still nonzero energy cost coming from

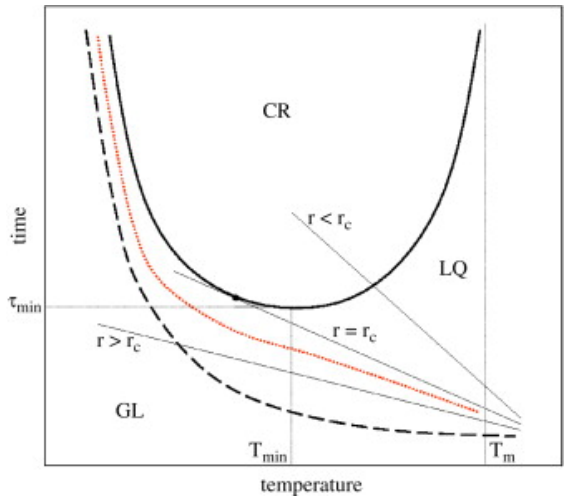


Figure 1.1: Important time scales for the supercooled liquid below the melting temperature, $T_m$. The nucleation time is depicted by solid black line; it becomes infinitely large both at the melting temperature and at absolute zero and has a minimum at $T_{min}$. The relaxation time of the system is very small near $T_m$ but rises drammatically as the temperature is lowered. If the system is cooled slower than a critical linear rate, $r < r_c$, the system has enough time to develop a stable nucleus and becomes a crystal. The critical rate $r_c$ is determined by the shape of the nucleation time profile of the system. At linear cooling rates faster than $r_c$, at some temperature the liquid is unable to relax and becomes frozen in a glass state. With nonlinear cooling rates (dotted red line) it is theoretically possible to cool the system to arbitrarily low temperatures while maintaining the metastable supercooled liquid phase. From ref. [1].

the surface tension term.

At $T < T_m$ the system has to get over the free energy barrier given by Eqn. 1.12. With Arrhenius like activation process coming only from thermal fluctuations of the system, the nucleation time becomes

$$\tau_n = \tau_0 \exp\Big(\frac{\Delta G(R_c)}{k_B T}\Big) = \tau_0 \exp\Big(\frac{\sigma^d}{d\delta g^{d-1} k_B T}\Big(1 - \frac{1}{d}\Big)^{d-1}\Big). \tag{1.13}$$

At $T = T_m$, $\delta g = 0$ and the nucleation time is infinitely large. Additionally at very low temperatures ($T \to 0$), there is not enough thermal energy to carry the nucleation process over the energy barrier and nucleation time is again infinite (Fig. 1.1). The minimum nucleation time, $\tau_{min}$, will happen at some intermediate

temperature $T_{min}$. As the system is cooled at a linear rate, the slowest rate at which nucleation can be avoided will be related to the minimum nucleation time

$$r_c \sim \frac{1}{\tau_{min}}. \tag{1.14}$$

If the cooling rate is slower than this, the system has enough time to develop a stable crystal nucleus. The relaxation time of the supercooled liquid is very small in the vicinity of $T_m$ but rises sharply as the temperature is lowered. At cooling rates $r > r_c$, the system eventually is unable to relax and falls out of equilibrium. This is identified as the glass temperature and is determined by the cooling rate besides material parameters. With nonlinear cooling scheme (red line in Fig. 1.1) it is theoretically possible to avoid both crystallization and glass transition and maintain the metastable supercooled liquid phase down to very low temperatures. However in reality, in many supercooled liquids the relaxation time becomes infinitely large at nonzero temperatures (section 1.4) and the liquid is forced to either crystallize or completely fall out of equilibrium.

## 1.3 Thermodynamic properties

As discussed above, when the liquid is cooled below its melting temperature, the stable state is the crystalline solid. When the liquid crystallizes, number of thermodynamic quantities characterizing the system change discontinuously at the melting temperature. Fig. 1.2a shows how specific volume $V_{sp}$ of a liquid depends on temperature below $T_m$ [2]. When the liquid crystallizes, the specific volume usually drops to a lower value. The specific volume of the supercooled liquid changes at a faster rate than the crystal and can be extrapolated from the specific volume of the liquid above the melting temperature. As the tempera-

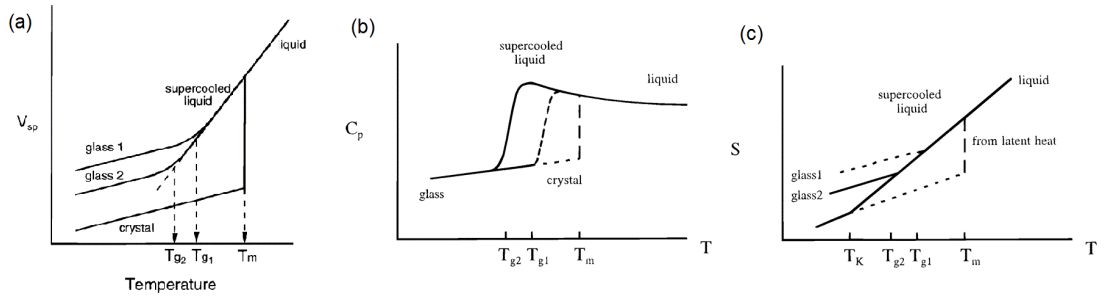


Figure 1.2: The specific volume (a), heat capacity (b) and entropy (c) of the liquid below the melting temperature. When liquid crystallized, all three of these quantities drop to a lower value discontinuously. For the metastable supercooled liquid, specific volume decreases continuously and heat capacity follows the same trend as the liquid preceding the supercooled liquid. However, around the glass temperature the liquid is unable to relax and becomes frozen in one of the metastable states. This results in sharp decrease of heat capacity to the value comparable to that of the crystal. The specific volume and entropy of the glass have the same temperature dependent trend as the crystal. The temperature at which glass transition occurs depends on the cooling rate, $T_{g1}$ corresponds to faster cooling rate (dashed line in (b) and (c)) compared to $T_{g2}$ that corresponds to slower cooling rate. From [2].

ture is lowered, the viscosity of the liquid becomes larger and larger. At some temperature the molecules move so slowly that they don't have enough time to rearrange to find the equilibrium $V_{sp}$ and the observed specific volume will begin to deviate from this equilibrium value. Below this temperature, the specific volume will continue to decrease, however the thermal expansion coefficient is significantly reduced compared to the liquid. In the glassy state, the thermal expansion coefficient is comparable to that in the crystalline state, because in both cases the expansion is dominated by thermal vibration of atoms. Depending on the cooling rate, the system will be locked in one of the metastable state and become glass at different temperature. In Fig. 1.2a, glass 1 is obtained at faster cooling rate than the rate used to realize the glass 2.

The crystal has lower thermal expansion coefficient than the liquid, and when the liquid crystallizes its heat capacity will drop sharply to a lower value. Ad-

ditionally, since the crystal is a more ordered phase, the entropy of the crystal will also be smaller than the metastable supercooled liquid (Fig. 1.2b,c. As the temperature is lowered further, the entropy of the supercooled liquid decreases faster than the entropy of the solid since the liquid has higher heat capacity. At first sight, it seems that if this trend can continue to low enough temperatures, at some temperature $T_K$ the entropy of the supercooled liquid can eventually become smaller than the entropy of the crystal, the more ordered state. This seeming "entropy crisis" was originally pointed Kauzmann to draw attention to the properties of liquids deep in the supercooled liquid state. [37] However, this entropy crisis is usually avoided by the fact that experiments usually don't have enough time to wait until the system can realize the equilibrium supercooled liquid state at every temperature when the system is cooled. Eventually the relaxation time becomes so large that the system gets trapped in one of the metastable states. At this point the thermal expansion coefficient decreases sharply and consequently the heat capacity of the liquid is reduced to a value comparable to that of the crystal. This is a different definition of the glass temperature; below this temperature the entropy of the glass changes at the same rate as the entropy of the crystal and the entropy crisis is avoided. Again, by following a cooling trajectory with slower rate (solid line in Fig. 1.2b,c) the temperature at which the glass transition will occur can be reduced and the system can be kept in the supercooled liquid phase at incrementally lower temperature.

A natural question to ask at this point is, 'Then can't we cool the system so slowly that it will never become a glass, but will remain supercooled liquid down to indefinitely low temperatures? How will the Kauzmann paradox be resolved then?' The answer to this question has two parts. Firstly, if the cool-

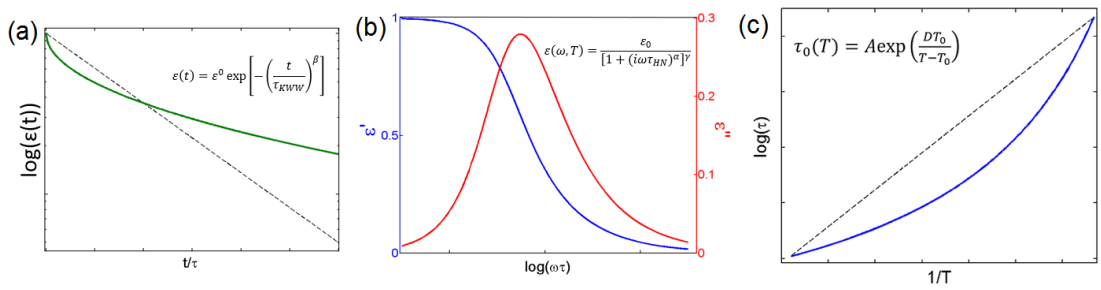


Figure 1.3: Dynamical properties of supercooled liquids. (a) In the vicinity of the glass transition, the time dependent response function deviates from the simple exponential decay and an extra parameter, the stretching exponent has to be included to explain the relaxation process. (b) AC response function of supercooled liquid also becomes different from Debye form. Exponents $\alpha$ and $\gamma$ are included to account for assymmetry and broadening compared to the prediction of Debye form of the peak in the imaginary part of susecptibility. (c) Relaxation time for a general supercooled liquid deviates from Arrhenius type exponential relaxation, and becomes infinitely large at finite temperature $T_0$. From [3].

ing rate is not fast enough, at some temperature the system will have enough time to develop stable nucleus and become crystal (Fig. 1.1 in section 1.2). So a nonlinear cooling scheme has to be employed both to avoid the nucleation and to give system enough time at low temperatures to relax and maintain the metastable supercooled liquid state. However, the second part of the answer to the question above is that, in real systems the relaxation time at low temperatures increases faster than exponentially and can become infinitely large at finite temperatures. This empirical fact, discussed in the next two sections, makes it impossible to maintain a supercooled liquid at arbitrarily low temperatures.

## 1.4 Dynamical Properties

In the vicinity of glass transition, the time dependent response function, which can be electric polarizability, the dielectric constant or stress induced after ap-

plied strain, of the liquid deviates from a simple exponential form (Fig. 1.3a).

$$\varepsilon(t) = \varepsilon^0 \exp\Big[ -\Big(\frac{t}{\tau_{KWW}}\Big)^{\beta}\Big] \tag{1.15}$$

This was first observed in 1847 by Kohlrausch when he was studying the decay of the residual charge on Leyden jar. [38] More recently, this type of relaxation function has been observed in many glass formers [39] and is commonly known as Kohlrausch-Williams-Watts relation. For glass formers, the exponent $\beta$ in Eqn. 1.15 is less than unity and can be as low as $3/7$ for some systems. At long times the relaxation process described by a stretched exponential with $\beta < 1$ is slower than simple exponential displayed by liquids at higher temperatures. This slowing down comes from spatial heterogeneity in the system that arises when the system is unable to relax as a whole and different parts of the system develop distinct relaxing domains. ( [1], [2], [6])

In the frequency domain, the stretched exponential form in Eqn. 1.15 corresponds to the Havriliak-Negami form (Fig. 1.3b). ( [38], [1])

$$\varepsilon(\omega) = \frac{\varepsilon_0}{[1 + (i\omega\tau_{HN})^{\alpha}]^{\gamma}} \tag{1.16}$$

The Havriliak-Negami form is the more general form of Debye ($\alpha = \gamma = 1$), Cole-Cole ($\gamma = 1$) and Davidson-Cole ($\alpha = 1$) forms. ( [40], [41]) It was developed to accurately explain the AC permittivity of polymers and supercooled liquids, and the exponents $\alpha$ and $\gamma$ account for the broadening of the width and asymmetry of the peak in imaginary part of AC response function. Analytic form of Fourier transform of Eqn. 1.15 doesn't exist for $\beta \neq 1/2$, however both KWW and HN forms can be generated in a model with a distribution of relaxation times

$$\exp\left[ -\Big(\frac{t}{\tau_{KWW}}\Big)^{\beta}\right] = \int_0^{\infty} \exp\left( -\frac{t}{\tau}\right) G(\ln\tau) d(ln\tau) \tag{1.17}$$

$$\frac{1}{[1 + (i\omega\tau_{HN})^{\alpha}]^{\gamma}} = \int_0^{\infty} \frac{1}{1 + i\omega\tau} G(\ln\tau) d(ln\tau). \tag{1.18}$$

The distribution function $G(\ln\tau)$ can be obtained from relaxation in one domain and used to generate the form in the other domain. This allows us to link the parameters of the two forms with the following equations [42]

$$\ln\left(\frac{\tau_{HN}}{\tau_{KWW}}\right) = 2.6(1-\beta)^{0.5}\exp(-3\beta) \tag{1.19}$$

$$\alpha\gamma = \beta^{1.23}. \tag{1.20}$$

As the glass temperature is approached, the relaxation time of the liquid increases faster than exponential (Fig. 1.3c). This deviation from Arrhenius-type activation is well captured by the Vogel-Tammann-Fulcher form

$$\tau_r(T) = \tau_0 \exp\left(\frac{DT_0}{T-T_0}\right) \tag{1.21}$$

and explicitly predicts the divergence of the relaxation time at some finite temperature $T_0$. The parameter $D$ here is known as the fragility parameter; it is small for fragile supercooled liquids and polymers, and can be very large for strong glass formers like $SiO_2$. For strong supercooled liquids like $SiO_2$ and $GeO_2$, the temperature dependence of the relaxation time is almost Arrhenius-like (Fig. 1.4a). This corresponds to very small VTF temperature $T_0$, and the glass transition happens at relatively high temperatures compared to the VTF temperature. [43] Fragile liquids on the other hand have greater deviation from Arrhenius and have relatively large VTF temperature that for some materials like lithium acetate is comparable to the glass temperature. The fragility of the liquid depends on the spatial heterogeneity of the system and greater the density of metastable energies in the energy landscape more fragile the liquid is (Fig. 1.4b). ( [6], [7], [8]). The greater number of metastable states in fragile liquids manifests itself as different regions relaxing with different relaxation times.

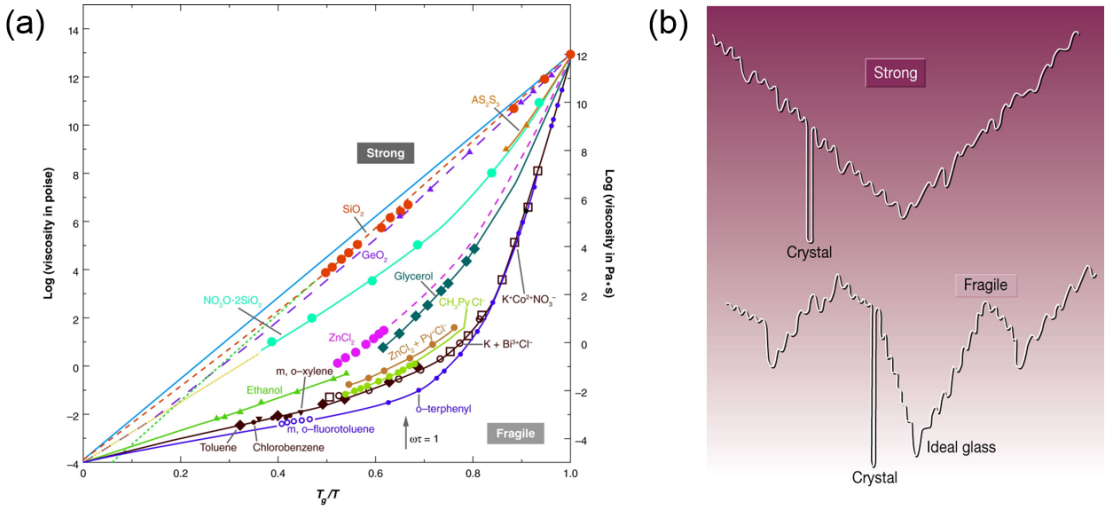


Figure 1.4: (a) The Angell plot for a number of supercooled liquids. ( [4], [5]) For strong liquids the temperature dependence of relaxation time is effectively Arrhenius type, however for fragile liquids greater deviation from Arrhenius law is seen. (b) Energy landscapes for strong and fragile supercooled liquids. Strong supercooled liquids have lower density of metastable energy levels compared to fragile liquids. ( [6], [7], [8])

.

Even if the individual relaxation times follow the Arrhenius form, the empirically observed relaxation time which is average of all the relaxation processes in the system will deviate from Arrhenius form in fragile liquids.

## 1.5 Theories of Supercooled Liquids

### 1.5.1 Adam-Gibbs Theory

The first successful attempt at explaining the relaxation processes of supercooled liquids came from Adam and Gibbs in 1965. [44] In their theory, Adam and Gibbs assume the relaxation of a group of molecules, defined as cooperatively rearranging region, over some characteristic energy barrier, $\Delta\mu$. The tran-

sition probability is then

$$P(T) = A \exp(-z\Delta\mu/k_B T) \tag{1.22}$$

where $z$ is the number of molecules in the cooperatively rearranging region. The dominant contribution to the probability will come from the smallest cooperatively rearranging region with size $z_0$ and the transition probability for this fastest transition is

$$P(T) = A' \exp(-z_0\Delta\mu/k_B T. \tag{1.23}$$

The contribution to the transition probability of all other regions with size $z > z_0$ simply modifies the prefactor of the exponent which was changed from $A$ in Eqn. 1.22 to $A'$ in Eqn. 1.23.

The configurational entropy $S_c$ of the whole system can be written as the product of the configurational entropy of a small region $s_c$ and number of such regions in the system $N$ under the assumption that all the regions are equivalent and independent of each other, $S_c = Ns_c$. Then the configurational entropy of a region will be related to the number of configurations in the system via

$$S_c = k_B \ln \Omega_c \tag{1.24}$$

$$s_c = S_c/N = k_B \ln(\Omega_c^{1/N}) \tag{1.25}$$

The configurational entropy of an individual region also depends on the size of the region $z$. Assuming the density of such regions is $z$ in some characteristic size for the number of molecules in the system, like Avogadro's number, $s_c$ becomes

$$s_c = k_B \ln(\Omega_c^{z/N_A}) \tag{1.26}$$

At some temperature smallest possible size for the cooperatively rearranging region will be characterized by some critical configurational entropy such that

$s_{c,0} = k_B \ln(\Omega_c^{z_0/N_A}) = S_c z_0/N_A$. Then the relationship between critical size of the region and configurational entropy of the system is derived to be

$$z_0 = N_A s_{c,0}/S_c. \tag{1.27}$$

Combining this with the expression for transition probability in Eqn. 1.23 we arrive at the well known Adam-Gibbs equation [44]

$$P(T) = A' \exp(-\Delta\mu s_{c,0}/k_B T S_c) = A' \exp(-C/TS_c). \tag{1.28}$$

The relaxation time of the system is inversely proportional to the transition probability, $\tau_r(T) \propto 1/P(T)$. This expression was originally used to explain the temperature dependence of the relaxation time of polymers, which follows Williams-Landell-Ferry (WLF) equation. [44] WLF equation is mathematically identical to the Vogel-Tammann-Fulcher equation used for supercooled liquid. ( [2], [6], [4]) The assumption used in deriving the Vogel-Tammann-Fulcher form from Eqn. 1.28 is that the heat capacity difference between the supercooled liquid state and the crystal is inversely proportional to the temperature. This is frequently the case, especially in strong supercooled liquids. [5] The configurational entropy is given as the entropy difference between the supercooled liquid and the crystal (difference between the solid and dashed lines in Fig. 1.2c)

$$S_c = \int_{T_K}^{T} \frac{\kappa}{T}\frac{dT}{T} = \kappa(\frac{1}{T_K} - \frac{1}{T}) \tag{1.29}$$

With this form for the configurational entropy, the relaxation time predicted by Adam-Gibbs theory becomes

$$\tau_r = \tau_0 \exp\Big(\frac{CT_K}{\kappa(T - T_K)}\Big). \tag{1.30}$$

This is precisely the same as the empirical equation suggested by VTF relation, and identifies the Kauzmann temperature, the temperature at which entropy

crisis would occur if the system could be maintained in metastable state down to arbitrarily low temperatures, with $T_0$ the temperature at which relaxation in the system has halted and the system cannot maintain the supercooled liquid state any more and has to freeze into a glass. This requirement lifts any danger of entropy crisis that could possibly arise at Kauzmann temperature. In fact, there is large body of empirical evidence that Kauzmann temperature $T_K$ and the VTF temperature $T_0$ agree well for significant number of supercooled liquids. ( [7], [43]) Additionally, the equation 1.30 relates the fragility parameter $D$ as being inversely proportional to the heat capacity difference between the supercooled liquid and crystal. Again, this trend is seen in thermodynamic and dynamic experiments on supercooled liquids, the strong supercooled liquids (large $D$) have smaller jump in heat capacity upon glass transition compared to the fragile (small $D$) supercooled liquids. [5]

### 1.5.2 Modern theories

Mode-coupling theory (MCT) was developed to explain divergence of correlation times when there is no divergence of correlation length or susceptibility at Kauzmann temperature. [2] It is based on nonlinear feedback mechanism of density correlations in a liquid which couple to secondary processes and allow relaxation processes occur even below the critical temperature associated with viscous slowdown $T_c$ and can be greater than $T_g$. The additional couplings in the system complicates the observation of any criticality at $T_c$. The main success of mode coupling theory has been the detailed prediction of autocorrelation function $\phi(t)$ in supercooled liquids; at short times $\phi(t)$ decays with a fast microscopic process as a power law ($\phi(t) \sim A_1 + B_1 t^{-a}$) which at intermediate

times becomes a power law with different exponent ($\phi(t) \sim A_2 - B_2 t^b$) and at long times it is well explained by Kohlrausch-Williams-Watts stretched exponential ($\phi(t) \sim \exp(-(t/\tau)^\beta)$). [45] This list of relaxations have been observed in supercooled liquids with light scattering and neutron scattering. ( [46], [47])

Random First Order Transition (RFOT), also known as mosaic theory uses the fact that when the relaxation process becomes so slow that large regions of the system cannot equilibrate as a whole, different parts of the system will be found in different states. ( [1], [5]) The free energy cost of this effective domain formation will be proportional to the surface tension of the system and the area of the boundary, $\Delta F = \sigma L^\rho$. For a system in $d$ dimensions, the surface area is expected to be proportional to $L^{d-1}$ however, with renormalization group method it was found that $\rho = d/2$ is a better choice for the effective surface area between different regions. [48] This extra free energy is balanced by the fact that larger regions will have larger configurational entropy and free energy can be reduced if the system rearranges into a collection of smaller regions. The free energy is then given by

$$F(L) = \sigma L^{d/2} - T s_c L^d \tag{1.31}$$

where $s_c$ is the configurational entropy of a single region and is normalized by the volume of the system. Derivation of the energy barrier for the rearrangements follows the similar procedure as that used in section 1.2 and at critical size of the rearranging regions

$$L_c \sim \left(\frac{\sigma}{2T s_c}\right)^{2/d} \tag{1.32}$$

is given by

$$F_b = \frac{\sigma^2}{4T s_c}. \tag{1.33}$$

Similar to Adam-Gibbs theory, the RFOT also predicts VTF relation for relaxation time when the form of configurational entropy is assumed to follow

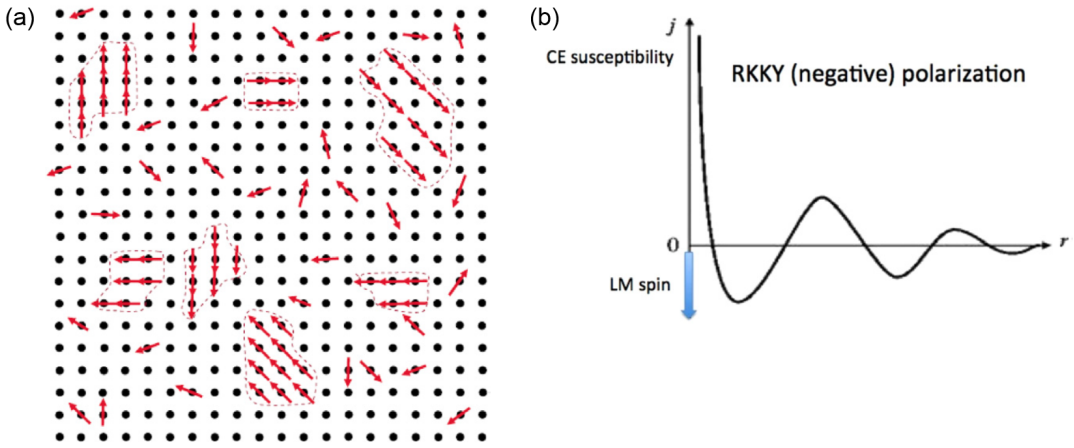


Figure 1.5: (a) Random magnetic spins in a nonmagnetic metallic matrix. (b) RKKY between magnetic ions in a metal interaction mediated by itinerant electrons. From [9], [10]

Eqn. 1.29. It was shown that mode coupling theory that makes detailed predictions about the dynamical properties of supercooled liquids and the random first order transition theory are equivalent descriptions of supercooled liquids. [49]

## 1.6 Spin Glasses

Spin glasses result when random magnetic interactions coupled with competition do not allow the system develop a long range order at low temperatures. [9] These systems have been actively studied since 1970s and have seen application in diverse areas like neural networks, vortex glass in high $T_c$ superconductors, econometrics and protein folding. [10] Here the combination of competing interactions, randomness and frustration can create a situation where it is impossible to satisfy all of the energy minimization conditions among the magnetic con-

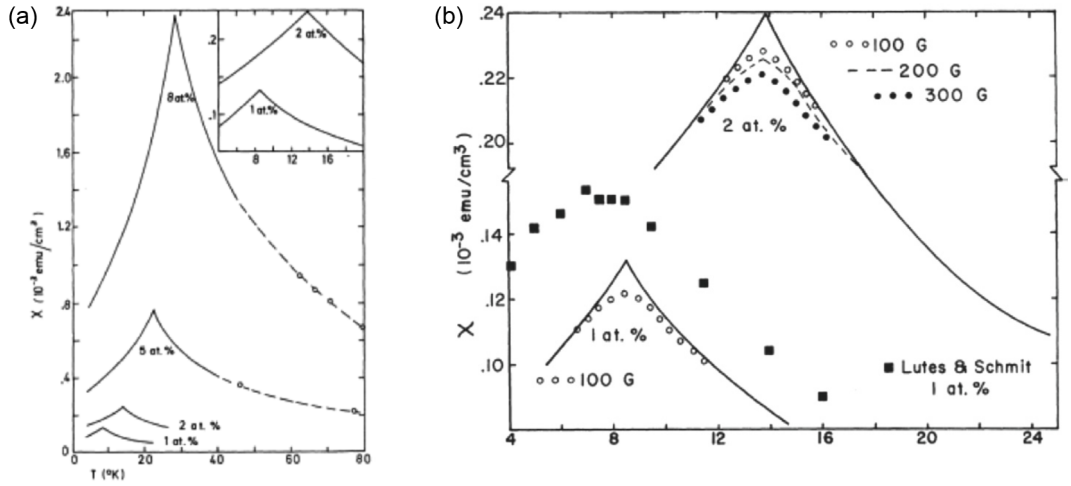


Figure 1.6: (a) Real part of AC susceptibility in AuFe alloy. The position of the cusp changes with the density of Fe ions. (b) The sharp cusp smears out with increasing external field. [11]

stituents of the system. The archetypal spin glass systems are the nonmagnetic metals doped with magnetic ions like iron doped gold (AuFe) or manganese doped copper (CuMn) (Fig. 1.5a). Here the nonmagnetic matrix is mildly doped (1-2%) with magnetic ions. Interactions between the magnetic ions in the metallic matrix is mediated by the itinerant electrons and is given by RKKY interaction (Fig. 1.5b). [9] This interaction changes sign depending on the distance between the magnetic sites and different sites can have either antiferromagnetic or ferromagnetic interaction depending on how far apart they are. The frustration combined with randomness associated with doping creates a system ripe for observation of spin glass characteristics.

Despite lack of long range ordering, the spin glass transition at low temperatures is identified as a phase transition. The real part of AC susceptibility exhibits a cusp at the SG temperature $T_{sg}$ the position and height of which depends on the density of magnetic impurities (Fig. 1.6a). However, this sharp cusp in AC susceptibility smears out with external magnetic field (Fig. 1.6b),

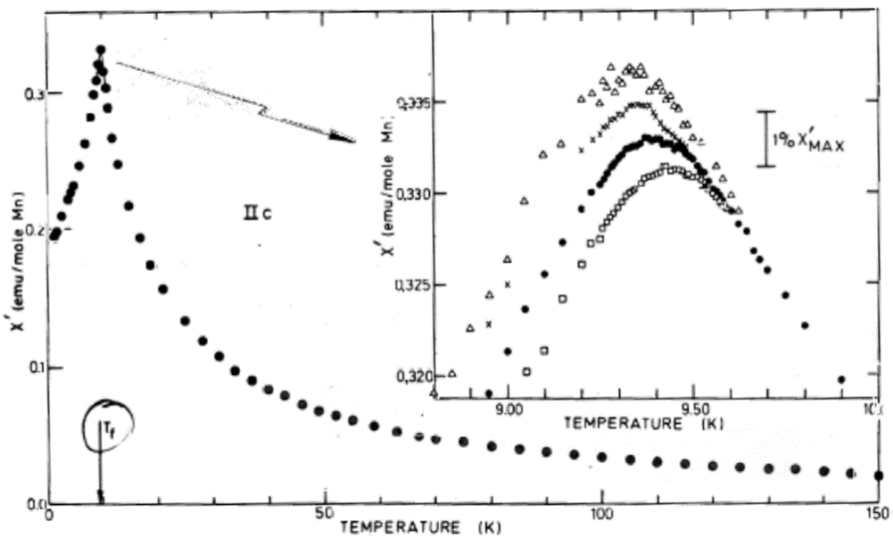


Figure 1.7: Real part of AC susceptibility in CuMn. (inset) Shift in the position of the cusp with the frequency of external field. Sensitivity of the spin glass transition temperature to the frequency of excitation gives information about the strength of interactions in the spin glass. [10]

which necessitates low fields to detect the cusp associated with the spin glass transition. The position of the cusp, i.e. the spin glass temperature depends on the frequency of external field (Fig. 1.7) and the amount of this shift gives information about the strength of interactions in the spin glass. The normalized shift $\Delta T_{sg}/T_{sg} \ln \omega$ is small for strongly interacting spin glasses. For the CuMn system in Fig. 1.7 this number is only 0.005.

The spin glass temperature is also the highest temperature where the difference between the measurement of susceptibility under field cooled or zero field cooled protocols becomes apparent. The zero field cooled (ZFC) protocol corresponds to cooling the system down in the absence of external field and measuring the susceptibility while warming up. After reaching a temperature $T > T_{sg}$ the susceptibility is measured while cooling which gives the field cooled (FC) susceptibility. The FC susceptibility is the equilibrium susceptibility of the system and ZFC susceptibility agrees with FC susceptibility at temperatures above

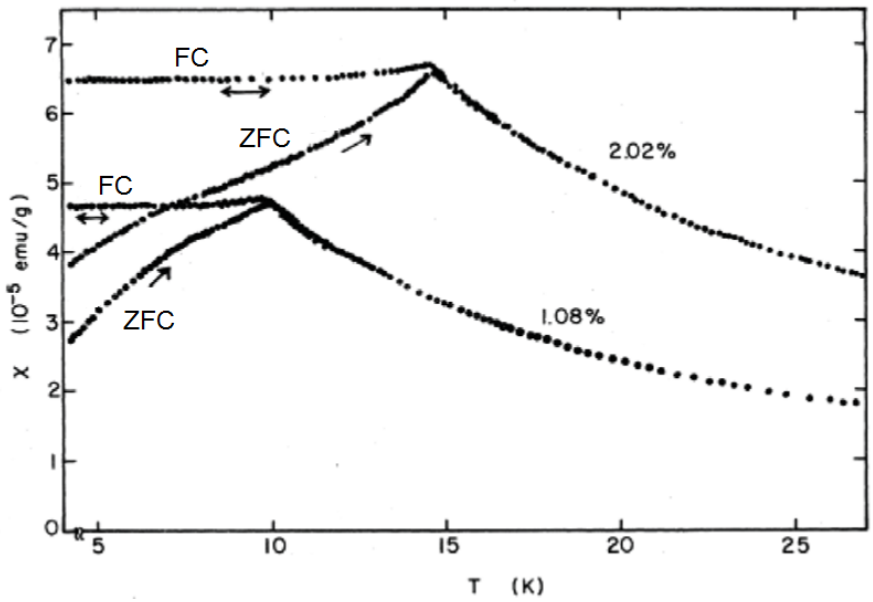


Figure 1.8: Difference between field cooled and zero field cooled susceptibility in CuMn at external field 6 Oe. At spin glass temperature, ZFC susceptibility deviates from FC susceptibility. However when the system is made to wait at external field after being cooled down without an external field (ZFC protocol) the susceptibility slowly creeps up to the FC value (aging). ( [12], [10])

spin glass temperature (Fig. 1.8). Below $T_{sg}$, the ZFC susceptibility is smaller than FC susceptibility, however if the system is made to wait at some temperature $T < T_{sg}$ under applied field after ZFC protocol, the susceptibility slowly creeps up toward the FC susceptibility. This is known as the aging process in the spin glasses.

The spin ices discussed mainly in the next chapter have large geometric frustration, but the spins in these materials are at well defined lattice points. The randomness which is key for the spin glass phase is usually absent in spin ices. However, it was demonstrated that randomness associated with slight doping of both rare earth and transition metal sites can create spin glass phase in the spin ices. ( [50], [51], [52])

CHAPTER 2

**SPIN ICE**

## 2.1 Pyrochlore Oxides

Pyrochlore structure is named after $(Na,Ca)_2Nb_2O_6(OH,F)$ that turns green when heated. The oxides are usually described by a general formula $A_2B_2O_6O'$ where A are the rare earth ions, B are the transition metal ions and O and O′ are oxygen sites. The A ions sit at 16d lattice sites, B ions sit at 16c sites, 6 of the oxygens sit at 48f sites and one O′ occupies 8b site. [53] The rare earth ions create a tetrahedral network while the transition metal ions form an octahedral lattice (Fig. 2.1). [54] The large magnetic ions usually have complicated interactions determined by detailed splitting of energy levels due to crystal fields. These lead to rich collection of phases exhibited by rare earth pyrochlore oxides like

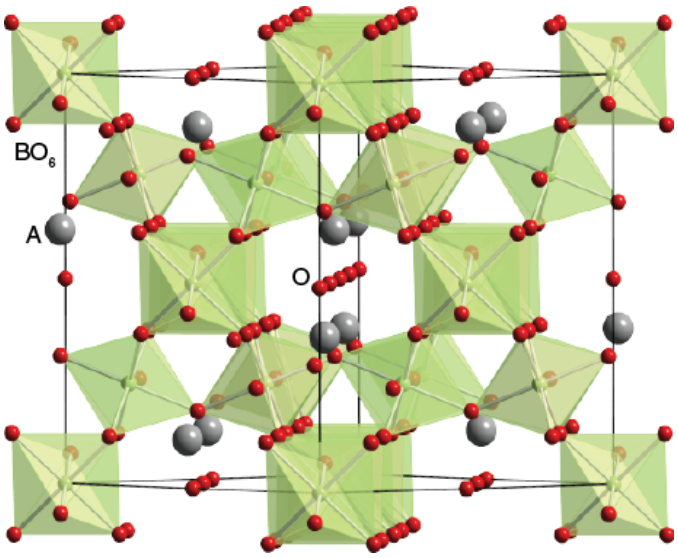


Figure 2.1: Crystal structure of pyrochlore oxide with general formula $A_2B_2O_7$. Rare earth A ions create tetrahedral network, while transition metal B atoms organize into corner sharing octahedra. [13]

long range ordered phases in $Er_2Ti_2O_7$, $Gd_2Ti_2O_7$, $Tb_2Sn_2O_7$, spin glass phases in $Y_2Mo_2O_7$, $Tb_2Mo_2O_7$, spin ices $Dy_2Ti_2O_7$, $Ho_2Ti_2O_7$ (which are subjects of this thesis) and spin liquids $Yb_2Ti_2O_7$, $Tb_2Ti_2O_7$. [54]

## 2.2 $Dy_2Ti_2O_7$ and $Ho_2Ti_2O_7$: Before They Were Spin Ice

The characterization of $Dy_2Ti_2O_7$and $Ho_2Ti_2O_7$was originally performed in 1960s and 1970s. ( [55], [56], [57] These magnetic systems have also shown interesting ferroelectric ( [58], [59]), magneteoelectric ( [60], [61], [62]) and spin glass behavior under doping of both A or B sites ( [51], [52], [50]). The ground state of both systems is a doublet with spins maximally aligned along the local $z$ direction, $m_S = \pm S$. This doublet is enforced by the strong crystal field interactions. [14] The energy splitting between the ground state doublet and the first excited state is 380 K in $Dy_2Ti_2O_7$and 240 K in $Ho_2Ti_2O_7$(Fig. 2.2). ( [63], [64], [65], [66]) Because of this large energy barrier between the ground state and the excited states, at low temperatures only the ground state doublet has to be included to study the properties of these systems. $Dy_2Ti_2O_7$ has rare earth ions with spin $S = 15/2$ and the energy levels are all grouped into doublets, while $Ho_2Ti_2O_7$has integer spin $S = 8$ and has both singlet and doublet energy levels (Fig. 2.2). One final difference that should be included is that, stable isotopes of Holmium have significant nuclear spin and the nuclear hyperfine interaction frequently has to be considered to analyze the properties of $Ho_2Ti_2O_7$ like low temperature heat capacity. ( [55], [57]) This has proven to be very important for correct analysis of $Ho_2Ti_2O_7$data. [16] $Dy_2Ti_2O_7$ on the other hand doesn't have any stable isotopes of $Dy^{3+}$ with significant nuclear spins and has been free of this complication. The direct evidence for the influence of nuclear spins

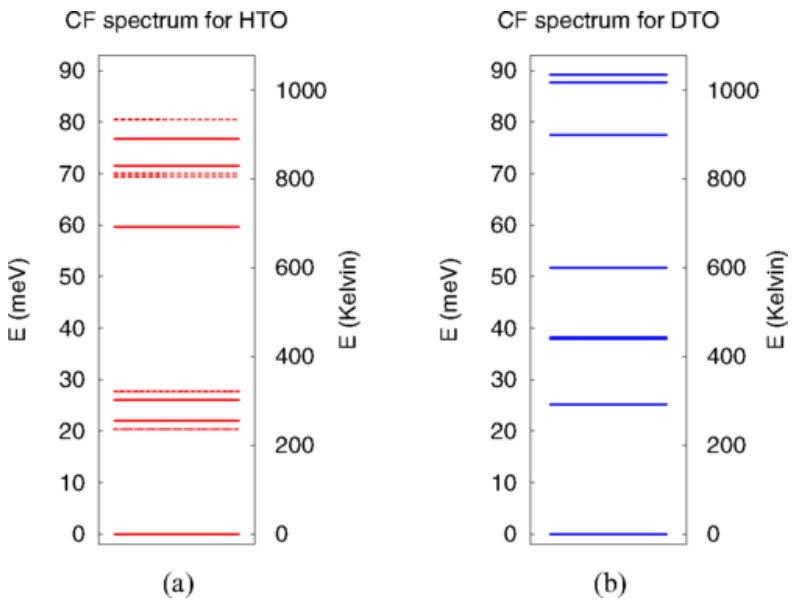


Figure 2.2: Energy levels of the rare earth ion in (a) $Ho_2Ti_2O_7$and (b) $Dy_2Ti_2O_7$. $Dy_2Ti_2O_7$has spin $S = 15/2$ and all the energy levels are grouped into doublets due to Kramers degeneracy. In $Ho_2Ti_2O_7$however, the spin is $S = 8$ and there are both singlet and doublet energy levels. The ground state doublet is separated from higher states by the energy barrier ~300 K such that at low temperatures, both the dynamic and static properties are determined by the ground state doublet in both materials. From [14]

in $Ho_2Ti_2O_7$ compared to $Dy_2Ti_2O_7$ was observed in neutron backscattering experiments. [67]

## 2.3 Spin Ice

The original experimental that coined the term spin ice was the measurement of heat capacity of $Dy_2Ti_2O_7$, and especially the entropy of the low temperature state calculated from this heat capacity. [15] Fig. 2.3a depicts the heat capacity of $Dy_2Ti_2O_7$at temperatures below 12 K. This heat capacity is used to calculate the entropy of the magnet at low temperatures from thermodynamic relation

$$S = \int \frac{C_p}{T} dT. \tag{2.1}$$

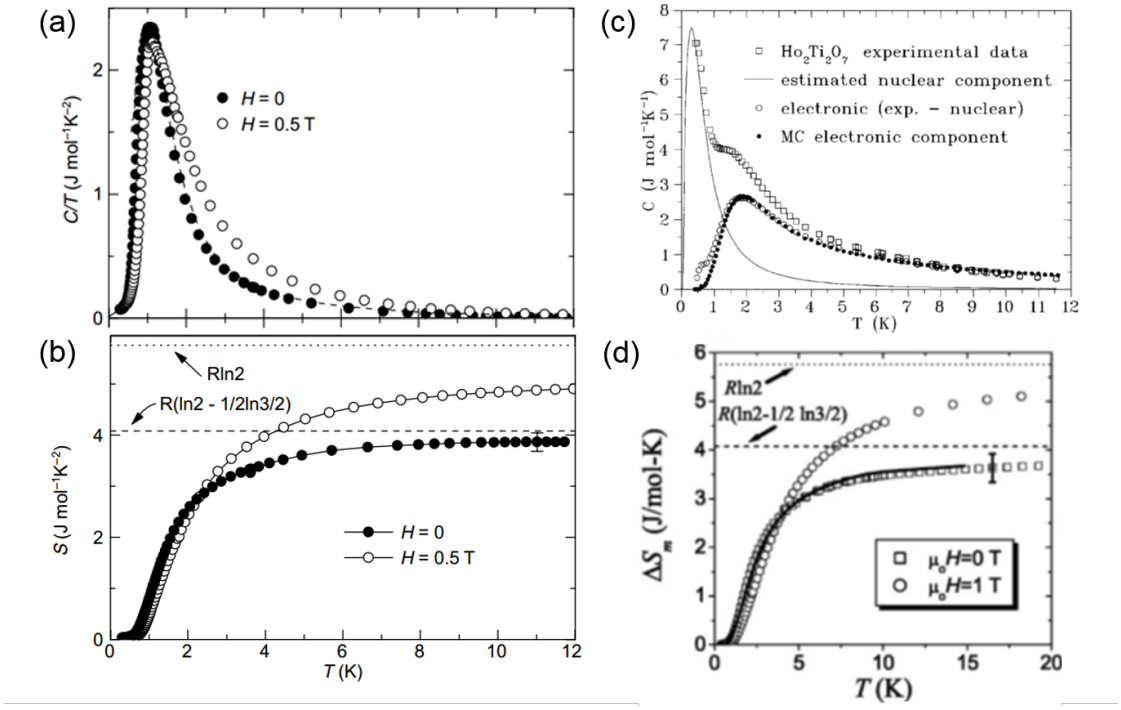


Figure 2.3: (a) Heat capacity of $Dy_2Ti_2O_7$measured at $T$¡12 K and (b) the entropy obtained from the measured heat capacity $S = \int C_p/T dT$. (c) Heat capacity of $Ho_2Ti_2O_7$at similar temperature range. For $Ho_2Ti_2O_7$, the nuclear contribution of heat capacity has to be removed first to estimates the magnetic heat capacity. (d) The entropy of the magnetic state obtained from magnetic heat capacity. From [15], [16], [17].

The change in entropy of $Dy_2Ti_2O_7$from intermediate temperature to low temperatures is shown in Fig. 2.3b and deviates from the simple assumption of $S = R\ln 2$ that would corresponds to the full entropy of the doublet ground state at high temperature.

Similar measurements of missing entropy were performed on $Ho_2Ti_2O_7$ as well. ( [16], [17]) Heat capacity of $Ho_2Ti_2O_7$is shown in Fig. 2.3c. When compared to the heat capacity of $Dy_2Ti_2O_7$in Fig. 2.3a, we see that besides the main peak in heat capacity associated with magnetic interactions, there is another and quantitatively more important peak at temperatures below 1 K. This extra peak comes from the hyperfine interaction due to the significant nuclear spins

of Holmium in $Ho_2Ti_2O_7$and can be fitted to a Schottky like form and subtracted from the total heat capacity to give us only the heat capacity of the system created by the magnetic interactions between the Holmium spins. [16] The entropy difference between low temperature and intermediate temperature turns out to be different from $R \ln 2$ for $Ho_2Ti_2O_7$as well (Fig. 2.3b).

The difference between the measured entropy difference and the expectation of $R \ln 2$ is very close to a special value $\Delta S = R/2 \ln 3/2$. This is the value predicted for the low temperature entropy of hexagonal ice $I_h$ by Pauling. [68] In the hexagonal ice, oxygens sit at the centers of tetrahedra. The tetrahedral lattice is defined by the protons, all of which occupy the corners of the tetrahedra on average, however slightly displaced from the ideal position. Every oxygen is surrounded by four protons; two of the protons are connected to oxygen by strong covalent bonds and are close to the oxygen, while the other two protons are connected to the oxygen by weaker hydrogen bonds and are farther from the oxygen (Fig. 2.4a). These rules are now known as ice rules, or Bernal-Fowler rules, and have been used extensively to explain the dielectric constant of ice. ( [69], [70], [71]) At low temperatures, there is no preference over which two protons should be close to the oxygen and which two should be far away. Then, for any single tetrahedron that contains four protons, there are six possible configurations that will satisfy the two protons near and two protons far rules, i.e. ice rules. Each oxygen is connected to four nearby protons, and each proton is shared between two oxygens such that the number of proton configurations in the system that fulfill the ice rules is

$$\Omega = \left(4 \cdot \frac{6}{16}\right)^{N/2} = (3/2)^{N/2}. \tag{2.2}$$

The entropy of the ice state then is calculated to be

$$S = k_B \ln \Omega = N k_B/2 \ln(3/2) \tag{2.3}$$

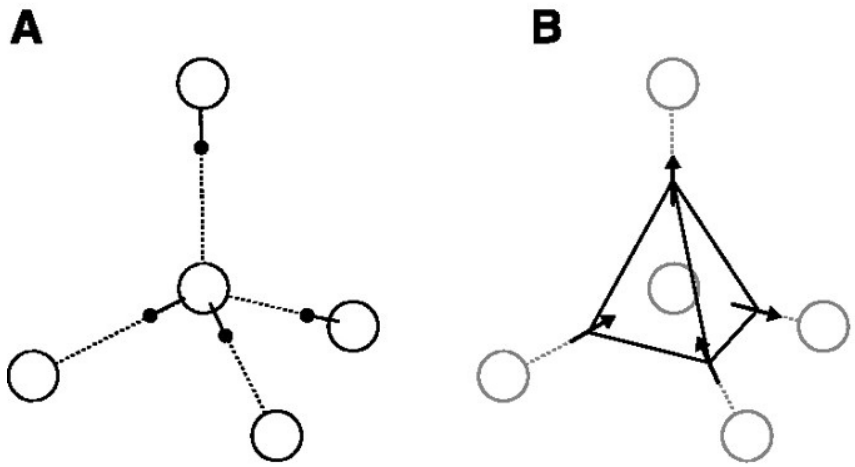


Figure 2.4: (a) The proton configuration in water ice, $I_h$. (b) Assumed spin configuration in the spin ice. The resemblance of two spin in and two spin out state in $Dy_2Ti_2O_7$ and $Ho_2Ti_2O_7$ to the proton configuration in hexagonal ice (two protons near and two protons far) has been the reason why magnetic systems like $Ho_2Ti_2O_7$ and $Dy_2Ti_2O_7$ are called spin ice. From [18].

which for a mole of material gives $S = R/2\ln(3/2)$. The observation of missing entropy both in $Ho_2Ti_2O_7$ and in $Dy_2Ti_2O_7$ has made these systems candidates for a spin configuration that can be directly mapped to the proton configuration in ice.

The spins both in $Ho_2Ti_2O_7$ and in $Dy_2Ti_2O_7$ have large magnetic moments in the ground state ($10\mu_B$ for both rare earth ions [63]), and as was described previously the ground state of the system is a doublet, i.e. is degenerate between spins pointing in two opposite directions (Fig. 2.4b). The low temperature state in these materials is then expected to have two of the spins in the tetrahedron to point in some direction and two in the opposite direction. If this analogue of ice rules is fulfilled, the spin system will have no definite low temperature configuration and at low temperatures the system will either be in a superposition of many different states all of which follow the ice rules. Or if the energy bar-

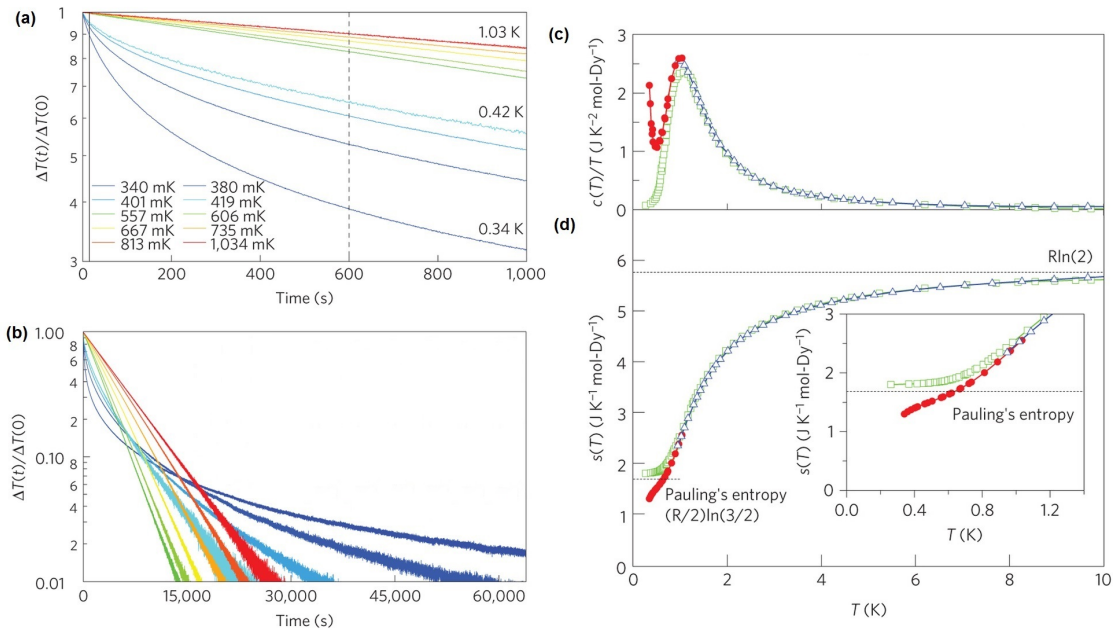


Figure 2.5: (a) Temperature relaxation over a weak thermal link after an initial temperature pulse above $\Delta T$ the equilibrium temperature. (b) At low temperatures, the thermal relaxation becomes very slow and wait times on the order of 100 hours must be accommodated for the system to explore the true equilibrium state. (c) Heat capacity from the long thermal relaxation measurements (red) compared to those from earlier work where relaxation was measured over ~100 seconds (green [15]). (d) Integrating this more precise heat capacity data gives entropy low temperature entropy lower than Pauling's result for ice. From [19].

riers are too large compared to the energy available to the system for transition between difference spin ice states, the system will get trapped in one particular state that will be a different state depending on what the state of the system was before it was cooled. Fig. 2.5 shows the details of the heat capacity measurement from a recent and more accurate study. [19] Here, the sample is connected to a heat bath with a weak thermal link and temperature profile $\Delta T(t)$ is measured after an applied temperature pulse at different temperatures. At high temperatures, the thermal relaxation is mainly determined by high heat capacity of the system, however as the temperature is lowered, very slow relaxation is observed (Fig. 2.5b). Temperature relaxation of up to 100 hours was mea-

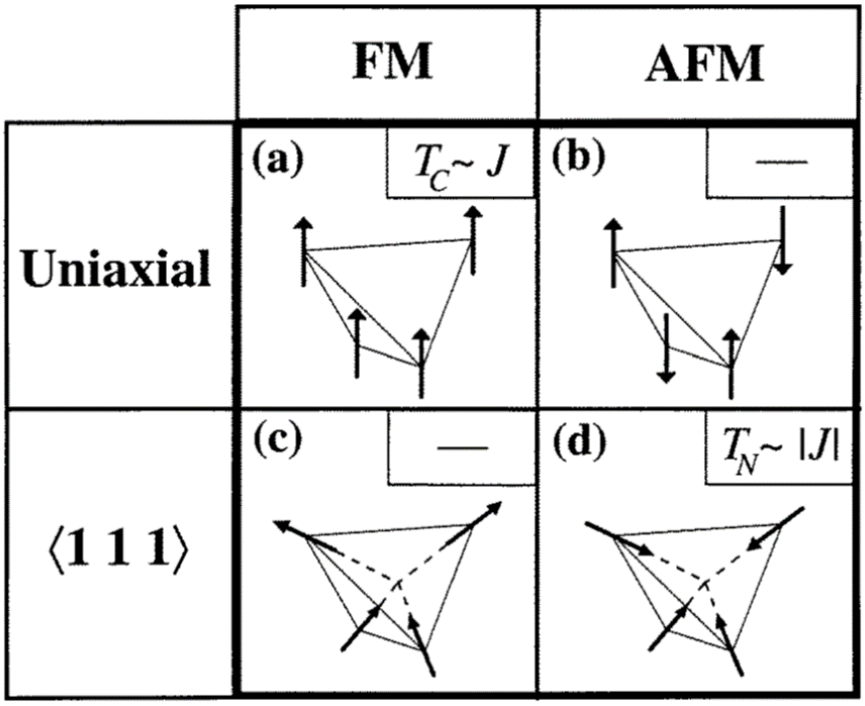


Figure 2.6: (a) For uniaxial spins in tetrahedral lattice, the nearest neighbor ferromagnetic interaction guarantees an ordered ferromagnetic state at low temperature, however (b) if the nearest neighbor interaction is instead antiferromagnetic, the system does not have a single ground state and becomes frustrated in a state similar to hexagonal ice. (c) If the spins are made to only point along the local 111 directions, i.e. towards the center of the tetrahedron or away from the center of the tetrahedron, ferromagnetic nearest neighbor interactions can create a frustrated low temperature state while (d) antiferromagnetic nearest neighbor interactions will result in a long range ordered antiferromagnetic state. From [20]

sured to get accurate value for heat capacity at low temperature. The heat capacity and entropy calculated from integrating this temperature profile is given in Fig. 2.5c,d and it is clear that if the system is given enough time to equilibrate, it can find an equilibrium state (possibly long range ordered [72]) at low temperature and the low temperature entropy will not be limited by Pauling's calculation for ice. However, as seen in Fig. 2.5b this is an increasingly difficult problem when temperature is reduced below 0.5 K, because the relaxation process becomes very slow.

The possibility of magnetic systems exhibiting similarity to the hexagonal ice was first studied by Anderson. [73] In his model, developed to explain the ferrite spinels like $NiFe_2O_4$, Anderson assumed spins forming tetrahedral lattice which interact with nearest neighbor antiferromagnetic interactions. In this model, the spins are also assumed to all point along the same line (Fig. 2.6a,b). For antiferromagnetic nearest neighbor interaction system exhibits low temperature frustrated state, a state where not all of the interaction constraints between spins can be satisfied and the system ends up in a degenerate energy state similar to the ice rule state in hexagonal ice. However, if the spins interact with ferromagnetic interactions instead, this model predicts a low temperature ferromagnetic phase with critical temperature $T_C \sim J$.

$Ho_2Ti_2O_7$ and $Dy_2Ti_2O_7$ on the other hand have ferromagnetic nearest neighbor exchange interactions. Fitting the DC susceptibility from higher temperatures to Curie-Weiss form gives $\theta_{CW}$=0.5 K for $Dy_2Ti_2O_7$ [15], and $\theta_{CW}$=1.9 K for $Ho_2Ti_2O_7$ [16]. Both of these are positive and indicate ferromagnetic nearest neighbor interaction. However, upon cooling down to these low temperatures and below, neutron scattering experiments show no long range ordered magnetic state in both systems. [74], [75] This has prompted to consider the similarity of the spin system to Anderson's model in [73] but in such a way that frustration can be generated with ferromagnetic nearest neighbor exchange interactions. Instead of all of the spins pointing along the same line, if the spins are required to point diagonally into the center of one of the tetrahedra that share it, the system now favors long range ordered antiferromagnetic state with all spins pointing into the center of the tetrahedron in one of the tetrahedra, and all spins pointing away from the center for the next tetrahedron. [20] The reason for why in this configuration of spins, antiferromagnetic nearest neighbor inter-

| | $Dy_2Ti_2O_7$ | $Ho_2Ti_2O_7$ |
|---|---|---|
| $S$ | 15/2 | 8 |
| $g_S$ | 4/3 | 5/4 |
| $\mu$ | $10\mu_B$ | $10\,\mu_B$ |
| $D = \frac{\mu_0\mu^2}{4\pi a^3}$ | 1.4 K | 1.4 K |
| $D_{nn}$ | 2.35 K | 2.35 K |
| $J$ | 3.72 | 1.56 K |
| $J_{nn}$ | 1.24 K | 0.52 K |

Table 2.1: Magnetic interactions important in the $Ho_2Ti_2O_7$ and $Dy_2Ti_2O_7$.

actions cause long range ordered state is explained in section 2.4, after introduction of the Hamiltonian used to study this magnetic system. However, with this configuration of spins, nearest neighbor ferromagnetic interactions will create a frustrated state similar to hexagonal ice, low energy state for every tetrahedron is such that two of the spins points toward the center of the tetrahedron while the other two point away from the center of the tetrahedron.

Although, the original attempt to explain the geometrical frustration in $Ho_2Ti_2O_7$ and $Dy_2Ti_2O_7$ used only nearest neighbor ferromagnetic exchange interactions it was quickly realized that dipolar interactions between large rare earth magnetic moments is necessary to provide correct description of the system. [16], [76] Table 2.1 has numbers for the important interactions between the spins in $Ho_2Ti_2O_7$ and $Dy_2Ti_2O_7$. Here, $a$ is the diamond lattice constant, or the distance between nearby moments, which is 4.38Å for both spin ices. The dipolar interaction between the spins is comparable to the nearest neighbor exchange interaction in both systems and must be included in the Hamiltonian in addition to the exchange interaction.

## 2.4 Dipolar Spin Ice

The Hamiltonian used to study the spin ices, $Ho_2Ti_2O_7$ and $Dy_2Ti_2O_7$ is [18]

$$H = -J \sum_{<ij>} \mathbf{S}_i \cdot \mathbf{S}_j + D r_{nn}^3 \sum_{j>i} \frac{\mathbf{S}_i \cdot \mathbf{S}_j}{|\mathbf{r}_{ij}|^3} - \frac{3(\mathbf{S}_i \cdot \mathbf{r}_{ij})(\mathbf{S}_j \cdot \mathbf{r}_{ij})}{|\mathbf{r}_{ij}|^5} \tag{2.4}$$

where $j$ is the nearest neighbor ferromagnetic exchange interaction, $D = \mu_0 \mu^2 / 4\pi r_{nn}^3$ is the strength of dipolar interaction between the neighboring moments, $r_{nn} = a$ is the diamond lattice constant, $\mathbf{S}_i$ and $\mathbf{S}_j$ are the spins at site $i$ and $j$, and $|\mathbf{r}_{ij}|$ is the distance between spins at different locations. $< i\,j >$ indicates the interaction is between nearest neighbors only, while the second term with $j > i$ means that the dipolar term includes the interaction between all the moments in the system. Early theoretical work has found that the full range of dipolar interactions has to be included to predict the properties of the system like the heat capacity. Attempts to reproduce the heat capacity of the spin ice $Ho_2Ti_2O_7$ with Monte Carlo simulations but where dipolar interactions are truncated beyond a set distance have predicted a sharp feature that can be associated with a thermodynamic phase transition (Fig. 2.7). [21] This however does not agree with the experimental results (Fig. 2.3), since in both systems magnetic heat capacity has a smooth peak.

The most efficient method to include the long range dipolar interactions without sacrificing quality of the simulation is to include them in a method called Ewald summation. [22] This method, originally developed to include the long range Coulomb interactions produces heat capacity predictions that agree very well with the experiments and has been the main method to extract the parameters corresponding to the important interactions Hamiltonian. [18] Best estiamtes of the exchange energy for the two systems obtained from fitting the heat capacity results to the Monte Carlo simulations of dipolar spin ice model are given in

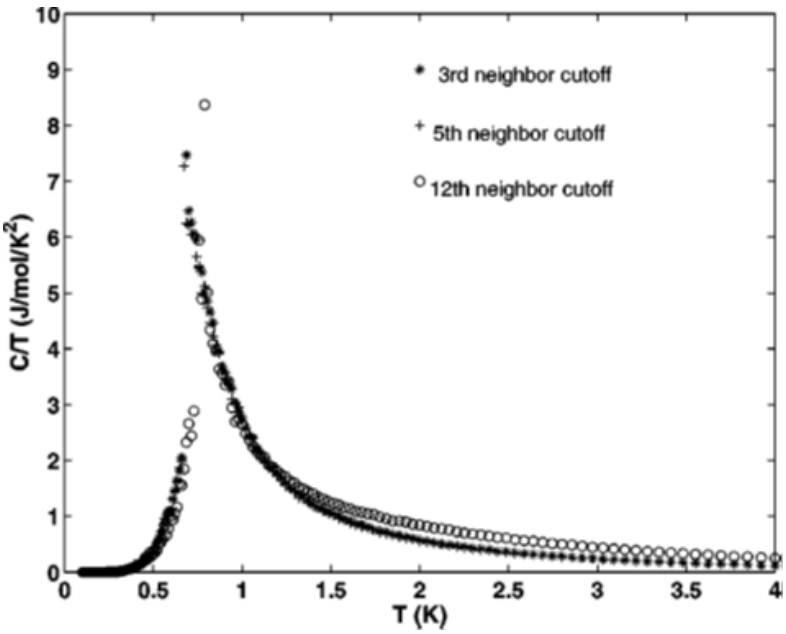


Figure 2.7: Monte Carlo simulations the heat capacity of $Ho_2Ti_2O_7$ but with dipolar interactions in Eqn. 2.4 truncated beyond a set distance. This results in nonphysical predictions for the system like the cusp in heat capacity that would otherwise be associated with some form of thermodynamic phase transition. [21] In reality, the heat capacity has no sharp feature as can be seen in Fig. 2.3c,d.

Table 2.1.

By this point, it is established that in the ground state of the system, the magnetic moments can only point towards the center of one of the tetrahedra that share it, along the so called local 111 directions. We can then map the system from the Heisenberg like Hamiltonian in Eqn. 2.4 to an Ising model such that $\sigma_i = +1$ means the spin is pointing away from the center of the tetrahedron, and $\sigma_i = -1$ means the spin is pointing towards the center of the tetrahedron. The angles between the spins will be important in converting from Eqn. 2.4 to an Ising model. In this new Ising like model, the nearest neighbor effective Ising interaction $J_{eff}$ in

$$H = \left(\frac{5D}{3} + \frac{J}{3}\right) \sum_{<ij>} \sigma_i \sigma_j = -J_{eff} \sum_{<ij>} \sigma_i \sigma_j \tag{2.5}$$

becomes antiferromagnetic $J_{eff} = -(5D/3 + J/3)$. We see that, the exchange interaction that was ferromagnetic in Eqn. 2.4 is now antiferromagnetic with effective strength $J/3$. This is because the angle between spins at the corner of the tetrahedra is such that the dot product $\hat{\mathbf{s}}_i \cdot \hat{\mathbf{s}}_j = -1/3$. This effective antiferromagnetic interaction is creates the tetrahedral analogue of the frustration in triangular lattice in the presence of antiferromagnetic nearest neighbor interactions. As a result, the low energy state will be when for two spins $\sigma = +1$ and for the other two $\sigma = -1$ which is the definition of the spin ice state that follows the ice rules.

The phase diagram for the system described by Eqn. 2.4 is given in Fig. 2.8. [22] For ferromagnetic nearest neighbor exchange interaction and for weak antiferromagnetic exchange interaction (weak compared to the nearest neighbor dipolar interaction) the system becomes frustrated at low temperatures and the lowest energy state will follow the ice rules. However, stronger antiferromagnetic nearest neighbor exchange interactions can lead to a low temperature long range ordered antiferromagnetic phase. The solid line is the line of phase transitions for antiferromagnetic ordering. For the spin ice state, the dotted line is the temperature at which the heat capacity becomes maximum, similar to the behavior in $Ho_2Ti_2O_7$ and $Dy_2Ti_2O_7$ as seen in Fig. 2.3.

The ice rules described in section 2.3 create long range correlations that fall off as power law. These rules correspond to a zero flux state for each tetrahedron, which effectively imposes a $\nabla \cdot \mathbf{M} = 0$ condition on the system. In the momentum space this corresponds to $\mathbf{k} \cdot \mathbf{M} = 0$, in other words, the equal time magnetization correlation function will be

$$\langle M_\mu(-\mathbf{k}) M_\nu(\mathbf{k}) \rangle = \frac{1}{\kappa}\Big(\delta_{\mu\nu} - \frac{k_\mu k_\nu}{|\mathbf{k}|^2}\Big) \tag{2.6}$$

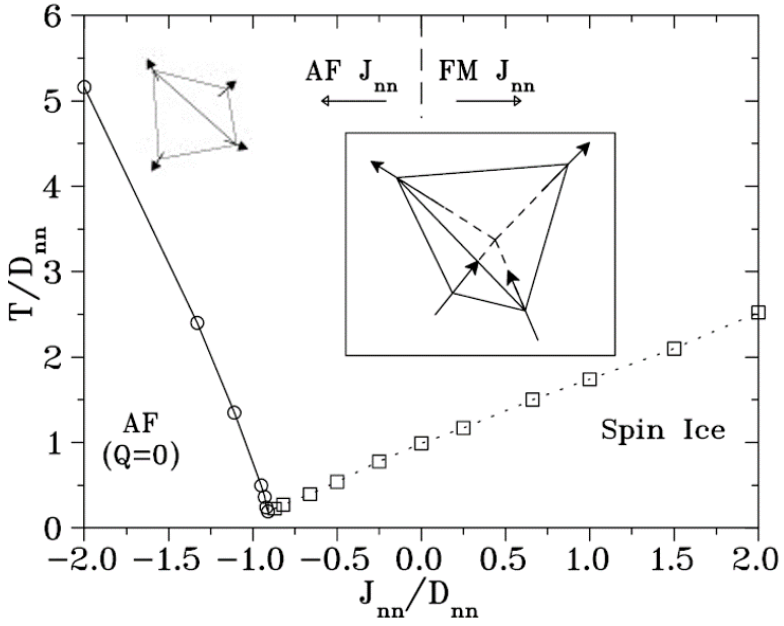


Figure 2.8: Phase diagram of the magnetic system described by the Hamiltonian in Eqn. 2.4 generated from the Monte Carlo simulations of the Hamiltonian. Full range of the dipolar interactions is included with Ewald summation. $J_{nn} = J/3$ and $D_{nn} = 5D/3$. For ferromagnetic nearest neighbor exchange interactions, and for weak antiferromagnetic exchange interactions (compared to the dipolar interaction) the lowest energy state of the system is the spin ice with two spins pointing in and two spins pointing out. For larger antiferromagnetic interactions, the system has long range ordered antiferromagnetic state. From [22]

where $\kappa$ is some effective "stiffness" corresponding to magnetization. [77] When Fourier transformed into position space, this correlation function becomes

$$\langle M_\mu(0)M_\nu(\mathbf{r})\rangle = \cong \frac{4\pi}{\kappa}\Big(\delta(\mathbf{r}) + \frac{1}{r^3}(\delta_{\mu\nu} - 3\hat{r_\mu}\hat{r_\nu})\Big) \tag{2.7}$$

which has the same form as dipole-dipole interaction. Theoretical work has also shown that in a system with significant long range dipolar interactions the magnetization correlation should follow the dipolar form given by Eqn. 2.6. [78] These correlations will be observed as the pinch points in diffuse scattering diagrams of $S(\mathbf{q})$, the structure factor in neutron scattering. Detection of these pinch points is a key observation in validating whether the system actually follows the ice rules or not. Fig. 2.9 shows the scattering factor of elastic neutron

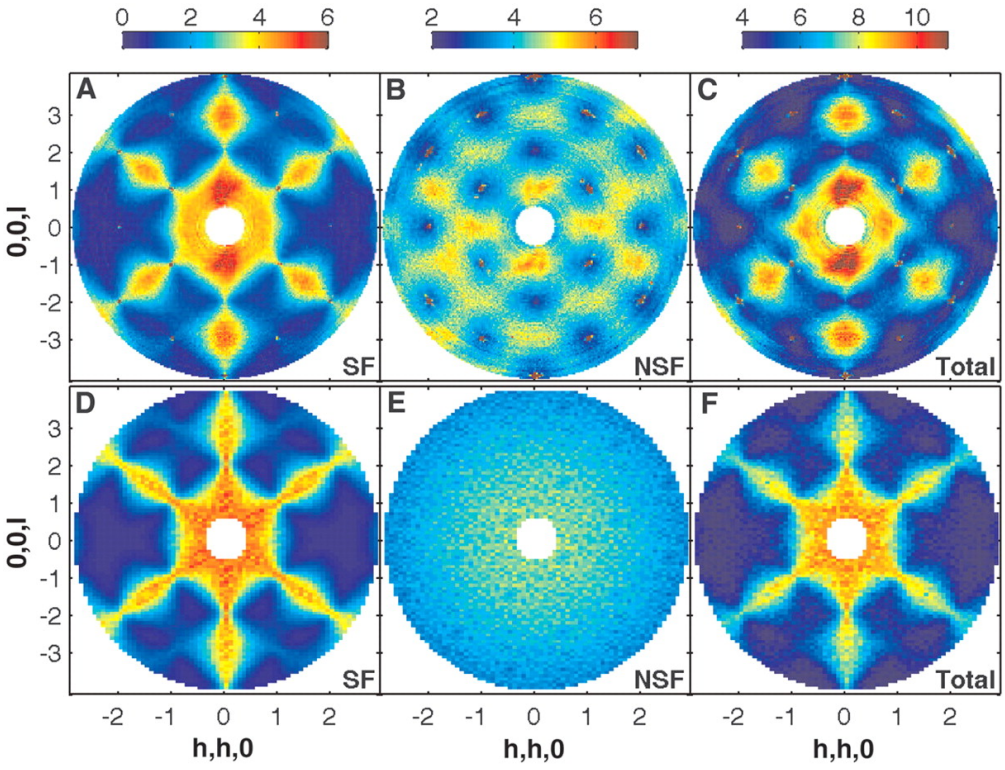


Figure 2.9: Diffuse scattering maps of $Ho_2Ti_2O_7$. (A-C) Experimental result for spin flip scattering, non spin flip scattering and total structure factor compared to the theoretical prediction (D-F). The pinch points in (C) are less pronounced than the expectation from theory (F) which indicates some longer range correlations of spins. These can be some form of loop correlations where on top of every tetrahedron following ice rules, spins along a closed loop will all point along the loop. From [23]

scattering performed on $Ho_2Ti_2O_7$. Top shows the measured $S(\mathbf{q})$ for spin flip (A), non spin (B) and total scattering (C) and is compared to the theoretical calculations (D-F). The pinch points in the experimental data are less pronounced than the theoretical predictions. This indicates a type longer range correlation between the spins. An example for such a correlation is, pins along a closed loop (minimum number of spins in smallest loop would be 6) being correlated such that they all point in the same direction as we move along the loop, on top of the usual ice rule correlations. [23], [79] This adds an extra length scale to the system and modifies the structure factor at the pinch points at wavevector

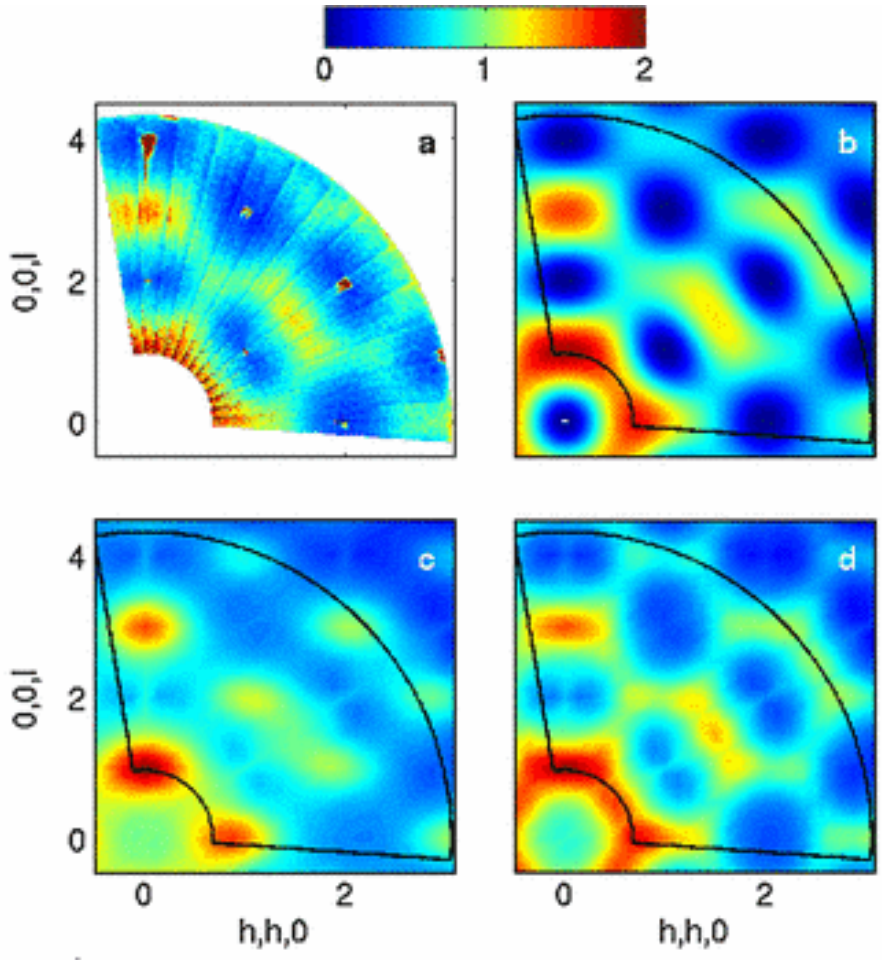


Figure 2.10: Neutron scattering intensity of $Dy_2Ti_2O_7$. (a) Experimental data, (b) intensity calculated with a model of uncorrelated hexagonal spin clusters or loops, (c) intensity calculated with dipolar spin ice model described by Eqn. 2.4 and (d) the predictions of a more general spin ice model that includes up to third nearest neighbor interactions. From [24]

resolution $\delta q \sim 1/\xi$, where $\xi$ is the length scale for the loops.

Fig. 2.10 shows the neutron scattering intensity of $Dy_2Ti_2O_7$. [24] Panel (c) shows the predictions of the dipolar spin ice model described by Eqn. 2.4. However, even better agreement with experimental data is found with a model that only assumes dynamics of uncorrelated hexagonal spin clusters or loops shown in panel (b). This is another evidence that loops dynamics can be important to accurately describe the magnetic system in spin ices $Ho_2Ti_2O_7$ and $Dy_2Ti_2O_7$.

Such closed loop correlations have seen use in Monte Carlo simulations to predict a possible low temperature ordered phase in spin ice [72], and has been part of discussion of dynamics of both protons in hexagonal ice [80] and spins in $Dy_2Ti_2O_7$ [3].

## 2.5 Monopoles in Spin Ice

Magnetic monopoles have been theoretical curiosity from the early days of electromagnetism. Before Biot-Savart and Ampere's laws became mainstream, the magnetic field created by magnetized objects was thought to be created by a dipole that has two monopoles of opposite polarity inside. Maxwell's equations, which are the fundamental relations used to make predictions about the interaction of charged or magnetized objects with each other and with fields of each other, are written such that effects of electric charges and magnetic charges are somewhat symmetric. If magnetic charges are present, it is a relatively easy task to modify Maxwell's equations to accommodate the new discovery. The first theoretical proposal for existence of quantized magnetic monopoles cam from Dirac who claimed that the quantization of electric charge can be explained if there are also magnetic monopoles in the universe. [81] A system composed of a single electric charge and a single magnetic monopole will have angular momentum proportional to the product of the two charges, and the prediction of free magnetic monopole charge from Dirac's arguments was $2q_eq_m/\varepsilon_0c^2 = n$, where $n$ is an integer. Despite intense searches for free monopoles expected from Dirac's theory, at this point existence of such magnetic monopoles is still under question. [82]

There have been proposals to realize magnetic monopole like excitations in

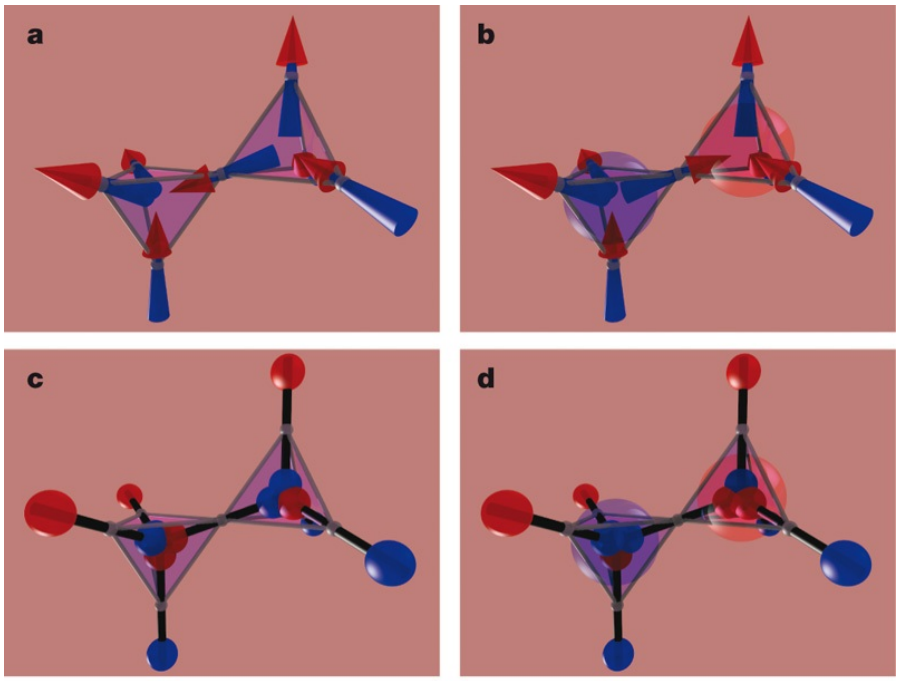


Figure 2.11: (a) Two neighboring tetrahedra of that follow ice rules simultaneously and (b) the new state after single spin flip, where one tetrahedron has three spins pointing in and one spin pointing out, while the other tetrahedron has one spin pointing in and three spins pointing out. If each of these spins (dipoles) are assumed to be made of two monopoles, in the ice rule following state, each inward pointing spin contributes two monopoles and each outward pointing spin contributes two antimonopoles and the net monopole charge in each tetrahedron is zero (c). The state created after a single spin flip will have nonzero positive monopole charge in the tetrahedron with three spins pointing in and one spin pointing out, and nonzero negative monopole charge in the tetrahedron with one spin pointing in and three spins pointing out. From [25].

a number condensed matter or atomic physics systems like superconducting quantum dots [83], surfaces of topological insulators [84], [85] and Bose-Einstein condensates [86], [87]. Possibility of monopoles in the geometrically frustrated spin ices was suggested twice independently, first in 2004 by I. Ryzhkin [88] from analogy to the proton dynamics in ice and Jaccard theory and second in 2008 by Castelnovo *et al* [25] from the observation that one of the dominant interactions in dipolar spin ices is the long range dipolar interaction. In the model proposed by Castelnovo and colleagues, each spin, a dipole is assumed to be

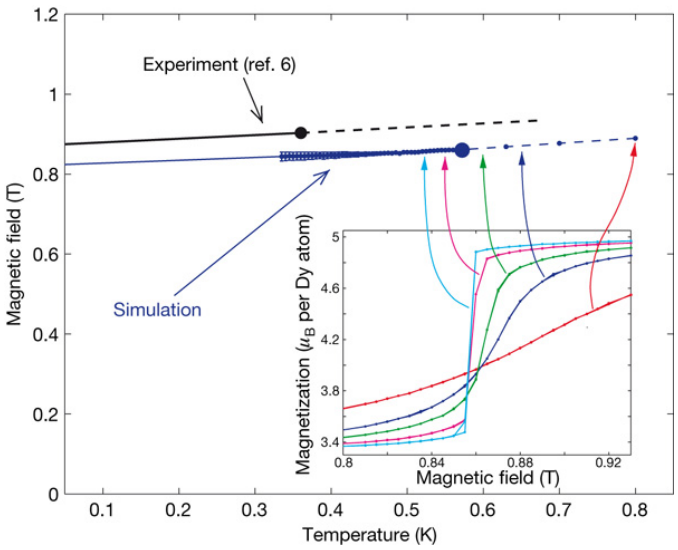


Figure 2.12: $B - T$ phase diagram of $Dy_2Ti_2O_7$. Monopole theory is used to explain the line of first order transitions observed in $Dy_2Ti_2O_7$ at intermediate fields below 1 K. From [25], [26]

composed of two monopoles (Fig. 2.11) of charge $q = \pm\mu/a_d$ where $a_d = \sqrt{3/2}a$ is the distance between the centers of two neighboring tetrahedra. The monopoles are situated such that the positive monopole is in the tetrahedron towards which the spins points and negative monopole is located in the tetrahedron that the spin points away from. If in a particular state of the system, the tetrahedron satisfies the ice rules, the spins pointing into that tetrahedron contribute two positive charges to the total monopole charge while the two spins pointing away from the tetrahedron contribute two negative charges. Then the configuration of spins that satisfy the ice rules corresponds to a tetrahedron with no net monopole charge (Fig. 2.11c). If a spin connecting the two tetrahedra both of which satisfy ice rules flips, both of these tetrahedra will not satisfy ice rules any more. The tetrahedron with three spins pointing in and one spin pointing out will have a total monopole charge of $Q_+ = 2\mu/a_d$, while the tetrahedron with one spin pointing in and three spins pointing out will have a total monopole charge $Q_- = -2\mu/a_d$ (red and blue spehere in Fig. 2.11c,d). With this mapping of

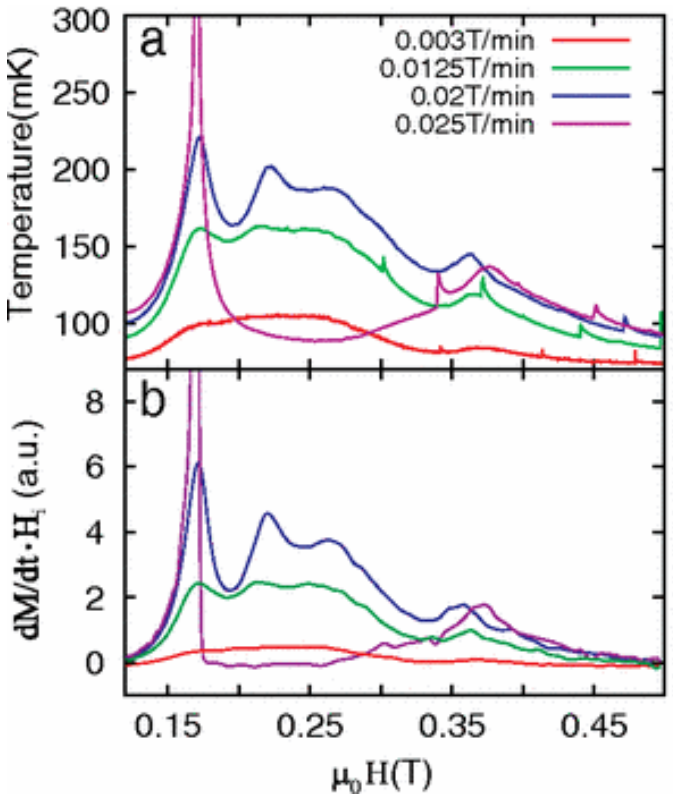


Figure 2.13: (a) The temperature profile of $Dy_2Ti_2O_7$ as a function of external field at different sweep rates and (b) estimated power dissipated by monopole motion. The good agreement between the two panels indicates that monopoles can be used to transport energy in the system. From [27]

dipoles onto effective monopoles, it is possible to transform the Hamiltonian of the system in Eqn. 2.4 onto a simpler one with monopole interaction

$$H = \frac{v_0}{2}\sum_i Q_i^2 + \sum_{j>i}\frac{\mu_0 Q_i Q_j}{4\pi r}. \tag{2.8}$$

Here, the first term is the self energy, the energy cost of having a nonzero monopole charge in the tetrahedron and is related to the paramaters of the sipolar spin ice Hamiltonian as [25]

$$v_0 = \left(\frac{a_d}{\mu}\right)^2\left(\frac{J}{3} + \frac{4}{3}\left[1 + \sqrt{\frac{2}{3}}\right]D\right) \tag{2.9}$$

and the second term is the Coulombic interaction between the monopoles with charges $Q = \pm 2\mu/a_d$ as defined above. The energy barrier to creation of the sin-

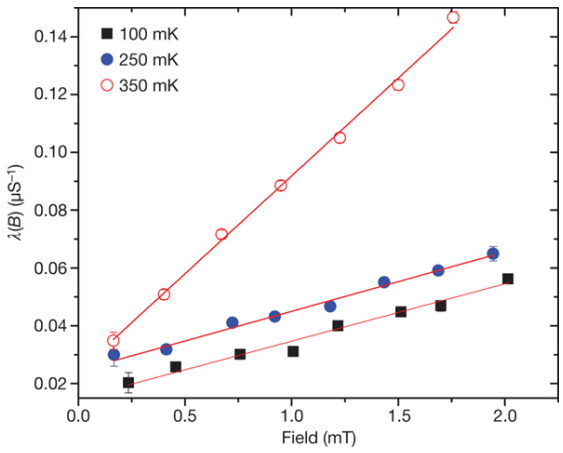


Figure 2.14: Muon decay rate as a function of field at different temperatures. The slope of the $\lambda$ vs $H$ curve is used to estimate monopole charge from the second Wien effect due to magnetic monopoles. From [28]

gle monopole pair is, $\Delta = v_0 Q^2 - \mu_0 Q^2/4\pi a_d$=5.4 K for $Dy_2Ti_2O_7$ and 8.5 K for $Ho_2Ti_2O_7$. To leading order in $r$, Eqn. 2.8 is equivalent to the dipolar spin ice model, the deviations between the two models dies out as $1/r^5$. [25]

The further spin flips after the monopoles are created can then be viewed as monopoles moving around, under the external field. Since spin flips are essential for creation and migration of monopoles, monopole motion will be characterized by a trail of spin flips behind it. This string of flipped spins is referred to as "Dirac string" to draw familiarity to the original proposal of monopoles by Dirac. [25] In the original paper, the Coulombic interaction between monopoles was proposed to explain a line of first order transitions observed as jumps in magnetization in intermediate magnetic field, ~1 T at temperatures below 1 K. However, the possibility of observing magnetic monopoles in spin ice has galvanized greater number of experimental work. Few of them will be described now, more will be discussed in the next section after discussion of models of monopoles dynamics.

Fig. 2.13 shows the results of the low temperature magnetization experiment

done on $Dy_2Ti_2O_7$. [27] At low temperatures, the magnetization of the rod shaped material is measured with Faraday force magnetometer which is calibrated against a SQUID, and the raw magnetization data is corrected for the demagnetization effect coming from the geometric shape of the material. The temperature of the material is measured with a local thermometer. There is clear agreement between the temperature profile of the sample as the field is varied at different speeds (panel (a)) and the estimated work done by the magnetic field while magnetizing the system (panel (b)). At high sweep rates, the system is unable to equilibrate under the rapid change of external field; the energy is dumped into the system locally heating it up.

Monopole charge was also estimated by drawing similarity to the second Wien effect where the monopole dissociation rate should depend on the external field. [28] This change of dissociation constant should be observed as the change of muon decay rate with field in muon spin relaxation experiments. Fig. 2.14 shows the reported muon decay rate with external field at low temperatures. The slope of this line from second Wien effect should equal $\mu_0 Q^3/16\pi k_B^2 T^2$ and was used in ref. [28] to estimate monopole charge in $Dy_2Ti_2O_7$ and in the follow up work in $Ho_2Ti_2O_7$ [89]. However, these findings were later refuted by both experimental work in [90] on the basis that the reported change of muon decay rate with external field cannot be distinguished in a large background signal and by theoretical work [91] that argued the observed effects can be attributed to the stray field generated by the magnetized spin ice and not due to monopole physics.

## 2.6 Monopole Dynamics

The first attempt at predicting the magnetization dynamics of monopoles came from Ryzhkin by drawing the similarity to proton motion in ice. [88] This work is based on Jaccard's theory of the thermodynamics of the defects in water ice [92] and relies on two assumptions, monopole current is directly related to the change in magnetization and the thermodynamics of monopole transport can be studied from the principle of entropy creation in irreversible processes. First a configuration vector that is proportional to the macroscopic magnetization is defined as $\mathbf{\Omega} = \mathbf{M}/Q$. When $N_s$ number of spins flip along a direction $\hat{x}_i$ this will change the configuration vector by $\delta\mathbf{\Omega} = -a_d N_s/V\hat{x}_i$, where $a_d$ is the distance between tetrahedral centers as was defined before, and $V$ is the volume of the system. Each spin flip corresponds to the positive monopoles moving by $d\mathbf{r}_+ = -a_d\hat{x}_i$ or the negative monopoles moving by $d\mathbf{r}_- = a_d\hat{x}_i$. Then a general change in configuration vector corresponding to the motion of $N_+$ monopoles and $N_-$ antimonopoles is $\delta\mathbf{\Omega} = N_+ d\mathbf{r}_+/V - N_- d\mathbf{r}_-/V$. The rate of change of configuration will then be

$$\frac{d\mathbf{\Omega}}{dt} = \frac{N_+}{V}\frac{d\mathbf{r}_+}{dt} - \frac{N_-}{V}\frac{d\mathbf{r}_-}{dt} = \frac{N_+\mathbf{v}_+ - N_-\mathbf{v}_-}{V} = \mathbf{j}_+ - \mathbf{j}_- \tag{2.10}$$

where $\mathbf{j}_+$ and $\mathbf{j}_-$ are the currents of monopoles and antimonopoles respectively. There are fewer states corresponding to a state with nonzero magnetization, and the configurational entropy of the state with vector $\mathbf{\Omega}$ is [88]

$$S_c(\mathbf{\Omega}) - S_c(0) = -\frac{4}{\sqrt{3}} a_d k_B |\mathbf{\Omega}|^2. \tag{2.11}$$

From the thermodynamics of irreversible processes the total entropy change associated with monopole motion is given by

$$T\frac{dS}{dt} = \sum \mathbf{j_i} \cdot Q\mathbf{B} + T\frac{dS_c}{dt} \tag{2.12}$$

where the first term is the work done by the external field. Substituting the expression for configurational entropy in Eqn. 2.11 into 2.12 gives

$$T\frac{dS}{dt} = \mathbf{j}\cdot\left(Q\mathbf{B} - \frac{8}{\sqrt{3}}a_d k_B T\mathbf{\Omega}\right) \tag{2.13}$$

with $\mathbf{j} = \mathbf{j}_+ - \mathbf{j}_- = d\mathbf{\Omega}/dt$, the total monopole current. Eqn. 2.13 has the same form as the generalized thermodynamic force $\mathbf{j}\cdot\mathbf{F}$ with $\mathbf{F} = Q\mathbf{B} - (8/\sqrt{3})a_d k_B T\mathbf{\Omega}$. Assuming a linear response of the average velocity of the monopoles to the general force $\mathbf{v} = u\mathbf{F}/Q$ with mobility $u$, the monopole current of a fluid with density $n_m$ will then be given with a form of Ohm's law

$$\mathbf{J} = Q\mathbf{j} = \frac{d\mathbf{M}}{dt} = Qn_m u\mathbf{v} = Qn_m u\left(\mathbf{B} - \frac{\mu_0}{\chi_T}\mathbf{M}\right) = \sigma_m\left(\mathbf{B} - \frac{\mu_0}{\chi_T}\mathbf{M}\right) \tag{2.14}$$

where

$$\chi_T = \frac{\sqrt{3}\mu_0 Q^2}{8a_d k_B T} \tag{2.15}$$

is the effective DC susceptibility of the system and $\sigma_m = Qn_m u$ is the conductivity of the monopoles. The solution of the equation 2.14 in the time and frequency domain provides a prediction for the magnetization dynamics of the system governed by monopole transport. These predictions are

$$M(t) = \chi_T H(1 - e^{-t/\tau_m}) \tag{2.16}$$

$$J(t) = \sigma_m H e^{-t/\tau_m} \tag{2.17}$$

for time dependent magnetization with relaxation time $\tau_m = \chi_T/\mu_0 Qn_m u$ and

$$\chi(\omega) = \frac{\chi_T}{1 + i\omega\tau_m} \tag{2.18}$$

for AC susceptibility. [88], [93], [32]

Fig. 2.15 shows the magnetization autocorrelation function (left) and AC susceptibility of $Dy_2Ti_2O_7$. [29], [30] The autocorrelation function was obtained by numerical Fourier transform of the AC susceptibility data in [94]. Despite the

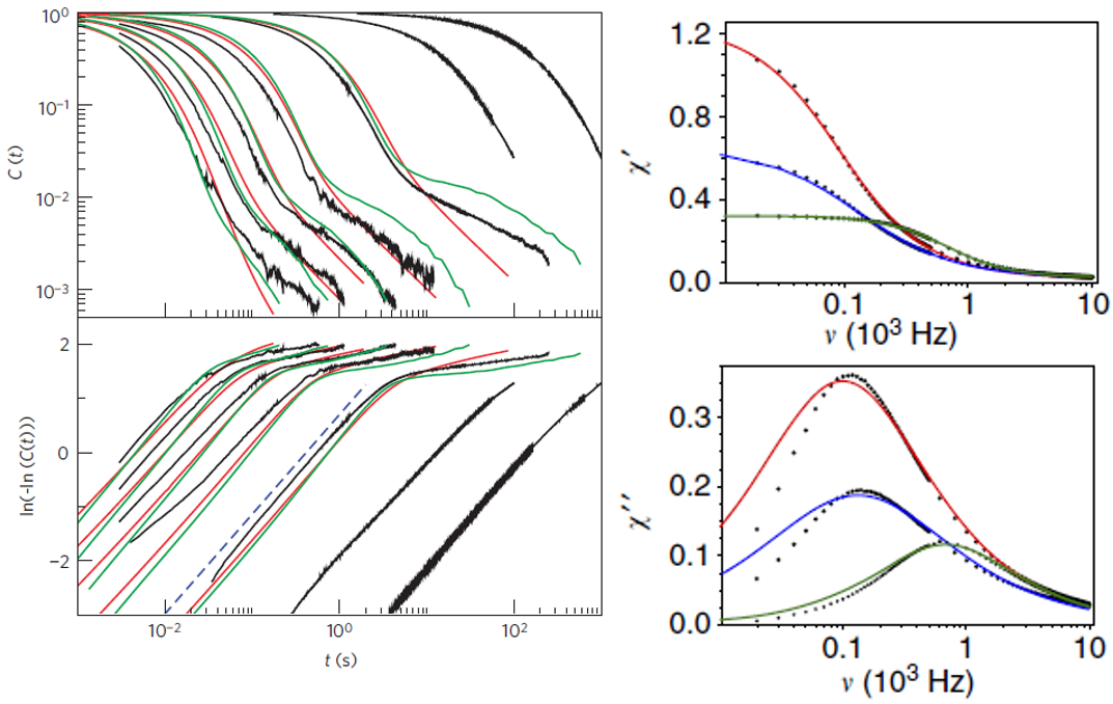


Figure 2.15: (Left) The autocorrelation function obtained from numerical Fourier transform of AC susceptibility of $Dy_2Ti_2O_7$. The simple exponential fit is insufficient and the stretched exponential form with $\beta \approx 0.7 - 0.8$ has to be used to explain the time dependence. (Right) Real and imaginary part of AC susceptibility of $Dy_2Ti_2O_7$. The solid lines are fits to Cole-Cole form (which is equivalent to HN form with $\gamma = 1$) as the form of AC susceptibility predicted by Eqn. 2.18 is unable to fit the data. From [29], [30]

expectations from Ryzhkin equations 2.16, the data cannot be fitted to a simple exponential form and stretching exponent of $\beta \approx 0.7 - 0.8$ had to be included to explain the time dependence of the autocorrelation function. The AC susceptibility as well doesn't fit the form in Eqn. 2.18. [95] The authors in reference [30] assume Cole-Cole fit, which is a version of Havriliak-Negami form with $\gamma = 1$ to fit AC susceptibility data. Debye-Hückel theory of monopoles [96] was also used to explain time dependent relaxation properties of $Dy_2Ti_2O_7$ [97], however the agreement with this theory was only for a narow temperature window, and at some temperatures fits with two exponential decays were necessary. Such two relaxation time fits of both time domain relaxation and AC susceptibility

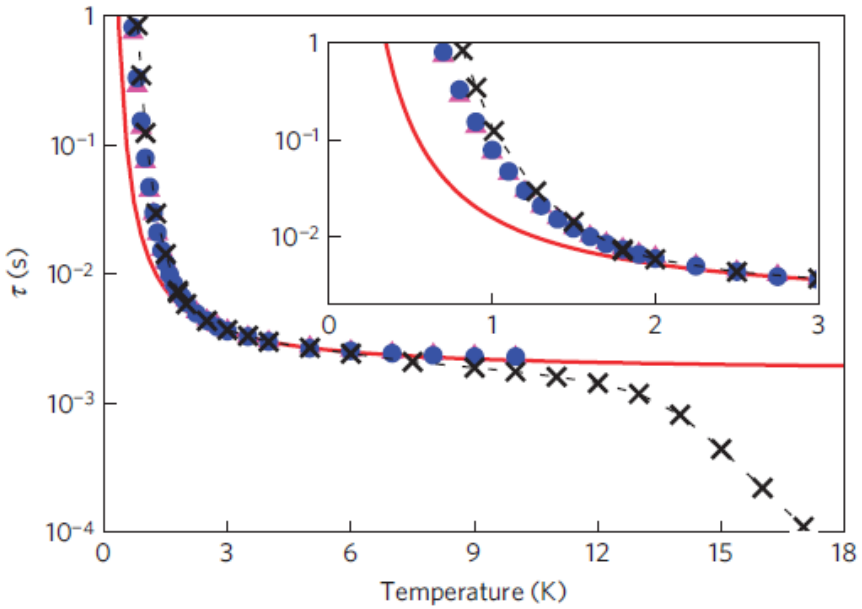


Figure 2.16: Relaxation time in $Dy_2Ti_2O_7$. Experimental data is in crosses from reference [31], red solid line is the simple Arrhenius fit and blue circle and red triangle symbols are from the Monte Carlo simulation with the assumption of Coulomb interaction between monopoles. From [32]

has seen better success [98] and is a special case of Havriliak-Negami function where in Eqn. 1.18 two delta functions with distinct relaxation times $\tau_1$ and $\tau_2$ are used instead of a more broad $G(\ln \tau)$ distribution.

Attempts to explain the temperature dependence of relaxation time in $Dy_2Ti_2O_7$ and $Ho_2Ti_2O_7$ with simple monopole theory have also been only partially successful. Fig. 2.16 shows the relaxation time data for $Dy_2Ti_2O_7$. The crosses are the experimentally measured relaxation time in $Dy_2Ti_2O_7$. The simple Arrhenius fit (red solid line) does a very poor job of capturing the changes in relaxation time below 2 K. Authors in reference [32] use Monte Carlo simulation of spin dynamics with the assumption of Coulomb interactions between monopoles, (blue circles and red triangles). We see that considering the long range Coulomb interactions improves the relaxation time significantly compared to the simple Arrhenius dependence for independent spin flips. However,

even this model doesn't fully account for the fast growth of relaxation time, and deviations from experimental data is seen below 1 K. Similar discrepancy was also reported when comparing the temperature dependence of the relaxation time in the other spin ice, $Ho_2Ti_2O_7$ [99].

CHAPTER 3

# EXPERIMENTS

## 3.1 Cryogenic System

To achieve low temperatures required for this project, we use a dilution refrigerator. Dilution refrigerator uses both of the stable isotopes of Helium, 3He and 4He, to generate cold temperatures down to 10 mK continuously. There are three key pieces of low temperature cryogen management system that allows us to reach temperatures below 50 mK; the 4He pot, also known as the 1 K pot, the still which is effectively the 3He pot, and the final and coldest stage, the mixing chamber. These are explained in the following sections (Fig. 3.1).

### 3.1.1 4He pot

4He is a staple for experiments at very low temperatures. It is used both in the liquid free pulse tube coolers, where gaseous 4He is circulated to achieve temperatures as low as 4.2 K, the boiling point of liquid 4He, or in wet fridges where the latent heat of liquid 4He is used to maintain cryogenic temperatures down to 4.2 K. At ambient pressure, 4He does not freeze even down to absolute zero [33] and liquid 4He is a cost effective way for experiments down to ~4 K. However, the latent heat of liquid 4He is very low compared to many liquids (20kJ/kg comapared to 200 kJ/kg for liquid nitrogen), and the cryogenic systems containing liquid 4He have to be insulated from the room temperature extremely well to avoid unnecessary boiling of this precious cryogen. [33] Double walled containers, also known as dewars, are used where the space between

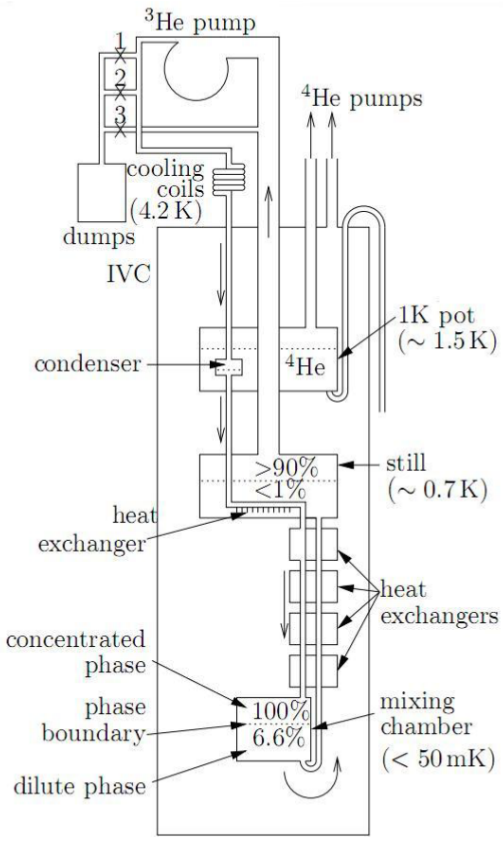


Figure 3.1: Schematic of an entire dilution refrigerator. The gasous 4He above the liquid 4He chamber, also known as pot is evacuated lowering the vapor pressure, hence the temperature of the pot down to 1.5 K. The mixture that comes from room temperature is made to thermalize well with this pot and goes to lower stages of the system at a temperature very close to pot temperature. The second stage, the still, is usually rich in the other isotope of helium, 3He and acts as a pot of 3He. Pumping on this section can reduce the temperature of the still down to 0.7 K. The mixing chamber is the coldest part of the system and relies on the phase separation of the 4He-3He mixture. When 3He atoms are forced to go through the phase separation boundary, they absorb energy from the system cooling the system down. This energy is later dumped on the still and is carried away by the 3He gas that is pumped out of the still by the circulation pump.

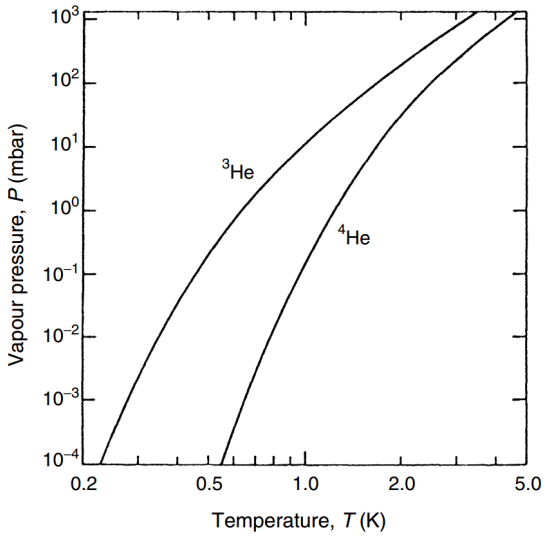


Figure 3.2: Vapor pressure of the two stable isotopes of helium. From [33]

the two walls is evacuated and filled with layers of material with very low thermal conductance. The outer wall of the insulating material is also coated with silver to reflect outward the radiative heat coming from room temperature. [33]

To achieve temperatures below the boiling of 4He, evaporative cooling is used. This relies on the fact that there is strong relationship between the boiling point of a liquid and the ambient pressure of its vapor, the vapor pressure. When the pressure of the gas above the liquid is reduced, the more energetic atoms of the liquid will escape to the empty space carrying away with it kinetic energy greater than the average kinetic energy of the atoms in the liquid. To get to 1.3 K from the boiling point of 4He, 40% of the liquid has to be evaporated. [33] This is rather inefficient use of the cryogen. However, heat capacity of most of the materials at such low temperatures is very small compared to the heat capacity of 4He. This knowledge is very useful for a design modification where one does not pump on the entire liquid helium bath. Instead there is a smaller container of liquid 4He connected to the 4He bath with a narrow capillary that has large

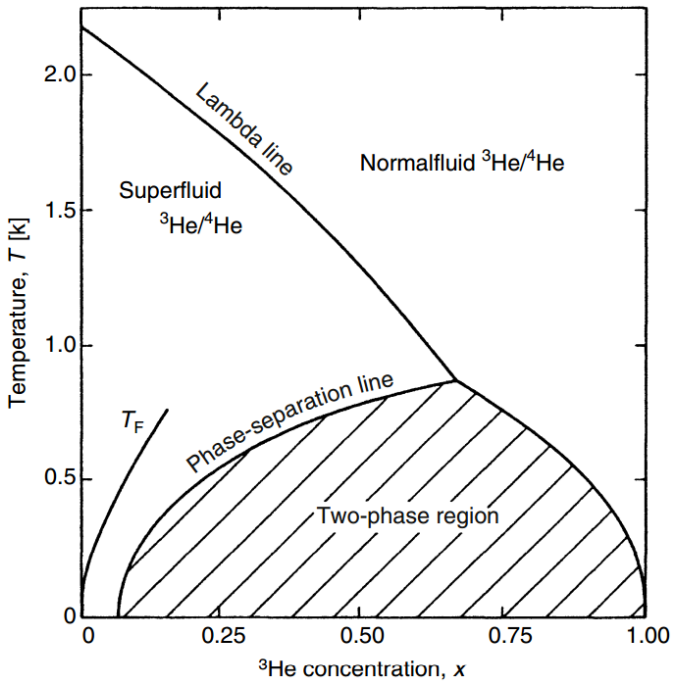


Figure 3.3: Phase diagram of the 4He-3He mixture. From [33]

impedance ($10^{11} cm^{-3}$ at room temperature) (Fig. 3.1). This high impedance line ensures that the amount of liquid in the pot is optimized to provide sufficient cooling down to ~ 1 K. The low flow also helps such that the pumps can generate vapor pressures ~ 1 mbar corresponding to the low temperature liquid (Fig. 3.2). The pot and the lower sections are situated in a vacuum can to eliminate the heat flow from the liquid 4He bath to the colder parts of the system.

### 3.1.2 Still and Mixing Chamber

4He becomes superfluid below 2.18 K (Fig. 3.3) [33]. When a mixture of 4He and 3He is passed through the pot continuously operating at 1.5 K, the heat exchangers help thermalize the incoming mixture to the operating temperature of

the pot. As this mixture proceeds to the lower parts of the system, most of the 4He in the mixture condenses into the container called the mixing chamber. At temperatures below 1K, the vapor pressure of 3He is significantly higher than the vapor pressure of 4He, such that during the continuous operation of the system, only 3He is pumped out of the system and is put back in. Right after the mixing chamber, the liquid 3He is collected in a third container called still. An external pump works on this container to reduce the vapor pressure such that the still can maintain temperatures around 0.7 K.

The mixing chamber itself can reach even lower temperatures by using the phase separation phenomenon in 3He-4He mixtures. Below 0.7 K, the mixture of 4He and 3He becomes unstable at certain mixing fractions and an arbitrary mixture of the two isotopes separates into two phases, one in rich in 3He and the other poor in 3He (Fig. 3.3). In the mixing chamber, the denser phase which is poor in 3He (or rich in 4He) sinks to the bottom. When the new 3He fluid is introduced into the mixing chamber it starts at the 3He rich phase, however as it passes through the unstable phase boundary into the 3He poor phase it absorbs energy from the system to go over the energy barrier. This energy is later dumped into the still as the 3He fluid follows through into this container as it is being pumped out. To improve the performance of the cooling system, the incoming 3He fluid is also cooled with outgoing 3He fluid with high quality heat exchangers located between the still and mixing chamber stages. With this design of the cryostat, dilution refrigerators can operate continuously at temperatures as low as 20 mK.

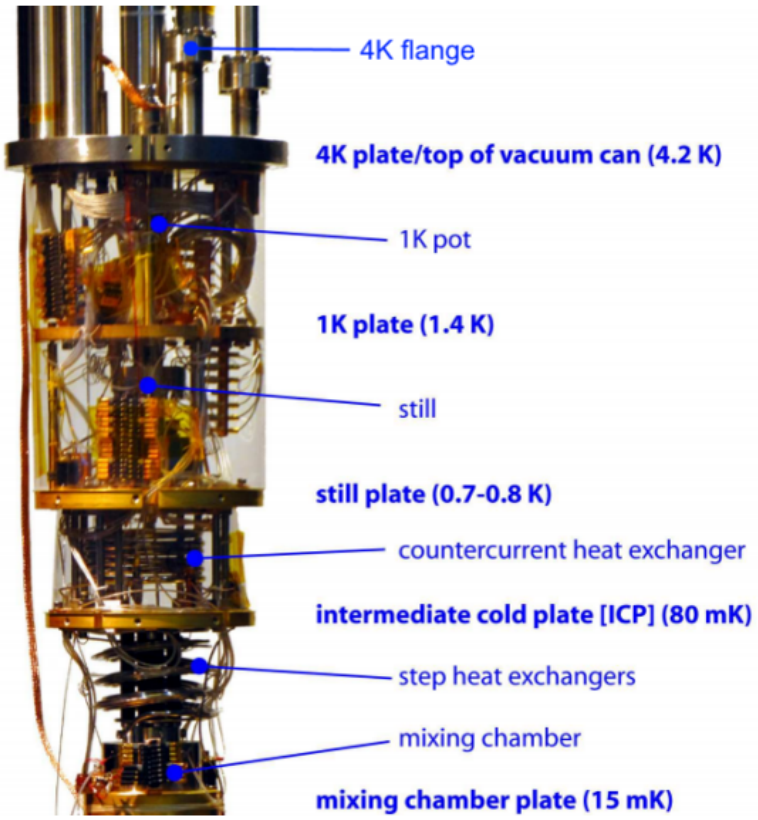


Figure 3.4: The photo of the low temperature section of the cryostat Cayuga.

### 3.1.3 Cayuga

The cryostat used for this project (nicknamed Cayuga) was mostly machined and assembled in UC Berkeley and Cornell by Minoru Yamashita, Joan Hoffmann and LASSP machine shop team. The cold temperature section of the cryostat is shown in Fig. 3.4. All the parts including the 4He pot and above were designed and machined in Cornell. The heat exchangers, the still and the mixing chamber were produced in collaboration with Janis Research Company. There is cylindrical experimental space below the mixing chamber of length 18″ and diameter 6″ which has proven very useful for this project. Besides the wires dedicated for experimentation, there are 4 heaters in the system and there are

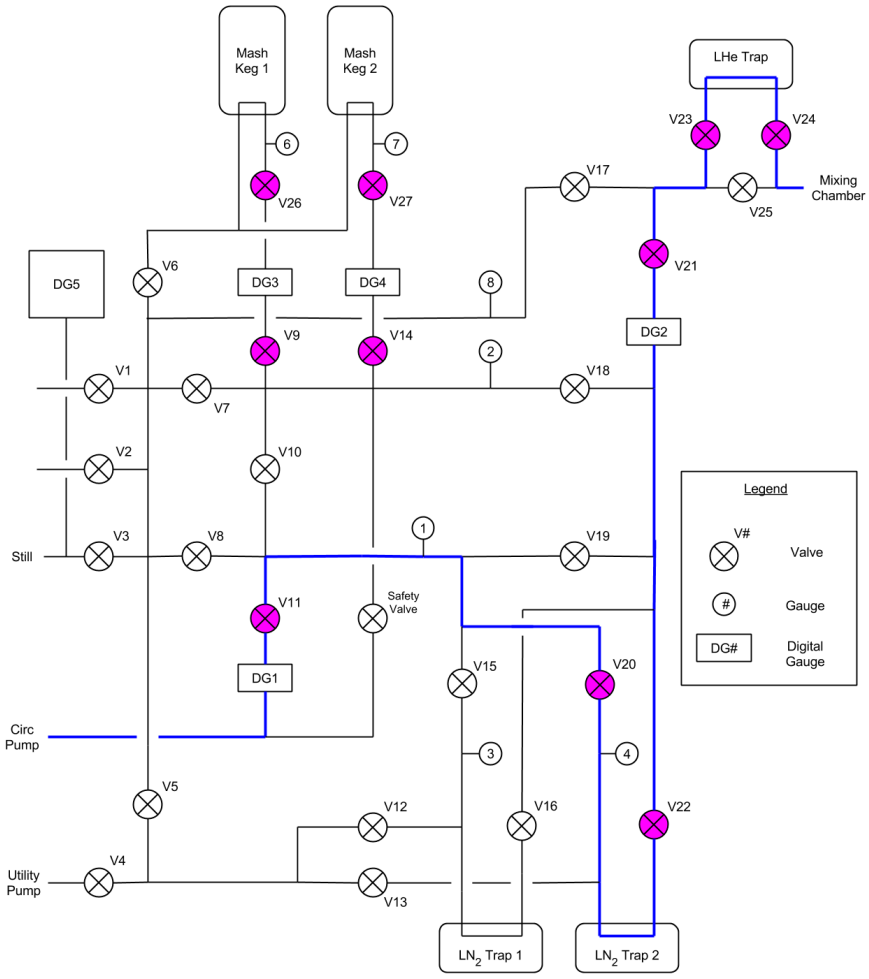


Figure 3.5: The 3He flow circuit during the continuous operation of the dilution refrigerator.

five thermometers to continuously monitor the system. The heaters are all 100 Ω metal wires and they are located at the pot, the still, the intermediate cold plate (an intermediate section between the still and the mixing chamber) and the mixing chamber. The heater at the mixing chamber is used to continuously control the temperature of the sample during the measurement, the rest of the heaters as well as the mixing chamber heater are used to speed up the boiling of liquid helium isotopes during warm up. The thermometers are located at the pot, the still, the intermediate cold plate, the mixing chamber and the fifth ruthenium

oxide thermometer is always placed very close to the experimental sample. The sample temperature is control in a closed PID feedback loop where the temperature controller continuously measures the sample thermometer and adjusts the heater power to the heater situated at the mixing chamber. All the supports below the mixing chamber are gold plated copper with very high thermal conductivity, and we observed that our current PID temperature control gives stable operational temperatures.

Fig. 3.5 shows the flow diagram during the continuous operation of the dilution refrigerator. The room temperature gas is always maintained below the atmospheric pressure to avoid any loss to the room due to possible leaks. When all the mixture is stored at room temperature, the pressure in the kegs is 750 mbar, and the DG1 reading (the pressure right after the circulation pump) during the continuous operation is 180 mbar. This pressure is always below ambient pressure such that if there is any leak at one of the joints, the air will leak into the system but 3He will not be lost. To avoid this air, as well as the oil vapor from the circulation pump to seep into the cryogenic parts of the system, the 3He is flowed through both liquid N2 and liquid 4He traps. The traps are cleaned every 2-3 weeks to keep them clean and to operate the system stably for long duration. The 4He bath inside the dewar space is refilled every 3-4 days during the normal operation.

## 3.2 Measurement Setup

The samples of $Ho_2Ti_2O_7$ and $Dy_2Ti_2O_7$ were grown and initially characterized by G. M. Luke group in McMaster University, Hamilton, Canada. They were grown as a boule under 2 atm $O_2$ pressure in an optical floating zone furnace

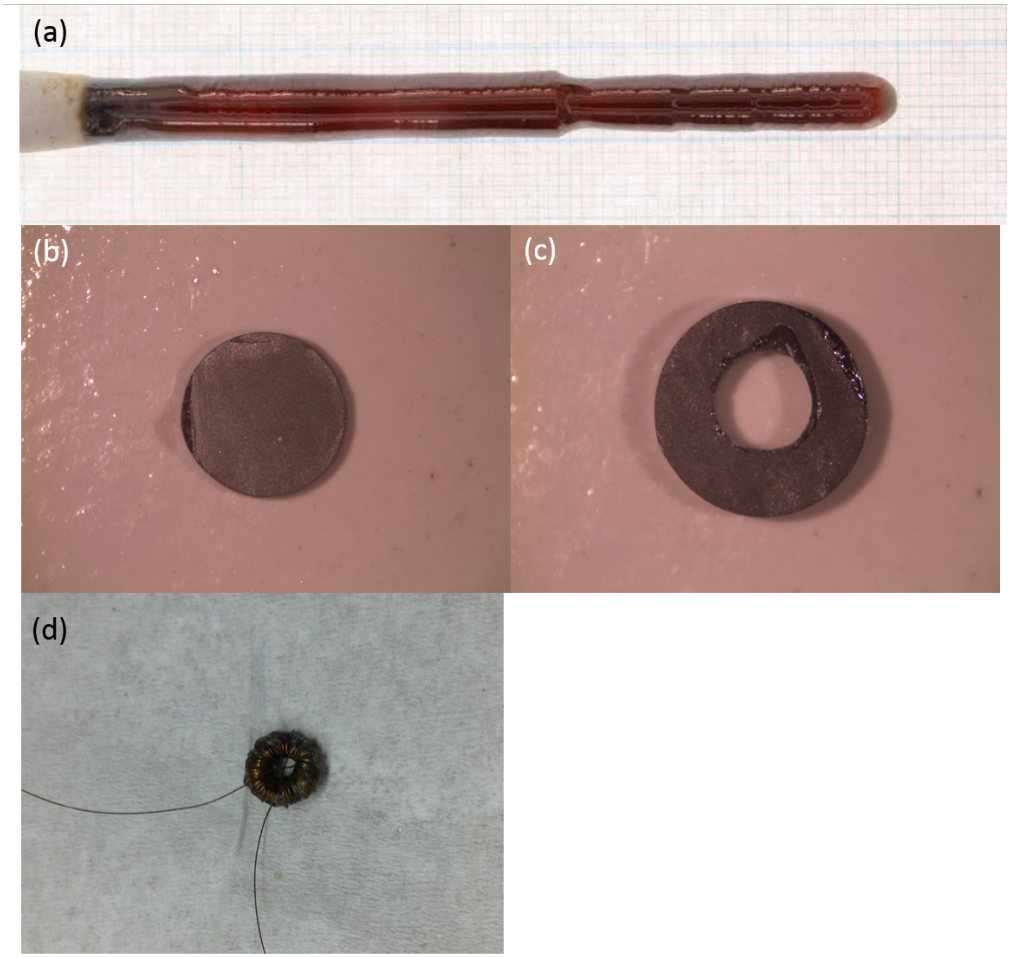


Figure 3.6: (a) The freshly grown titanate boule. (b) These are cut into disks of thickness ~ 1 mm and characterized in McMaster university. (c) The sample with a 2.5mm diameter hole drilled in the middle. (d) 0.08 mm diameter NbTi wire wound around the toroidal sample to create a superconducting toroidal solenoid.

(Fig. 3.6a). These were later cut into disks of thickness ~ 1 mm and diameter 6 mm (Fig. 3.6b), and characterized with X ray diffraction experiments to confirm that they were single crystalline. To probe the magnetization dynamics unambiguously we use a boundary free geometry. For this we drill a 2.5 mm diameter hole in the middle of the disk shaped samples with diamond tip drill bits at 900 rpm and wind a 0.08 mm diameter superconducting NbTi wire around it to create a superconducting toroidal solenoid (STS), Fig. 3.6c,d. Pass-

ing current through the STS applies an azimuthal magnetic field to the sample. In the STS there are no boundaries and the field is always continuous along the circumference of the sample. This removes any barriers for monopole transport and the boundary free geometry also eliminates the demagnetization effect that has to be included in analyzing the magnetic properties of rod shaped materials. [94], [99] Upon application of the azimuthal external field $H\hat{\phi}$ the material will magnetize along this field and this time dependent magnetization will generate an EMF in the STS that can be detected by measuring the voltage over the leads. This is effectively a four probe measurement where the same coil is used to apply magnetic field and detect the magnetization dynamics and AC susceptibility.

When time dependent external field is applied to the STS $H(t) = nI\Theta(t)$, the material will slowly magnetize. Assuming the magnetization at some time $t$ be $M(t)$ the emf generated in the coil at any time is

$$V = -\frac{d\Phi}{dt} = -\mu_0 NA\frac{d(H+M)}{dt}. \tag{3.1}$$

In time domain measurements, the external field is switched suddenly with switch times much less than the relaxation time of the material. The detailed curves are presented in the next section. For this reason, at times important for the data analysis the EMF generated by the coil can be assumed to be only due to the magnetization change of the sample.

$$V = -\mu_0 NA\frac{dM}{dt} \tag{3.2}$$

Eqn. 3.2 shows that the EMF measured across the STS is directly proportional to the rate of change of magnetization and gives direct information about the magnetization dynamics of the system. Additionally, since the monopole current is defined as $J = dM/dt$ (Eqn. 2.14), the EMF measured gives direct information

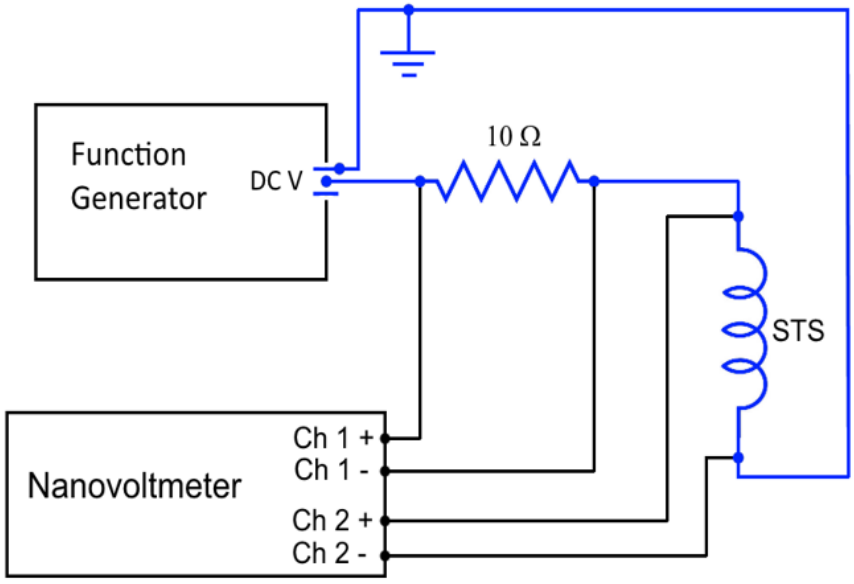


Figure 3.7: The circuit used for the time domain measurements

about the density of monopole current.

Fig. 3.7 shows the sketch of the circuit used for time domain measurements. The function generator Agilent 33210A is used to apply step function voltage. This drive voltage is generated over the the length of the entire circuit. The low temperature circuit has no resistance, but all the cables connecting the instruments in the control room to the cryostat were measured to have total effective resistance of 50 Ω. Another 10 Ω resistor is connected in series to continuously monitor the current over the STS. To generate drive current of 100 mA, we then need to apply voltage of 6 V at the function generator and the voltage of 1 V will be measured over the 10 |*omega* resistor. Both the voltage over series resistor and the EMF of the STS is measured with Nanovoltmeter Keithley 2182A. This instrument has two channels, the higher precision Channel 2 is used for the STS measurement, while Channel 1 is used to measure the current in the system at all times.

If instead a field periodic in time is applied to the system, $H = nIe^{i\omega t}$, there will be AC voltage generated over the STS

$$V = -\mu_0 NA\frac{d(H+M)}{dt} = -i\omega\mu_0 NAH(1+\chi) = -i\omega\mu_0 NAnI(1+\chi) = -i\omega LI(1+\chi) \quad (3.3)$$

where $L = \mu_0 nNA$ is the inductance of the STS when there is no magnetic material inside it. The inductance is measured separately as a control measurement, at temperature where no magnetic activity of the system is expected. Usually, 50 mK is chosen for this measurement, because at such low temperatures the dynamics of the system is so slow ( [98], [94] [99]) that no change in magnetization can be detected with Faraday effect based experiment. Subtracting the EMF measured at low reference temperature from the higher temperature measurement gives us a number that is directly proportional to the susceptibility of the material

$$\delta V = -i\omega LI\chi = -i\omega LI(\chi' - i\chi''). \quad (3.4)$$

The detailed procedure for the low temperature subtraction is given in the next section. One can then accurately measure the real and imaginary parts of susceptibility from in phase and 90° out of phase components of the measured EMF

$$\delta V_x = \omega LI\chi'' \quad (3.5)$$

and

$$\delta V_y = \omega LI\chi'. \quad (3.6)$$

Equations 3.5 and 3.6 are very useful to calculate the susceptibility from the measured EMF and inductance of the STS.

Fig. 3.8 shows the sketch of the circuit and the instruments used for the AC susceptibility measurements. The current is again generated as a voltage created by the oscillator output of the Lock-in amplifier Signal Recovery SR7265. Voltage over the 10 Ω series resistor is measured by the second lock-in amplifier SR830 to

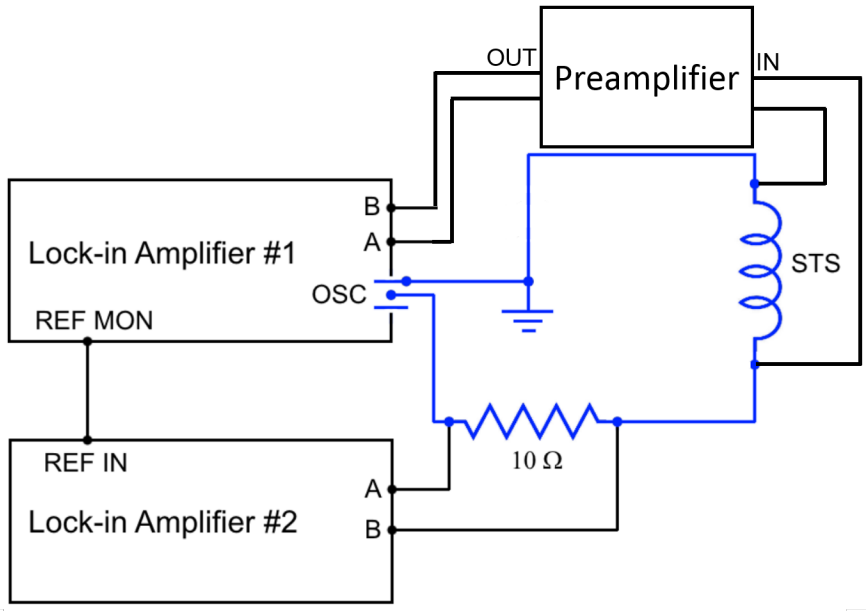


Figure 3.8: The circuit and instruments used for AC susceptibility measurements.

continuously measure the current over the STS, which corresponds to the magnetic field applied to the sample. The EMF over STS is first fed into preamplifier SR560 located right outside the cryostat and is set to broadband amplification. The output of the preamplifier is measured by the lock-in amplifier SR7265 and the susceptibility of the material is calculated from this measurement described by the procedure above.

To probe the magnetization dynamics, we use the homemade STS to apply magnetic fields to the materials. The highest magnetic fields that can be generated with the STS is limited by the geometry and the maximum current that can be applied without heating the cryogenic system. There is a hard limit for how tightly the STS can be wound, the coil density cannot be larger than inverse the diameter of the wire. Since we are using very thin wires, the coil density can be as high as $n \sim 10^4$, however even with this coil density we need currents as high as 100 mA, without any part of the low temperature circuitry going normal, to

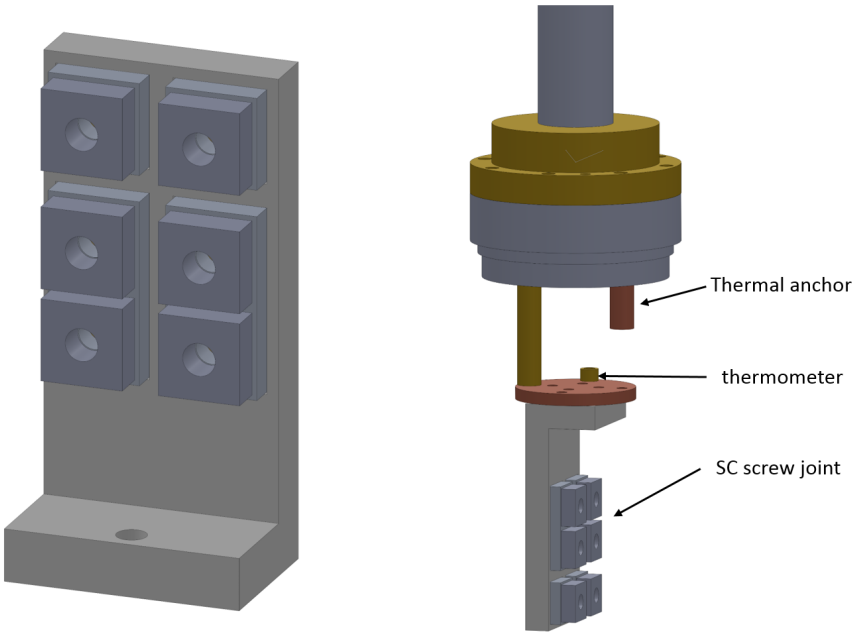


Figure 3.9: (Left) the Nb screw joint assembly inside the Stycast 1266 enclosure. (Right) the cryogenic test system to characterize the critical current of the superconducting screw joints.

generate magnetic fields in the milliTesla range. The critical current of the wires is reported to be few Amperes which is more than enough for our applications. Then, the weakest link in the low temperature circuit will be where the superconducting wires of the STS have to be connected to the superconducting wires inside the cryostat with the other end at room temperature. To improve success of this low temperature circuit we use two connections, the cryogenic superconducting screw joint, and the vacuum grade 4 K feedthrough that sits in the 4He bath right outside the vacuum can.

The superconducting screw joints are made with sandwiching the superconducting wires between two pads of thick Niobium (Fig. 3.9). The bottom Nb pads are 3/8" thick, are mounted inside an insulating post made of Stycast 1266 and are glued in place. The top Nb washers are 1/4" thick. To get high quality superconducting joints, the ends of the superconducting wires and both Nb

pads are sanded with rough sandpaper and are subsequently cleaned with isopropanol (IPA). Very soon after this, the wire is placed between the two pads and a brass screw is screwed in through the central hole very tightly. To ensure high quality superconducting joints for all of the wires, sanding and cleaning with IPA is performed for every connection just before the connection is made. Before placing the sample and the screw joints inside the dilution refrigerator, the critical current of the wire and joint assembly is tested in a homemade dip probe modified such that the assembly is in a vacuum can (Fig. 3.9 right).

The tests are performed in liquid 4He transport dewar. Evacuating the space around the superconducting joint reduces the cooling power from the 4He reservoir, and slight increases in resistance will generate local heat and create a positive feedback loop and drive more of the superconducting assembly normal. This will be registered as jump in the four probe resistance of the circuit and the temperature of the surrounding material will also increase. An on board thermometer measures the local temperature of the assembly and is located on the opposite side of the copper mounting plate (Fig. 3.9right). The bottom two washers are used to connect to the leads of the STS, the middle two are used to apply current and the top two are used to measure voltage. The current wires are made to go through both the top and middle Nb washers, this way the four probe resistance measurement will be sensitive to both the contact resistance between drive current wires and Nb pads, and between STS leads and Nb pads. All tests of the joints in dip probe assembly showed critical currents in excess of 100 mA, with one test showing critical current as high as 180 mA. After the tests, only the top and middle pairs of Nb pads were loosened, and the assembly with the STS leads still connected to bottom Nb pads was transferred to the cryostat for the experimentation.

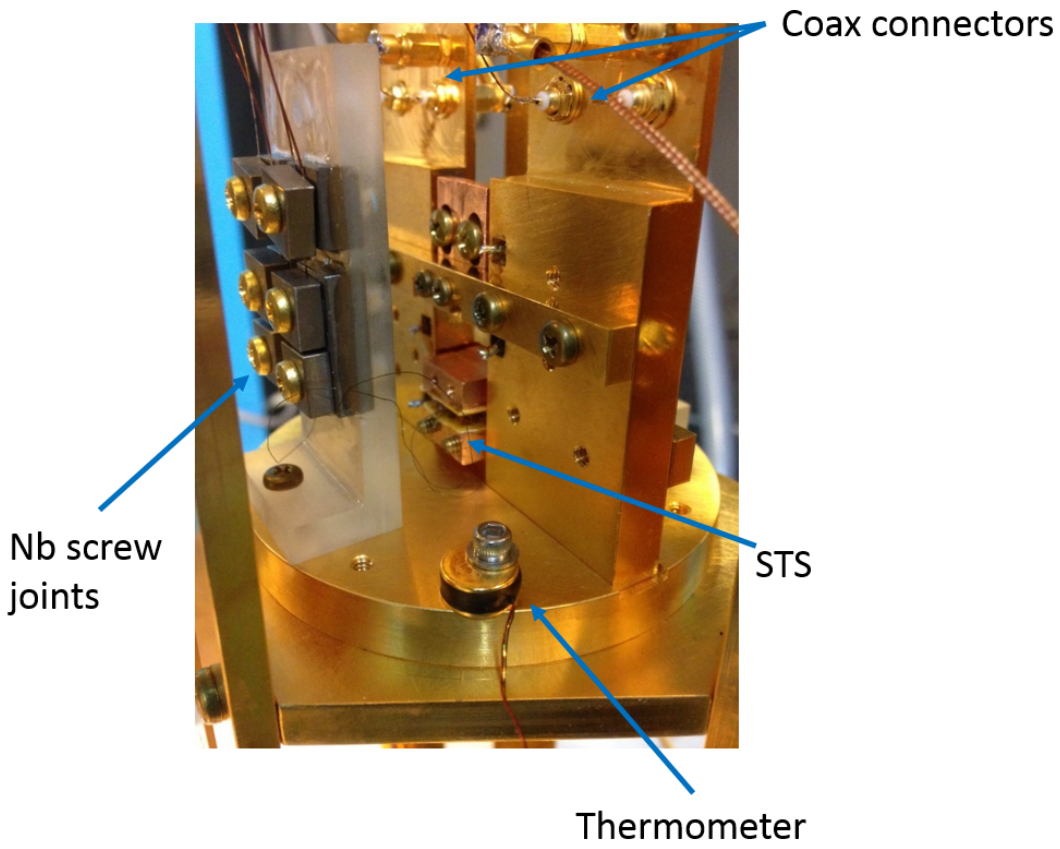


Figure 3.10: The experiment on board the cryostat. The samples with STS around them are sandwiched between copper plates to improve thermalization of the sample. Currents as high as 100 mA can be applied to the STS with the help of low temperature superconducting screw joints. An on board thermometer is used to control the temperature of the experiment in a PID feedback loop.

When mounting to the experiment similar sanding and cleaning with IPA procedure was used right before tightening every screw. Fig. 3.10 shows the photo of the experiment after it is mounted in the frame located under the mixing chamber. The $Ho_2Ti_2O_7$ and $Dy_2Ti_2O_7$ samples are sandwiched between copper plates to improve thermalization of the materials, and on board Ruthenium Oxide thermometer is used to control the temperature of the system in a closed PID feedback loop.

The cryogenic superconducting screw joints make sure that high current can

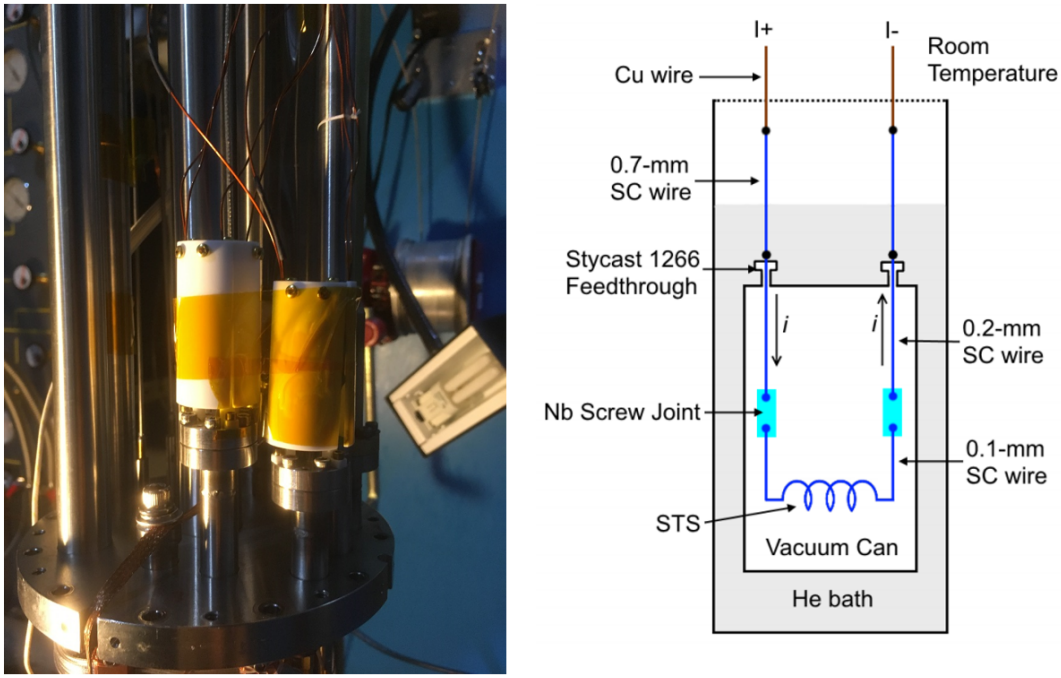


Figure 3.11: (Left) The 4K cryogenic feedthrough and (right) the sketch. The wires coming from room temperature are thermalized well by being inside liquid 4He bath. These are soldered to superconducting wires going inside the vacuum can, the solder joints are just outside the can. The feedthrough is made of Stycast 1266 and was tested to operate well in vacuum without any detectable leaks of 4He into the vacuum can.

be applied at cryogenic temperatures without heating up the system. But the power source used to generate the current is at room temperature and this wire has to be inserted inside the vacuum can in the most efficient way possible. Since there is no room temperature superconductor yet, the higher parts of any wire will be normal and will dissipate a lot of heat at high currents used in this experiment. This makes it impossible to send the current wires down the vacuum lines that go directly inside the vacuum can. We use CuNi clad, 0.7 mm thick NbTi wires from room temperature down to just outside the vacuum can. These wires are always thermalized with the liquid 4He bath. The wires from temperature are soldered to thinner CuNi clad 0.25 mm thick NbTi wires

just outside the vacuum can. The thin wire then goes through the Stycast 1266 feedthrough. The feedthrough was tested to be leak proof and does not jeopardize the vacuum level inside the vacuum can. Since the 0.25 mm thick superconducting wire is thermalized at 4K, all the section of this wire inside the vacuum can is superconducting and does not dissipate heat. This wire is then connected to the leads of the STS at the Nb screw joint.

## 3.3 Control Measurements

The first test performed after the cool down is the critical current test of the low temperature circuits. These are done twice for every STS circuit, once at 3 K and once at 50 mK close to the base temperature of the cryostat. Both of these temperatures are outside the experimental range but they give crucial information about the quality of the circuits at two extremes. At high temperature, the critical current of superconductor is smaller than the value at low temperature and safe application of current justifies the procedure at lower temperatures. At very low temperatures however, the cooling power of the cryostat is very small and any small local heating can drive an avalanche effect, turn the whole circuit normal and warm up the experimental space. The critical current tests showed that the low temperature superconducting circuit can support currents up to 200 mA without any noticeable heating.

The next test performed is to measure the inductance of the STS. For this, we apply 0.5 mA AC current at high frequencies $f > 10$ kHz and at low temperatures and measure the voltage generated. Prior experiments have shown that the $Ho_2Ti_2O_7$ and $Dy_2Ti_2O_7$ do not have any magnetic activity in this temperature and frequency range ( [94], [98], [99]), and we can attribute all of the EMF to

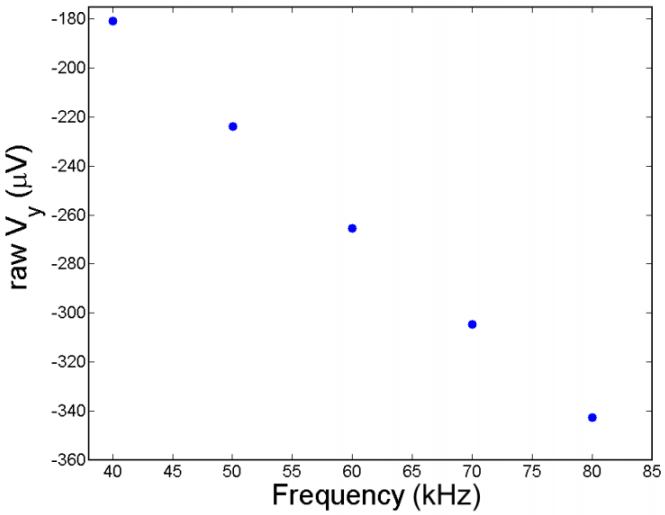


Figure 3.12: Inductance measurement at 30 mK at high frequencies, few 10 kHz. At such high frequencies the capacitive contribution to EMF is negligible and the inductance can be directly obtained from the slope of the curve.

the geometric inductance of the coils. Fig. 3.12 shows one of such plots, the vertical axis is the out of phase component of AC voltage and the horizontal axis is frequency. At high frequencies, capacitive contribution to the EMF is negligible and the slope of this curve gives accurate information about the inductance. The inductance of the STS used in these studies is usually few $\mu H$. This inductance value is used in later analysis to calculate the susceptibility.

The next test performed is measuring the stabilization time of the circuits after changes in temperature, current (or magnetic field) and frequency. For this, the EMF is measured as quickly as possible while changing number of external conditions and letting system wait at each new set of parameters for $\sim$ 3 hours. The frequency at which our data acquisition software can make a measurement is every 3 seconds. Fig. 3.13 shows the in phase and 90° out of phase component of EMF continuously measured while the frequency and temperature is stabilized at different values. The stabilization time after frequency jumps were observed to be less than 10 seconds for many frequency jumps tried, and the stabilization

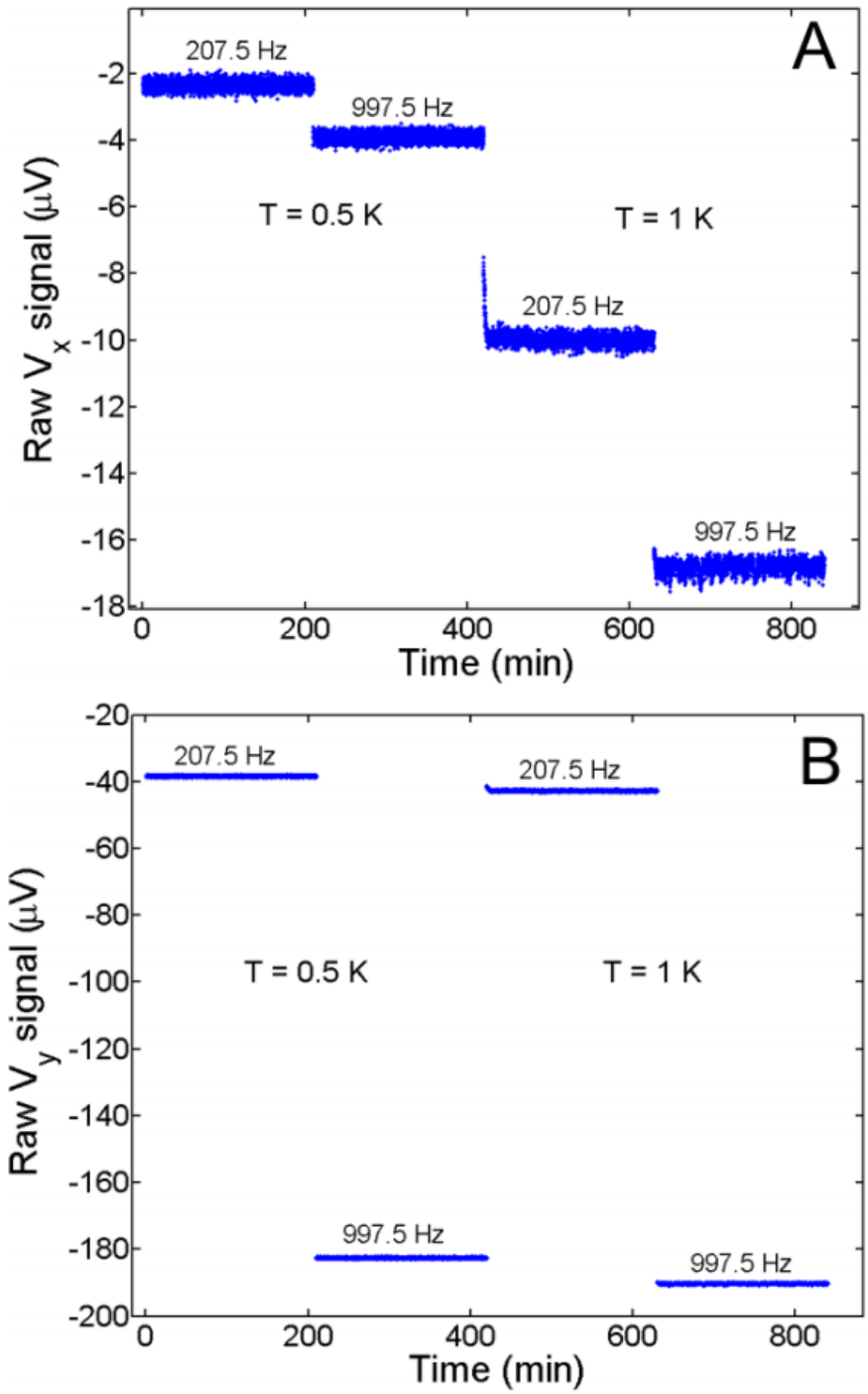


Figure 3.13: Time constant tests of one of the STS. (A) In phase and (B) 90 ° out of phase component of EMF for a STS on $Dy_2Ti_2O_7$. EMF is measured every 3 seconds and parameters like frequency and temperature is stabilized for ~ 3 hours after every change. Both components of EMF stabilize quicker than 10 seconds for many frequency jumps attempted. Relaxation times of <5 minutes were observed after temperature jumps.

time after temperature change was measured to be less than 5 minutes. With this knowledge, we set wait time of 15 seconds after frequency change and 10 minutes after temperature jump before taking the data. To reduce the statistical noise of AC measurements, we take 75 data points at every frequency and average over these.

Next we do background measurements. These are divided into two parts; choosing the highest temperature that we can use as background to subtract, and confirming that any measurement above this temperature is strictly due to the magnetic activity in the magnetic materials. For the first part, we first note that in the frequency range relevant for our measurements, $f$ = 1 Hz−100 kHz, both $Ho_2Ti_2O_7$ and $Dy_2Ti_2O_7$ were reported to have zero susceptibility below 0.6 K [94], [99]. So we are inclined to choose 0.5 K as a useful temperature that can be used as a background. On the other hand at even lower temperatures like 50 mK, there is no expectation for any magnetic dynamics, and we know that all the EMF generated in the STS is from parasitic sources. We then measure the EMF at various temperatures between 50 mK and 500 mK, both included, and compare whether temperatures as high as 500 mK can be considered as magnetically active temperatures. Fig. 3.14 shows the raw EMF normalized by the product $I\omega L$ over $Ho_2Ti_2O_7$ at different frequencies and temperatures including and below 500 mK. There is virtually nonexistent deviation between the different data sets at these low temperatures. This reinforces the prior choice that 500 mK is a low enough temperature below which our experiments cannot detect any magnetic activity. Fig. 3.15 shows the discrepancy between the higher temperature measurement and 50 mK measurement, as well as the discrepancy between two measurements performed at 50 mK. We see that (i) the data is reproducible and (ii) temperatures below 500 mK have estimated susceptibility

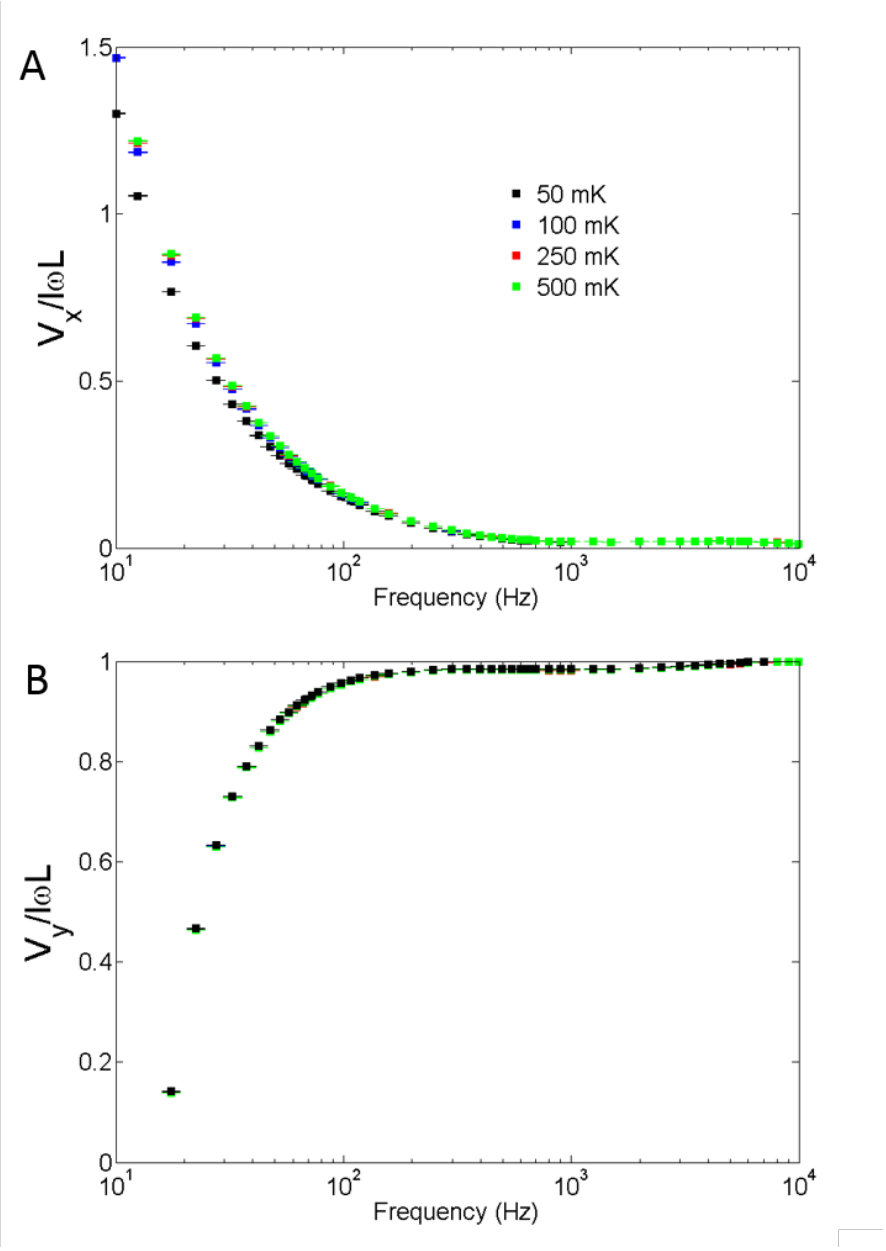


Figure 3.14: (A) The in phase and (B) out of phase component of EMF, normalized by $I\omega L$, over the STS at various temperatures including and below 500 mK for $Ho_2Ti_2O_7$. Both components of EMF show almost no temperature dependence over the entire frequency range measured. This confirms that at such low temperatures, all the EMF generated is from the parasitic sources.

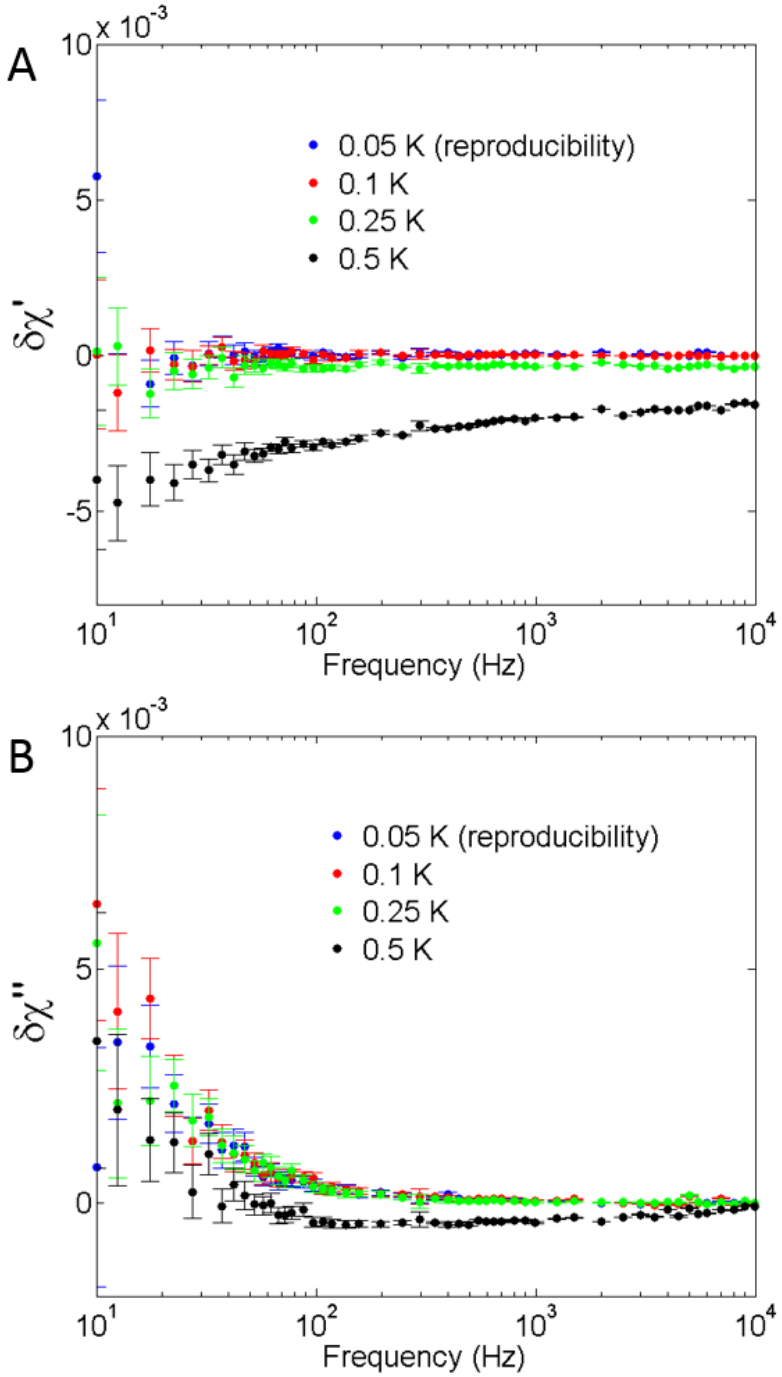


Figure 3.15: (A) The discrepancy of $\chi'$ and (B) of $\chi''$ between 50 mK and various temperatures up to 500 mK, and between two measurements performed at 50 mK, for $Ho_2Ti_2O_7$. The discrepancy is calculated following equations 3.5 and 3.6. The discrepancy is often within error limits and is 2-3 orders of magnitude less than the value for susceptibility at higher temperatures, which is of order unity.

that is withing the error bars. The deviation is 2-3 orders of magnitude less than the value of susceptibility at higher temperatures. We then deduce that if we assume 500 mK as the low reference temperature, this will influence the susceptibility measurement only at the third or fourth significant figure.

This choice of the low reference temperature may seem unnecessary tour de force, however we must look at how the cryostat operates for the importance of this practical finding. To cool the system to very low temperatures like 50 mK, the circulation pump has to circulate the maximum amount of 3He possible and the still pressure will be very small. At such high rates of circulation, the effective cooling power of the cryostat at temperatures as high as 2 K is enormous and employing heat as the only method to control the temperature makes it dangerous as large amounts of heat must be used. However, the system needs only modest amount of 3He circulation to reach 500 mK, and continuous operation between 500 mK and higher temperatures is relatively easy, and does not jeopardize the cryostat by applying large amounts of heat to low temperature sections.

We next look at the discrepancy between EMF over STS wound around a torus made Stycast 1266. This control experiment is done to ensure that all the magnetization signal detected at the desired temperature range is due to genuine magnetization dynamics of the material and not due to external effects that have some possible temperature dependence. Fig. 3.16 shows the deviation of in phase and out of phase EMF from its value at 500 mK for STS around a Stycast torus. The torus was machined to have geometric parameters similar to out $Ho_2Ti_2O_7$ and $Dy_2Ti_2O_7$ samples. Virtually no deviation between the EMF at 500 mK and temperatures as high as 2 K is observed in the frequency window of the experiment. We conclude that, any deviation of the EMF measured at high

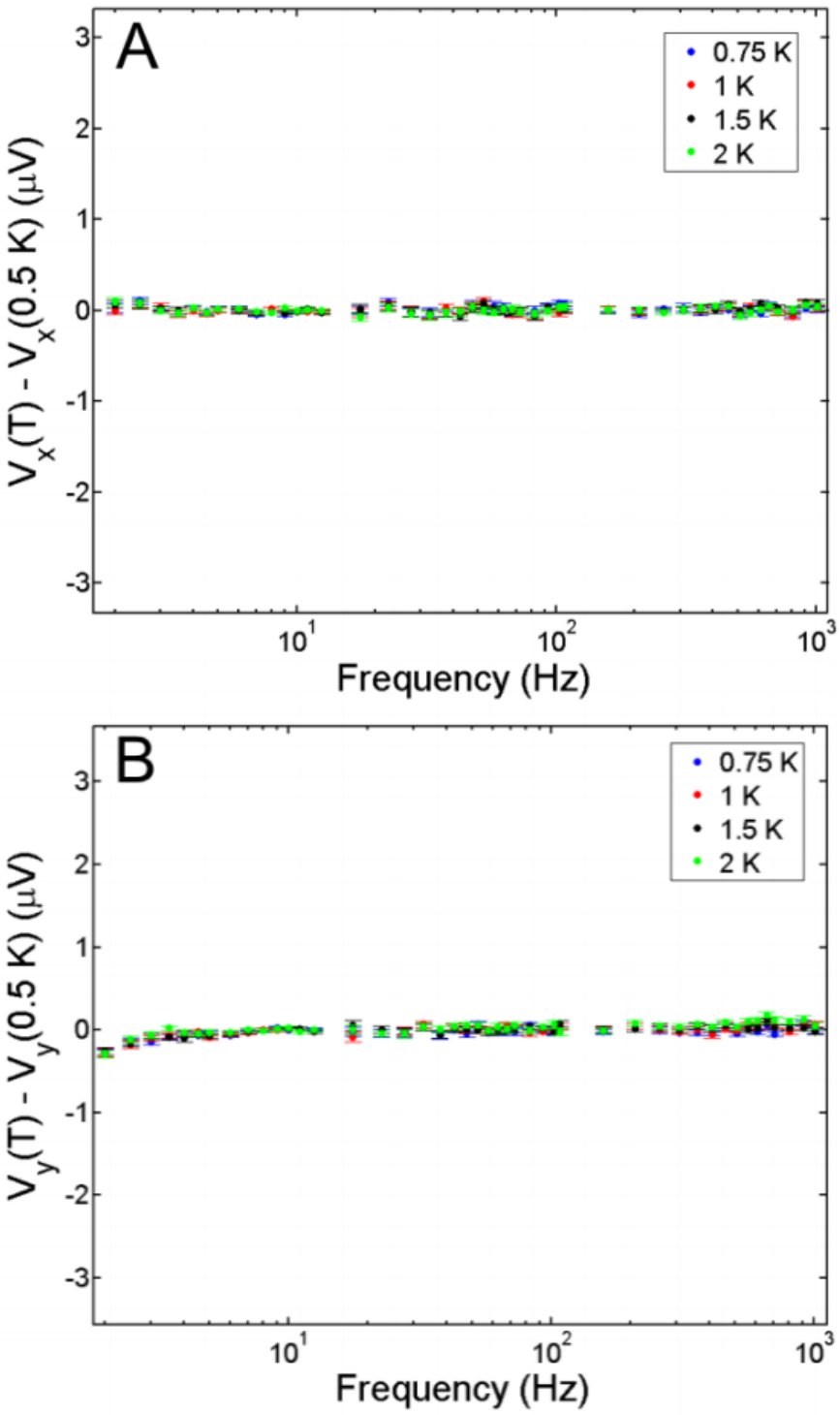


Figure 3.16: (A) Deviation of in phase and (B) out of phase component of EMF from its value at 500 mK generated over STS wound around Stycast 1266. This concludes that effects not coming from the magnetism of the experimental samples have no temperature dependence, and all the data measured and calculated using equation 3.5 and 3.6 come from genuine magnetic dynamics of the aterials.

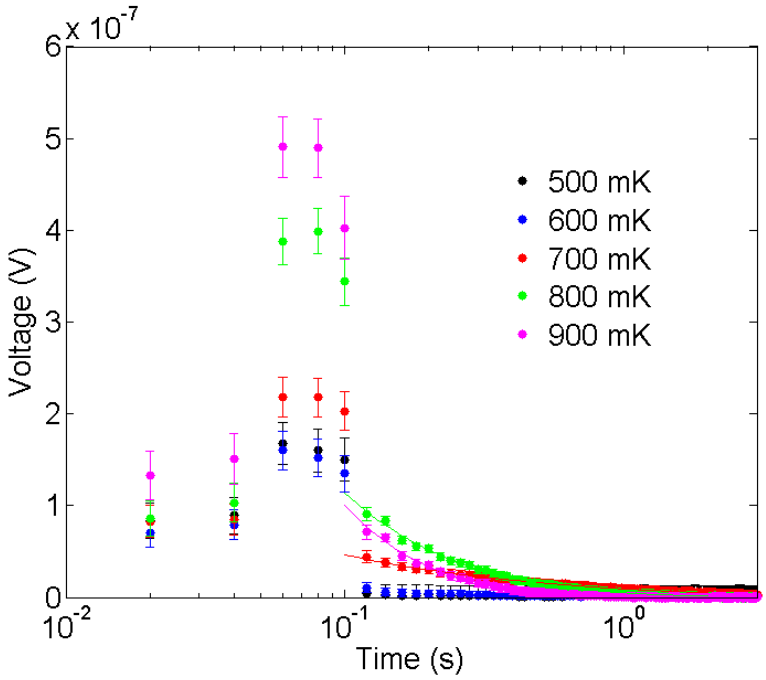


Figure 3.17: The averaged EMF over an STS wound around $Ho_2Ti_2O_7$. At early times, $t \leq 0.1$ s, there is charging effect due to the current stabilization in inductive circuit. At times after this, decay of EMF indicates the magnetization dynamics in the system.

temperature from the measurements at 500 mK over the magnetic materials is strictly due to magnetization dynamics and the analysis in equations 3.5 and 3.6 should unambiguously yield the AC susceptibility of the materials.

For time domain measurements, we use the function generator to apply a step function change in current from zero to 50 mA over the duration of 20-100 s, switch the applied current off for the same duration, apply the current of equal magnitude but in the opposite direction, and switch the current off, again over the same duration. The data is taken every 20 milliseconds such that the nanovoltmeter has time greater than the period of the line frequency to acquire data.

Fig. 3.17 shows the averaged EMF over an STS wound around $Ho_2Ti_2O_7$. At early times, there is non monotonous behavior seen. This is due to the charging of the inductor after the change in current. At times after 0.1 s, monotonous

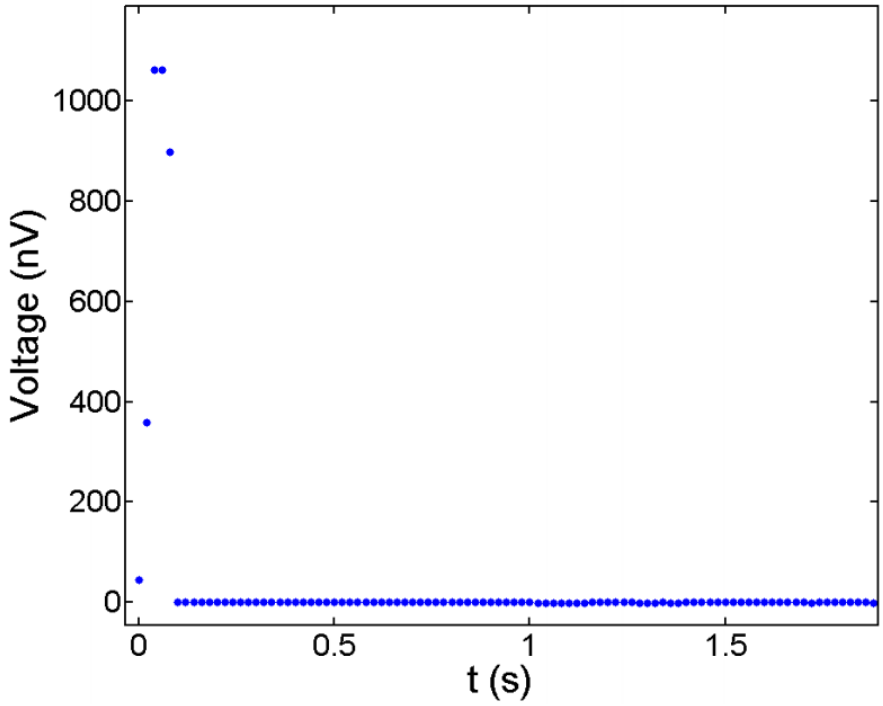


Figure 3.18: EMF generated over STS wound around Stycast 1266 torus. There is clear sign of charging effect at early times, however EMF is not discernible from zero after 100 ms.

decay of EMF gives information about the magnetization of the system. The similar test done on the STS wound around Stycast 1266 showed no EMF after the initial charging present at early times (Fig. 3.18). We then deduce that the EMF generated after the first 100 milliseconds can be used to study the relaxation properties of the materials and the first step in our data analysis is to remove the early time data and reset the time to zero for fitting procedures carried on later.

To get quality data, at every temperature up to 150 cycles of current turn on/off as described above are carried out and averaged. The initial EMF generated is few hundred nanovolts, however at long times after 50 seconds slowly varying noise noise amplitude is present. To accurately take the average of multiple transients we follow the following procedure. For each transient, generate the

temporary background voltage defined as the average of the measured EMF between $t = 20$ s and $t = 25$ s.

$$V_{b,i} = \frac{1}{m} \sum_{t_j=20}^{t_j=25} V_i(t_j) \tag{3.7}$$

where $m$ is the number of data points in the specified interval. At the data taking interval of 20 ms, $m = 250$. This EMF is subtracted from the EMF measured at earlier times, $t < 20$ s and is attributed to magnetization dynamics. As a final step, the data after the background has been subtracted is averaged over 150 runs to generate smooth decay curves

$$V(t) = \frac{1}{N} \sum_{i=1}^{N} (V_i(t) - V_{b,i}) \tag{3.8}$$

where $N = 150$ is the number of time a transient was measured at a certain temperature. We observed that this scheme reduced the error bars down to $\sim 10$ nV compared to a different analysis protocol where the same background voltage was subtracted from every transient. However, since the background voltage varies significantly over large periods of time that the experiment is performed, the error bars in the latter method were consistently larger than the error bars in the method described above. For some experiments, the error bars in the analysis method that assumed constant background were as large as 100 nV.

To see how the data quality improves with the number of transients included in the averaging procedure (equation 3.8), we looked at how the standard deviation of the relaxation time, obtained from fitting the EMF transients to a form of exponential decay (details of the fit are given in the next chapter). Fig. 3.12 shows the dependence of the standard deviation $\delta\tau$ and the effective signal to noise ration $\tau/\delta\tau$ for $Ho_2Ti_2O_7$ (top) and $Dy_2Ti_2O_7$ (bottom) at two temperatures. The standard deviation decreases monotonously with increasing number of transients included in the averaging. Fitting this to a power law form,

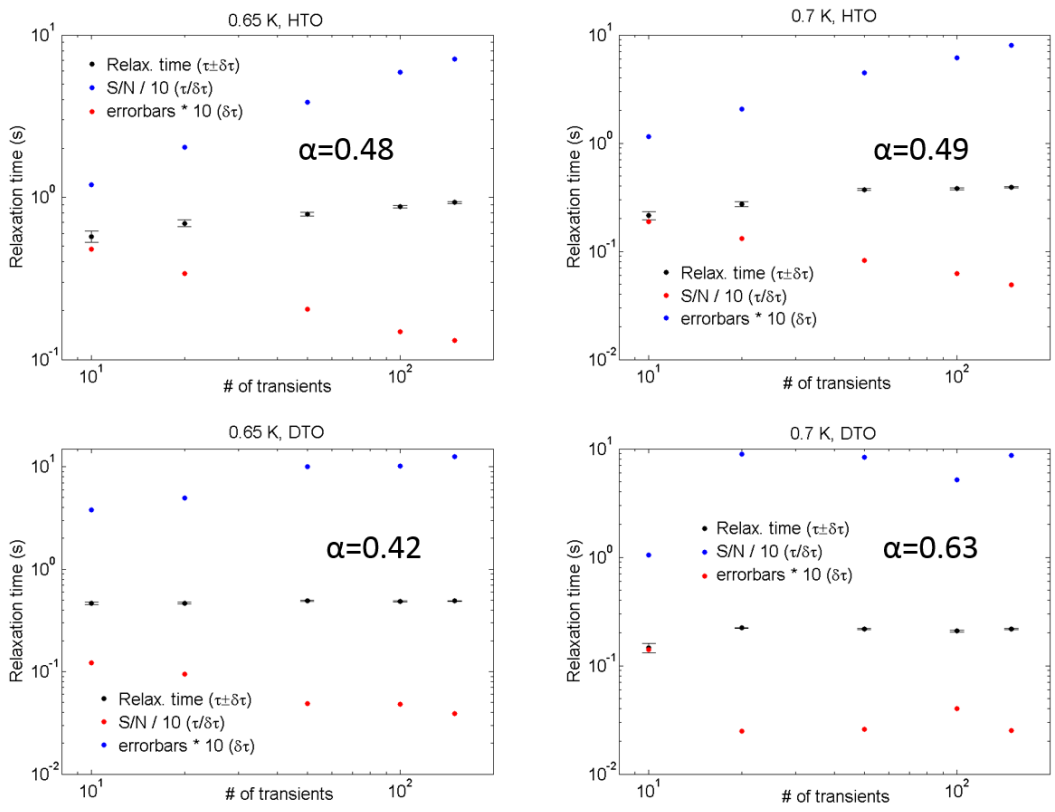


Figure 3.19: (Top) Relaxation time, standard deviation of the fit and the effective signal to noise ration (defined as $\tau/\delta\tau$) for $Ho_2Ti_2O_7$ at $T = 0.65K$ and $T = 0.7K$, (bottom) for $Dy_2Ti_2O_7$. Clear improvement of the fit quality and reduction of the standard deviation is seen. Fitting the deviation to a power law of the form $\delta\tau \sim N^{-\alpha}$ gives exponent very close to $1/2$, in agreement with the central limit theorem.

$\delta\tau \sim N^{-\alpha}$ gives the exponent very close to $\alpha = 1/2$ that is expected from the central limit theorem.

Fig. 3.20 depicts the averaged EMF measured from $Ho_2Ti_2O_7$ STS at different temperatures. The EMF transients after different current switching protocols, positive current on, positive current of, negative current on and negative current off are plotted separately. A uniform monopole current flowing under the constant external magnetic field should generate electric field similar to the Ampere's law for charge currents. This electric field can be identified by nonzero EMF generated in the circuit at long times after the application field, and the

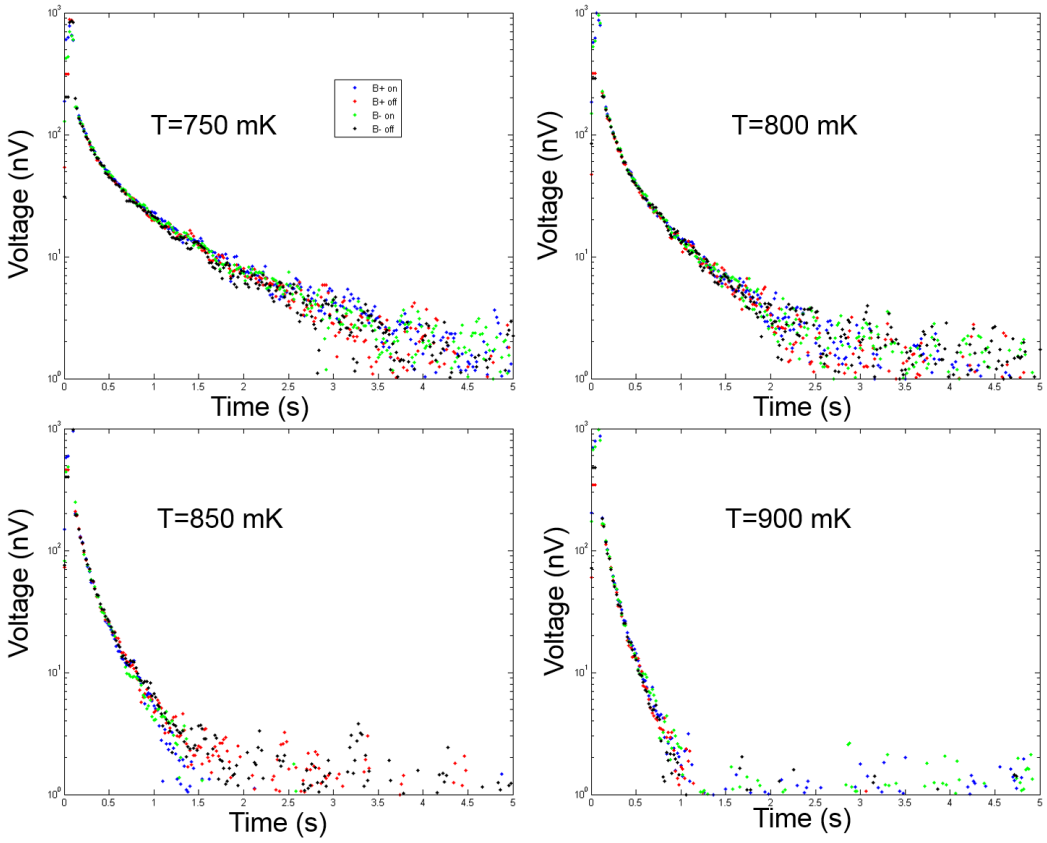


Figure 3.20: EMF transients after different current switching protocols at different temperatures. At all temperatures, EMF for different current switching protocols agree very well. Such symmetric behavior indicates that there is no uniform DC monopole current in these systems.

sign of the EMF will change when the direction of magnetic field is reversed. Since for all the measured temperatures, there was no difference between long time EMF corresponding to nonzero magnetic field and zero magnetic field, and between positive magnetic field and negative magnetic field, we deduce that uniform DC current of monopoles, as one might expect for electrons in an electrical circuit cannot be observed for the monopoles conjectured to exist in $Ho_2Ti_2O_7$ and $Dy_2Ti_2O_7$.

CHAPTER 4

# GLASS FORMING SPIN LIQUID DYNAMICS IN $HO_2TI_2O_7$ AND $DY_2TI_2O_7$

## 4.1 Time Domain Measurements

The magnetization dynamics theory based on monopole motion predicts that after application of an external field, the monopole current will decay like a simple exponential and magnetization of the system will reach the equilibrium magnetization also as a simple exponential (equations 2.16 and 2.17). However, the relaxation characteristics observed as the EMF generated in the STS show significant deviation from this behavior. We saw the first example for this in Fig. 3.19; here the vertical axis has logarithmic scale and a simple exponential decay corresponds to a straight line in such a diagram. We see that the decay characteristics follow a curve that is slower than a simple exponential, and a stretched exponential form has to be used to explain the relaxation properties accurately. Fig. 4.1 shows the EMF decay characteristics for STS wound around $Dy_2Ti_2O_7$ (top) and $Ho_2Ti_2O_7$ (bottom). Panels A and C show the decay properties, the smooth EMF decay down to zero is seen for both systems at all temperatures. Plotting the EMF on a vertical scale (panels B and D) we see that the EMF decay is slower than a simple exponential which corresponds to a straight line in this diagram. At long times, the decay becomes much slower than an exponential decay and has to be instead fitted to a Kohlrausch-Williams-Watts type stretched exponential described in section 1.4. The stretched exponential decay is slower than a simple exponential decay and indicates existence of a family of relaxation processes instead of just one.

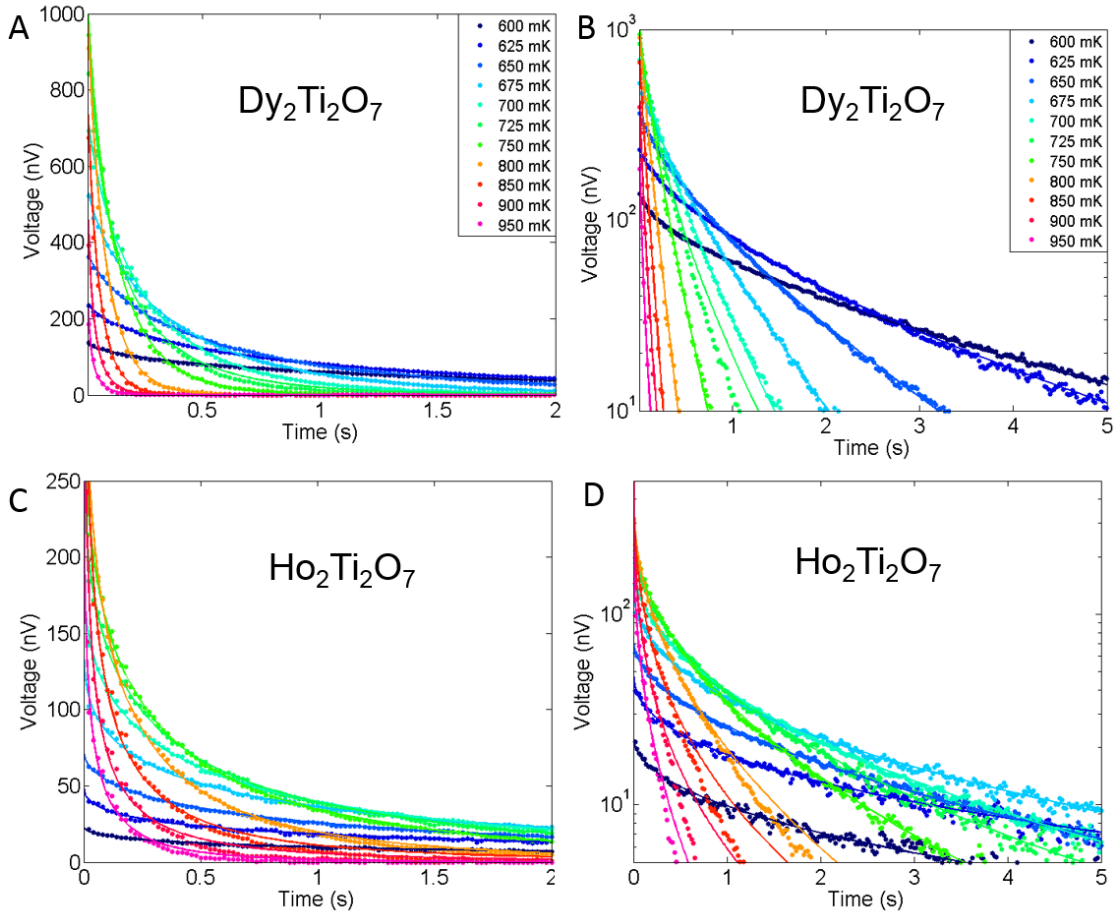


Figure 4.1: EMF generated over STS wound around $Dy_2Ti_2O_7$ (top) and $Ho_2Ti_2O_7$ (bottom) at different temperatures in the range 0.6 K-0.95 K. Smooth decay curves for both materials is clear. However, for both materials, the decay characteristics do not follow the simple exponential form predicted by a simple monopole theory. This is evident in the semilogarithmic plots in B and D, where at long times the EMF decay curve deviates from a straight line.

The solid lines in all the panels of Fig. 4.1 are the fits to stretched exponential form. Good agreement for all temperatures is seen for both magnetic systems. Fig. 4.2 depicts the stretching exponent $\beta$ for both materials. It is clearly seen that the exponent is significantly less than unity over the entire temperature range. This shows that stretched exponential form has to be used to fully describe the time dependent relaxation property of $Ho_2Ti_2O_7$ and $Dy_2Ti_2O_7$. Fig. 4.3 shows the residuals from fitting the EMF relaxation data to the stretched exponential

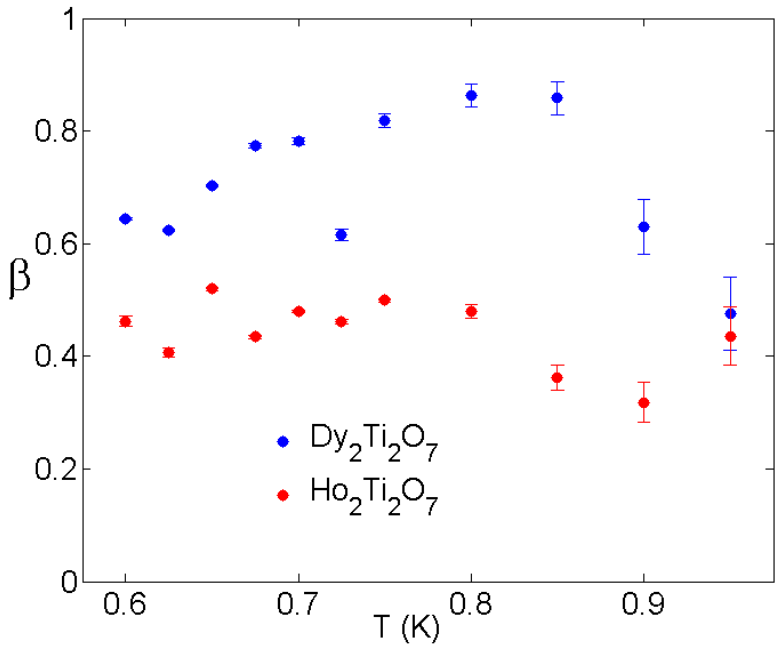


Figure 4.2: The stretching exponent $\beta$ for $Dy_2Ti_2O_7$ and $Ho_2Ti_2O_7$. At all temperatures, the stretching exponent is less than unity showing the necessity of consideration of the stretched exponential form compared to a simple exponential.

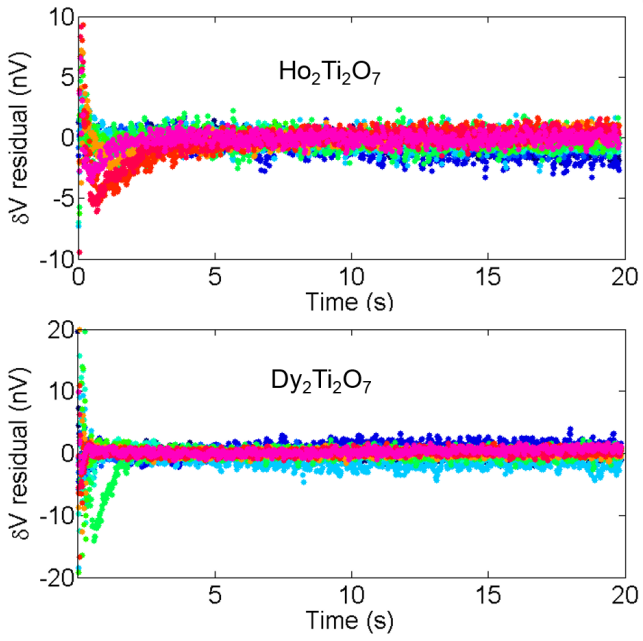


Figure 4.3: (top) Residuals of fitting the EMF relaxation data to stretched exponential form for $Ho_2Ti_2O_7$ and (bottom) for $Dy_2Ti_2O_7$.

form. The residuals are only ~ 10 nV compared to the signal amplitude which is up to a $\mu V$ in $Dy_2Ti_2O_7$.

To test the agreement with stretched exponential form

$$V(t) = V_0 e^{-(t/\tau_{KWW})^{\beta}} \tag{4.1}$$

over the entire temperature range more rigorously we plot the relaxation plots in such a way that temperature dependence of all fit parameters $V_0, \tau_{KWW}, \beta$ have been included. The parametrization $y = V(T)/V_0$ and $x = (t/\tau_{KWW})^{\beta}$ ensures that this choice of correcting for temperature dependence should collapse all of the experimental data onto a single function $y = \exp(-x)$. Fig. 4.4 depicts the data corrected for the temperature dependence in the procedure described above. We see that the EMF from all temperatures falls onto a straight line. This is a clear proof that KWW form of time domain relaxation is the correct description for relaxation of magnetization in $Ho_2Ti_2O_7$ and $Dy_2Ti_2O_7$.

## 4.2 Frequency Domain Measurements

The Ryzhkin theory based on monopole motion predicts that the AC susceptibility of magnetic systems like $Ho_2Ti_2O_7$ and $Dy_2Ti_2O_7$ should follow a Debye like form given by

$$\chi(\omega) = \frac{\chi_T}{1 + i\omega\tau}. \tag{4.2}$$

Before going through the details of comparing the AC susceptibility results to this prediction, we note that there is a simple test to see whether AC susceptibility follows this form or not. For the system with AC susceptibility given by this relation, the real and imaginary parts will be related such that

$$\frac{\chi''}{\chi'} = \omega\tau \propto \omega. \tag{4.3}$$

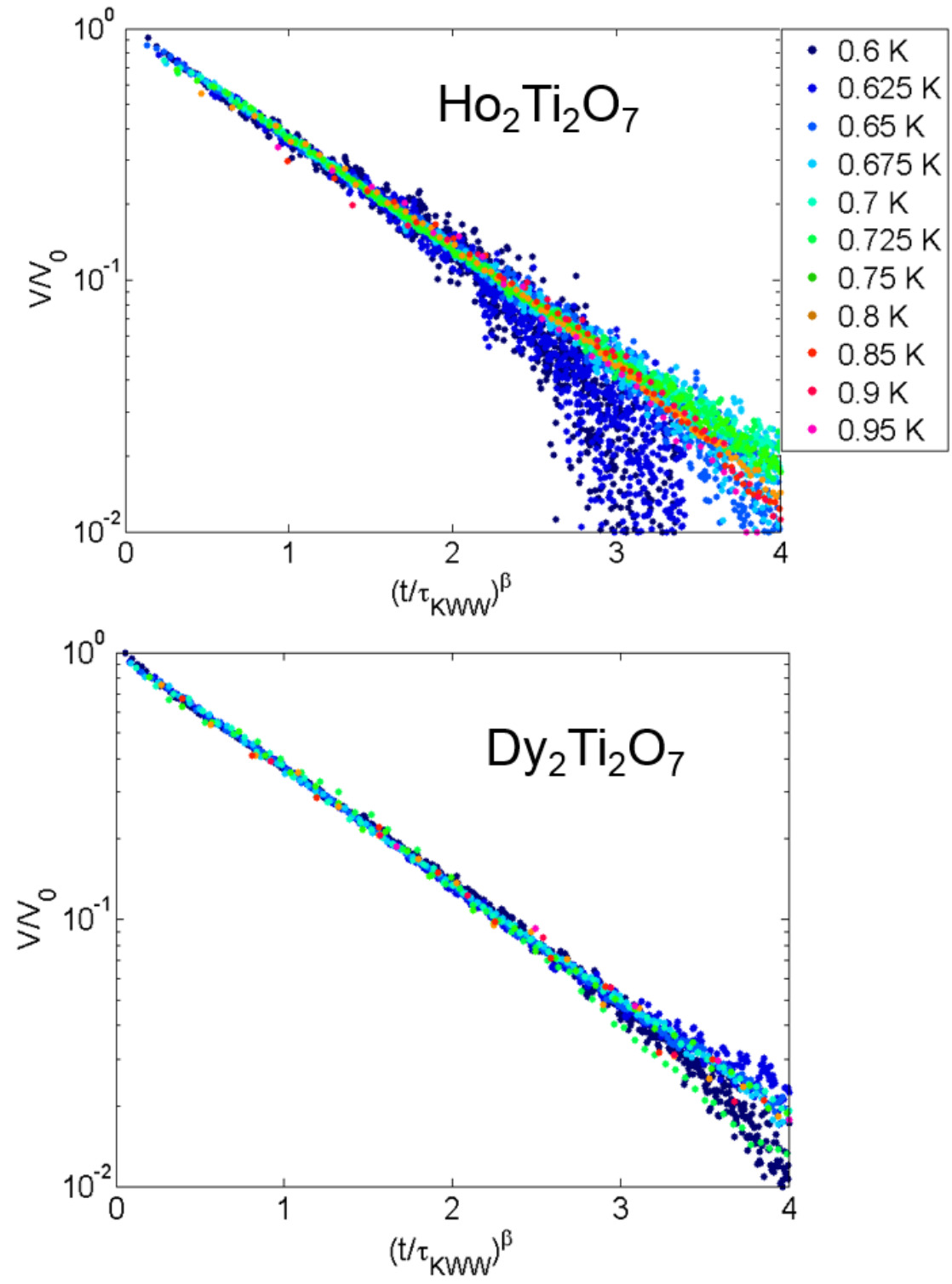


Figure 4.4: (top) Collapse of all the time domain relaxation data onto the KWW form for $Ho_2Ti_2O_7$ and (bottom) for $Dy_2Ti_2O_7$. This is a clear indication that KWW form is the correct description of magnetization relaxation in $Ho_2Ti_2O_7$ and $Dy_2Ti_2O_7$.

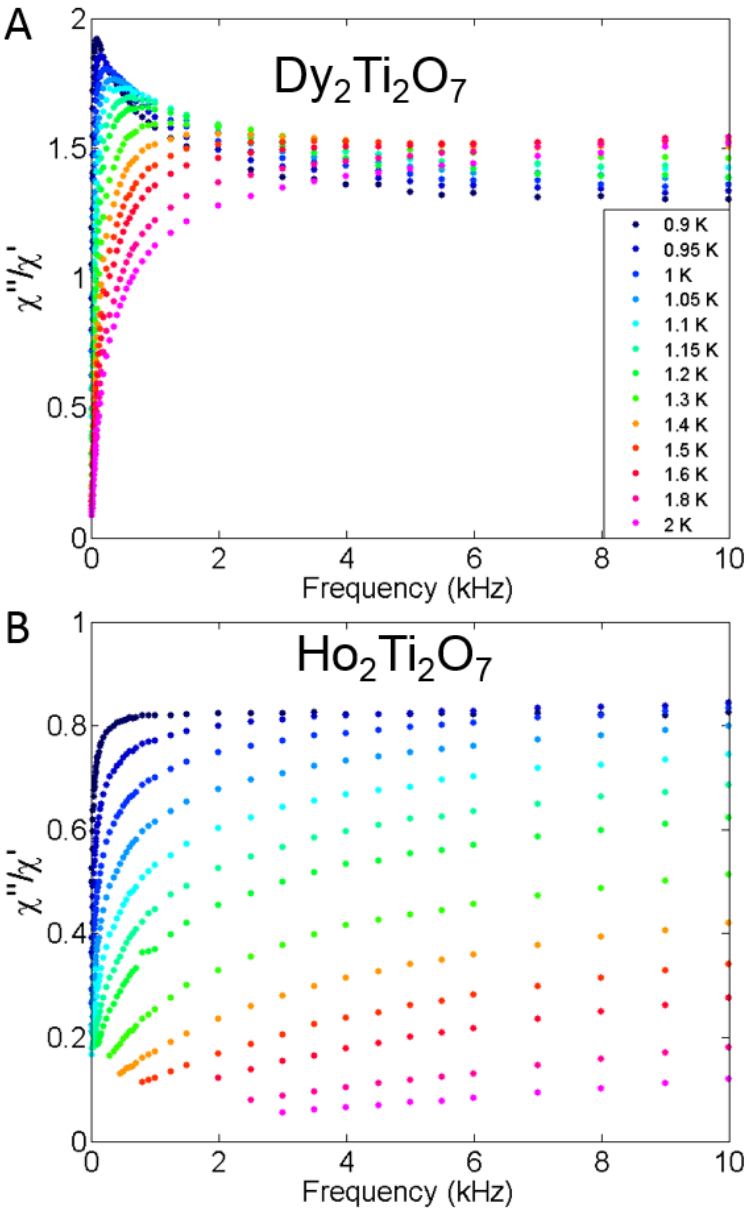


Figure 4.5: Ratio of imaginary part of susceptibility to real part of suceptibility $\chi''/\chi'$ for $Dy_2Ti_2O_7$ (A) and $Ho_2Ti_2O_7$ (B). Only at low frequencies the ratio can be described as a straight line. For most of the frequency range, this assumption fails and Eqn. 4.2 cannot be used to accurately fit the AC susceptibility results.

Then, plotting the ration of imaginary part of susceptibility to the real part against frequency should give a straight line. Fig. 4.5 depicts this ratio plotted against frequency for both magnetic systems. We see that there are significant

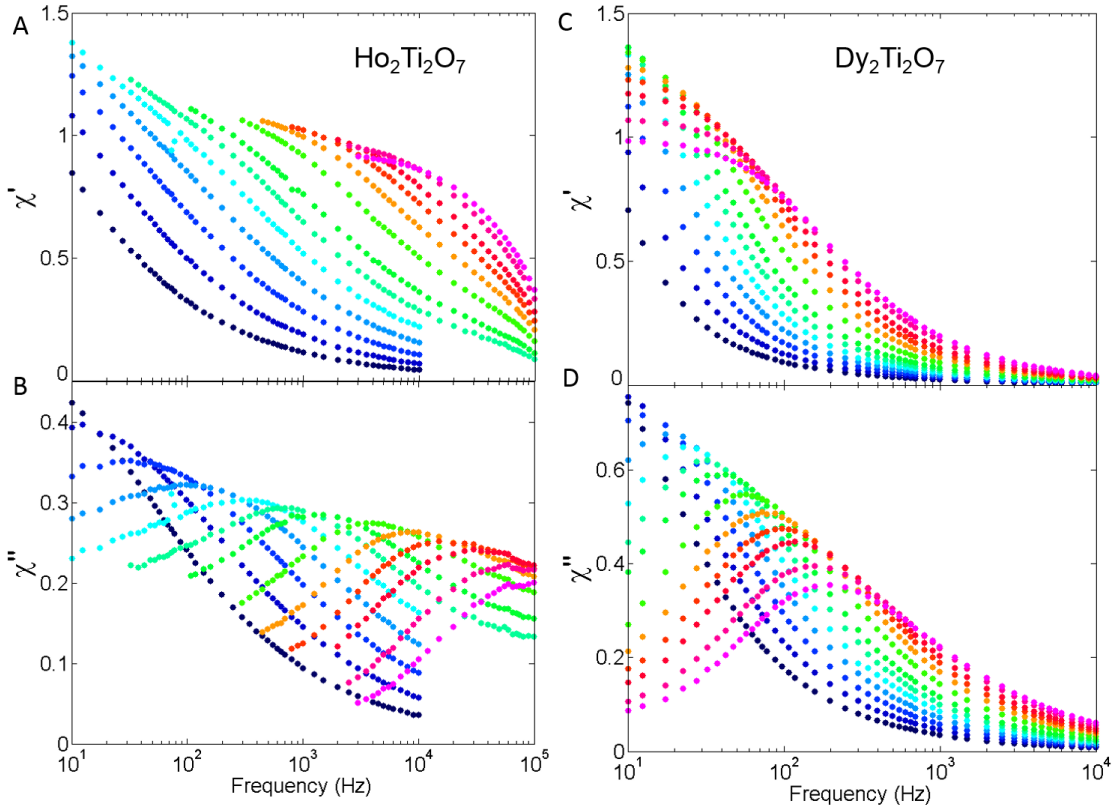


Figure 4.6: Real (A) and imaginary (B) components of susceptibility of $Ho_2Ti_2O_7$ and (C,D) $Dy_2Ti_2O_7$.

deviations from straight line expected from Ryzhkin model. This means that prediction of the simple monopole dynamics is not sufficient to explain the AC susceptibility and more elaborate functional forms must be used.

Fig. 4.6 depicts the real and imaginary susceptibility of $Ho_2Ti_2O_7$ (A,B) and $Dy_2Ti_2O_7$ (C,D). Monotonous decay of the real part of susceptibility with frequency and clear peak in the imaginary part is observed for both materials. Since the form predicted by Ryzhkin model, Eqn. 4.2, is not sufficient to explain the AC susceptibility, we try the more general Havriliak-Negami (HN) form described in section 1.4 for the analysis.

$$\chi(\omega) = \chi_\infty + \frac{\chi_0}{[1 + (i\omega\tau_{HN})^\alpha]^\gamma} \tag{4.4}$$

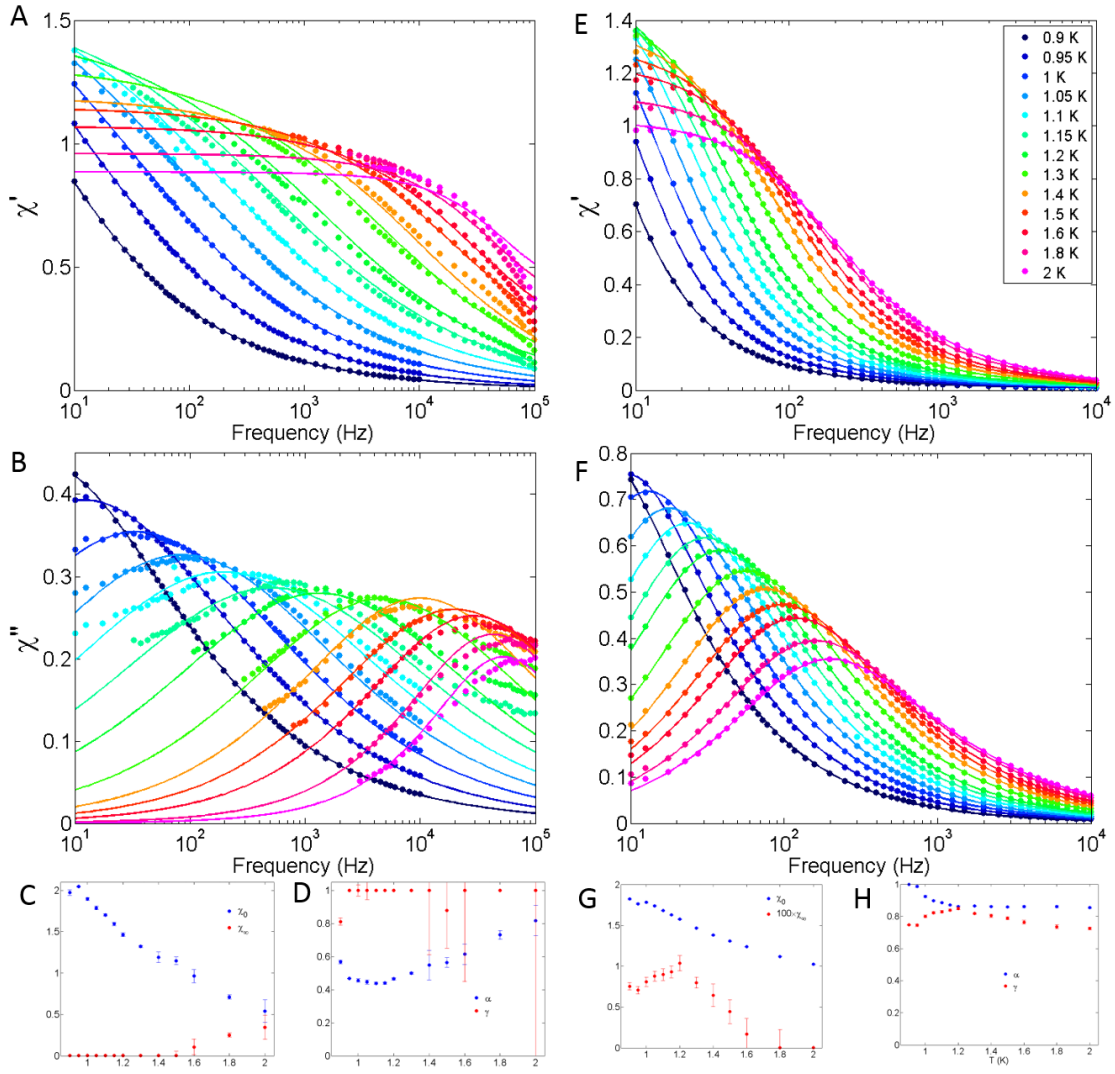


Figure 4.7: (A,B) AC susceptibility of $Ho_2Ti_2O_7$. Solid lines show the fits to HN form. (C,D) Temperature dependence of the fit parameters. (E,F,G,H) AC susceptibility data, fits and temperature dependence of the fit parameters for $Dy_2Ti_2O_7$.

An additional coefficient $\chi_\infty$ (also sometimes denoted as $\chi_S$ for adiabatic susceptibility) is the adiabatic susceptibility included to explain the nontrivial deformation of the phase phase along the direction of the external field [93].

Fig. 4.7 depicts the fits of both real and imaginary parts of AC susceptibility to the HN form given by Eqn. 4.4 simultaneously for both $Ho_2Ti_2O_7$ ad $Dy_2Ti_2O_7$. The temperature dependence of the fit parameters is shown in the bottom panels

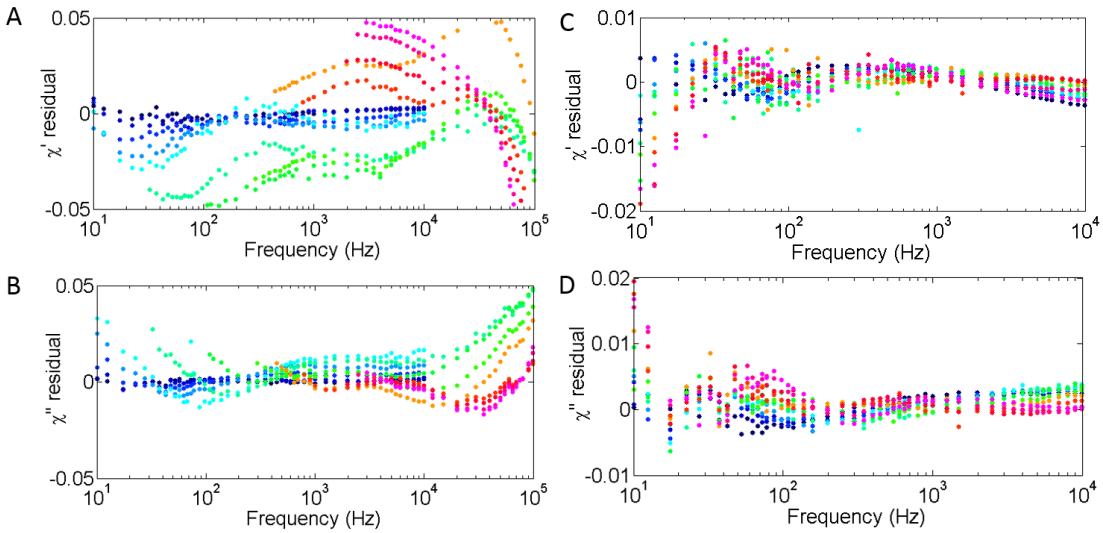


Figure 4.8: Residuals of fits of AC susceptibility data to HN form for $Ho_2Ti_2O_7$ (A,B) and for $Dy_2Ti_2O_7$ (C,D).

C,D,G,H. For both magnetic systems, we see that at least one of the exponents $\alpha$,$\gamma$ is less than unity. This justifies the general analysis of the AC susceptibility to account for the deviations from the Eqn. 4.2. The residuals of the fit are shown in Fig. 4.8. Residuals are smaller for the $Dy_2Ti_2O_7$ data than for $Ho_2Ti_2O_7$. This maybe due to relative difficulty in growing the $Ho_2Ti_2O_7$ single crystals and the data for the susceptibility of $Ho_2Ti_2O_7$ likely to have more extraneous details coming from the growth quality.

Similar to the time domain results, we want to check unambiguously whether the HN form given in Eqn. 4.4 is the correct fit for all temperatures. The size of residuals gives us some confidence, however we try a functional transform of the data of correct for the temperature dependence of all the fit parameters and see whether the data from all temperatures will fall onto a single line. The HN form for AC susceptibility has four parameters on top of the relaxation time that we have to correct for, $\chi_\infty, \chi_0, \alpha$ and $\gamma$. The basic form

$$\chi' - i\chi'' = \chi_\infty + \frac{\chi_0}{[1 + (i\omega\tau_{HN})^\alpha]^\gamma} \tag{4.5}$$

can be converted to

$$\frac{\chi' - i\chi'' - \chi_\infty}{\chi_0} = \frac{1}{[1 + (i\omega\tau_{HN})^\alpha]^\gamma} \tag{4.6}$$

to account for the temperature dependence of the coefficients $\chi_0$ and $\chi_\infty$. We can go a step further and correct for the temperature dependence of the assymmetry exponent $\gamma$

$$G(\chi) = \left[\frac{\chi' - i\chi'' - \chi_\infty}{\chi_0}\right]^{1/\gamma} = \frac{1}{1 + (i\omega\tau_{HN})^\alpha} = \frac{1 + (\omega\tau_{HN})^\alpha(\cos\frac{\pi\alpha}{2} - i\sin\frac{\pi\alpha}{2})}{1 + 2(\omega\tau_{HN})^\alpha + (\omega\tau_{HN})^{2\alpha}}. \tag{4.7}$$

Then, plotting the real part of $G(\chi)$ should collapse all the data onto a line described by

$$\frac{1 + (\omega\tau_{HN})^\alpha \cos\frac{\pi\alpha}{2}}{1 + 2(\omega\tau_{HN})^\alpha + (\omega\tau_{HN})^{2\alpha}} \tag{4.8}$$

and the imaginary part of $G(\chi)$ should collapse all the data from different temperatures onto a line

$$-\frac{(\omega\tau_{HN})^\alpha \sin\frac{\pi\alpha}{2}}{1 + 2(\omega\tau_{HN})^\alpha + (\omega\tau_{HN})^{2\alpha}}. \tag{4.9}$$

Fig. 4.9 depicts the AC susceptibility data corrected for the temperature dependence of fit parameters according to the Eqn. 4.7. For $Dy_2Ti_2O_7$ an excellent collapse of all the data onto a single line is seen, while there are some deviations in the collapse of $Ho_2Ti_2O_7$ data. This is likely because of the large variation of the $\alpha$ exponent in $Ho_2Ti_2O_7$ over the temperature range compared to relatively stable value for $Dy_2Ti_2O_7$. These variations will shift the curves left or right. However, we see that even $Ho_2Ti_2O_7$ data collapses onto single line quite well.

In Chapter 1 it was presented that the Kohlrausch-Williams-Watts stretched exponential form for time domain relaxation and Havriliak-Negami form for AC susceptibility are two of the key dynamical identifiers of the supercooled or glass forming liquids. These forms are complements of each other, that Fourier transform of one function gives the other and in their respective domains they both correspond to a general distribution of relaxation times in the system. Seeing the significant similarity between the dynamics of spins in $Ho_2Ti_2O_7$ and

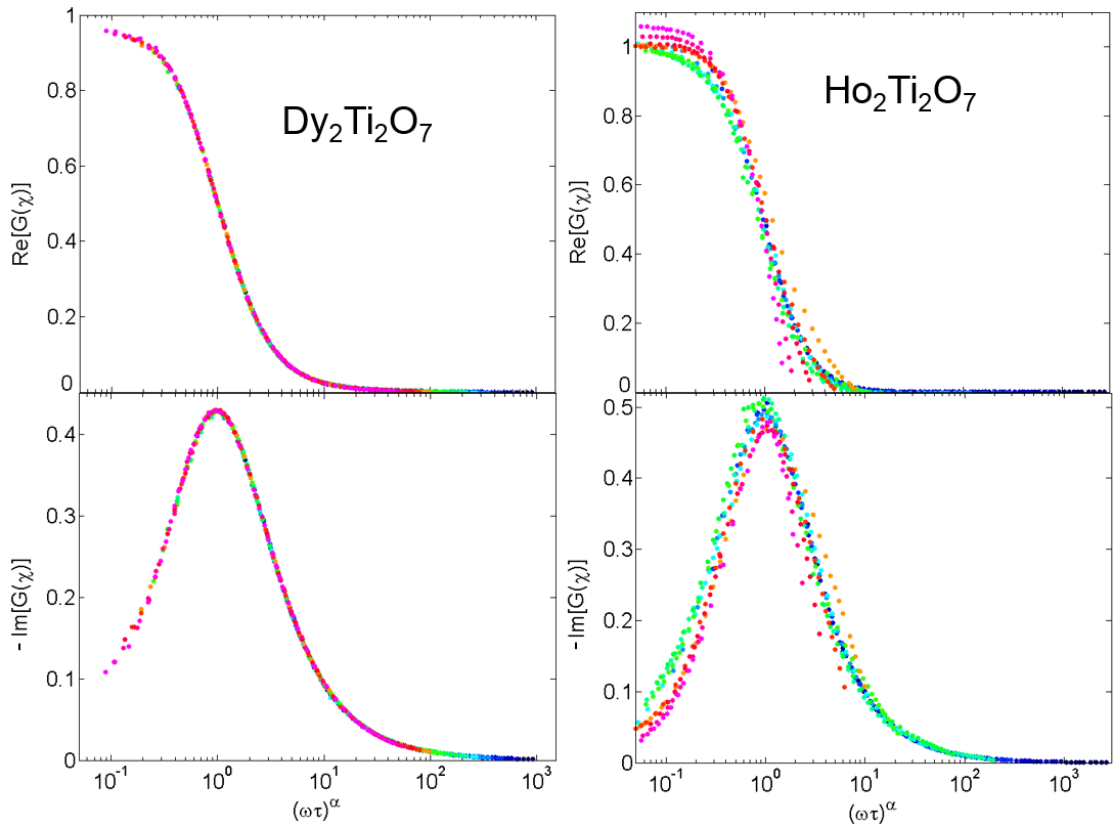


Figure 4.9: (Left) Collapse of the AC susceptibility on the function given in Eqn. 4.7 for $Dy_2Ti_2O_7$ and (Right) for $Ho_2Ti_2O_7$.

$Dy_2Ti_2O_7$, we want to check whether the third dynamical property of the glass forming liquids, the divergence of relaxation times along the Vogel-Tammann-Fulcher (VTF) trajectory is valid for the relaxation time results in these materials.

## 4.3 Unified Analysis

To analyze the relaxation time data obtained from different measurements, time domain and frequency domain, we need to be able to confidently convert from one set of data to the other. Numerical studies have found that it is possible to obtain the parameters of frequency domain function in terms of those in the

time domain with the following relations

$$\ln\left(\frac{\tau_{HN}}{\tau_{KWW}}\right) = 2.6(1-\beta)^{0.5}\exp(-3\beta) \tag{4.10}$$

$$\alpha\gamma = \beta^{1.23}. \tag{4.11}$$

However, these are obtained by generating time domain relaxation, numerical Fourier transform to obtain the response function in frequency space fitted to HN form, and the obtained parameters are parametrically fitted to get a relation. To improve the quality of conversion, we instead use the table generated in [42] and estimate the ratio $\tau_{HN}/\tau_{KWW}$ by piecewise linear fitting the obtained $\beta$ parameters to the numerical result.

Fig. 4.10A depicts the relaxation time data plotted against the inverse temperature. The data from both AC susceptibility and time domain relaxation experiments are included in this diagram. The horizontal axis is chosen as inverse temperature. This is a useful method of plotting the relaxation time data, because commonly the systems following Arrhenius type activation show a straight line when relaxation time is plotted against $1/T$. We see that both for $Ho_2Ti_2O_7$ and for $Dy_2Ti_2O_7$ relaxation time data does not fall on a straight line, but in fact as the temperature is lowered the rate at which the relaxation time diverges becomes larger. Such faster than Arrhenius divergence of relaxation time is common in supercooled liquids and is usually fit to VTF form described in section 1.4

$$tau(T) = \tau_0 \exp\left(\frac{DT_0}{T-T_0}\right). \tag{4.12}$$

Here $\tau_0$ is the attempt frequency, $T_0$ is the temperature at which relaxation time is extrapolated to diverge (also known as VTF temperature or Kauzmann temperature) and $D$ is the fragility parameter. In this parametrization an Arrhenius type relaxation would correspond to $T_0 = 0$ and $DT_0 = E$ the activation energy. As was discussed in section 1.4, for strong liquids Arrhenius law is frequently

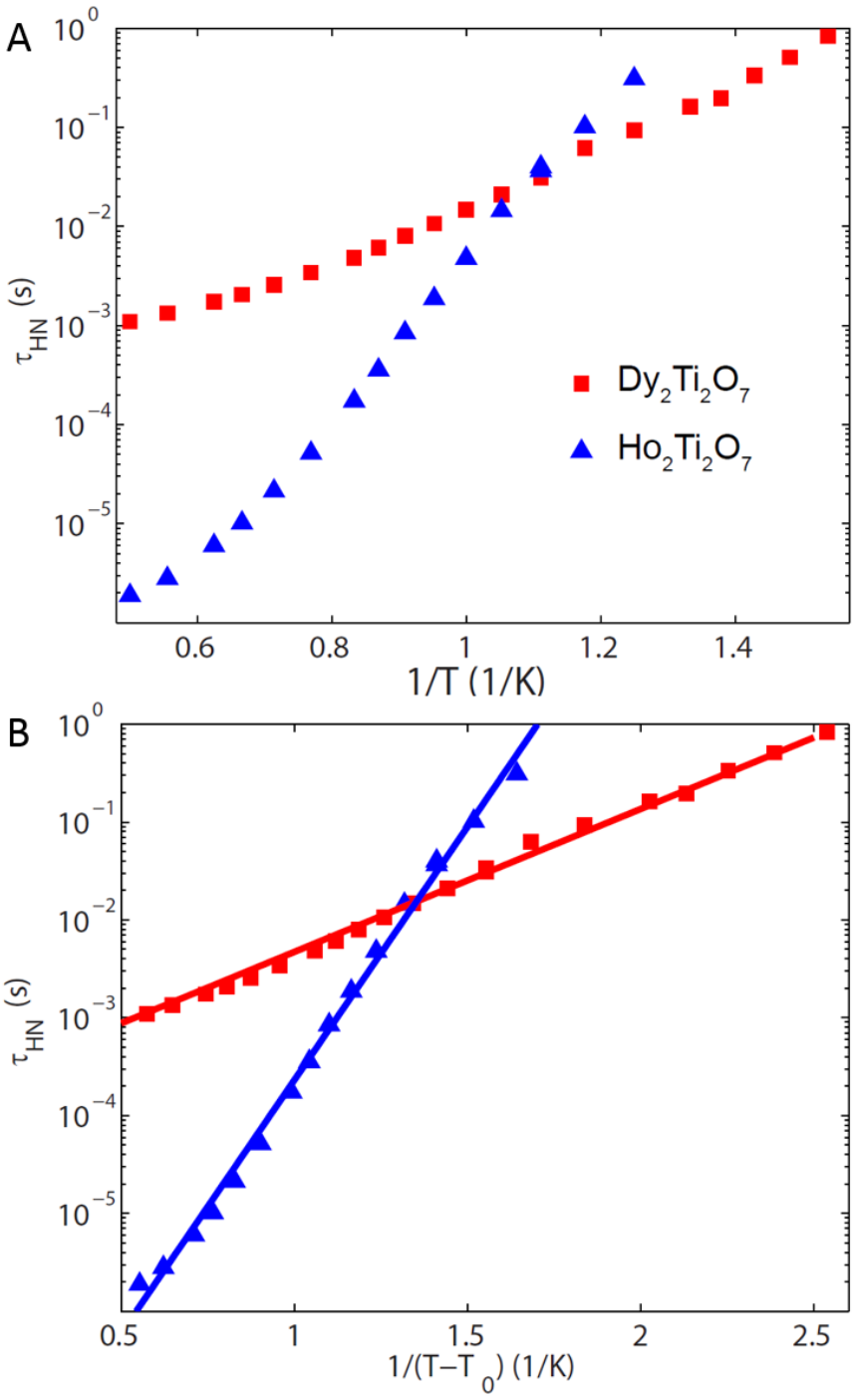


Figure 4.10: (A) The relaxation time vs temperature for $Ho_2Ti_2O_7$ and $Dy_2Ti_2O_7$ obtained from AC susceptibility and time domain relaxation measurements. The temperature dependence does not follow a straight line when the horizontal axis is made inverse temperature, which shows the Arrhenius relation is insufficient to explain the relaxation time data. (B) The horizontal axis is modified to include the effects of nonzero divergence temperature $T_0$ also known as VTF temperature or Kauzmann temperature.

a sufficient description and $D$ approaches infinity for these systems. Fitting the relaxation time data to VTF relation gives $\tau_0 \approx 8 \cdot 10^{-10}$s, $D \approx 60, T_0 \approx 191$ mK for $Ho_2Ti_2O_7$ and $\tau_0 \approx 1.4 \cdot 10^{-4}$s, $D \approx 14, T_0 \approx 257$mK. To show the agreement of relaxation time data with VTF relation, the horizontal axis is changed to $1/(T - T_0)$ in Fig. 4.10B. A clear straight line is seen for both materials proving that the VTF form is the correct description for the divergence of relaxation time in both systems. The KWW relaxation, HN susceptibility and VTF divergence of relaxation times shows that the magnetic state in $Ho_2Ti_2O_7$ and $Dy_2Ti_2O_7$ has to be classified as a supercooled liquid state, but different from the other supercooled liquids like liquid silica or supercooled water, in these systems the supercooled liquid dynamics are created by the magnetic interactions.

This is the first evidence for existence of supercooled liquid state in a system with magnetic interactions. Spin glasses (discussed in section 1.6) have been the most popular magnetic states where frustration and competition between interactions do not let the system reach a clear low temperature state. Early work in $Ho_2Ti_2O_7$ and $Dy_2Ti_2O_7$ had also concentrated on determining whether the magnetic state can be identified as the spin glass. However, key identifiers of spin glass phase like the cusp in AC susceptibility is absent in these systems. Additionally, in spin glasses the temperature at which the discrepancy between FC and ZFC magnetization starts decreases when the applied external field is increased. Similar studies performed on $Dy_2Ti_2O_7$ have shown that this temperature is very weakly dependent on the external field and contrary to spin glass behavior, increases with the increasing field. [31] These results have removed spin glass as a possible explanation for the dynamics of pure $Dy_2Ti_2O_7/Ho_2Ti_2O_7$. The doped materials however have shown spin glass like behavior, since now randomness which is another key ingredient in the devel-

opment of spin glass behavior can be introduced with doping. [100], [52], [50]
The magnetic state, which at this point must be called a supercooled spin liquid state is very similar to the supercooled liquids based on the dynamical evidence presented here. At low temperatures, the magnetic system falls out of equilibrium and different parts of the system is segmented into regions with local dynamics. Based on empirical evidence, for both systems when the temperature is as low as $T_0 \approx 200$ mK, the system will be completely out of equilibrium.
It is important to also consider the significant difference between the VTF fit parameters of $Ho_2Ti_2O_7$ and $Dy_2Ti_2O_7$. Even though both systems are expected to completely fall out of equilibrium by around 200 mK, the attempt frequency and the fragility are vastly different between the two systems. The attempt frequency corresponds to the frequency of transition between different states at some high temperature. However, this high temperature value is not a room temperature value that one would expect from a simple activation picture. The relaxation time in these systems at high temperatures was observed to follow Arrhenius law, but with activation energy of ~300 K, comparable to the energy gap created by the crystal field. [31], [101] At high temperatures, the spin flip is thermally activated over this large energy barrier. At intermediate temperatures however, 5-10 K, there is a plateau in the relaxation time (Fig. 4.11), and below 5 K the effective energy for the magnetization dynamics is only a few Kelvins ($DT_0 \approx 3.5K$ for $Dy_2Ti_2O_7$, $DT_0 = 12K$ for $Ho_2Ti_2O_7$). This is a much smaller value than the gap created by the crystal field, and has the same energy range as the energy difference between an ice rule following state and a state with three spins pointing in and one spin pointing out (or one spin pointing in and three spins pointing out). This deviation from the high temperature Arrhenius behavior happens because at intermediate temperature, the spin flips

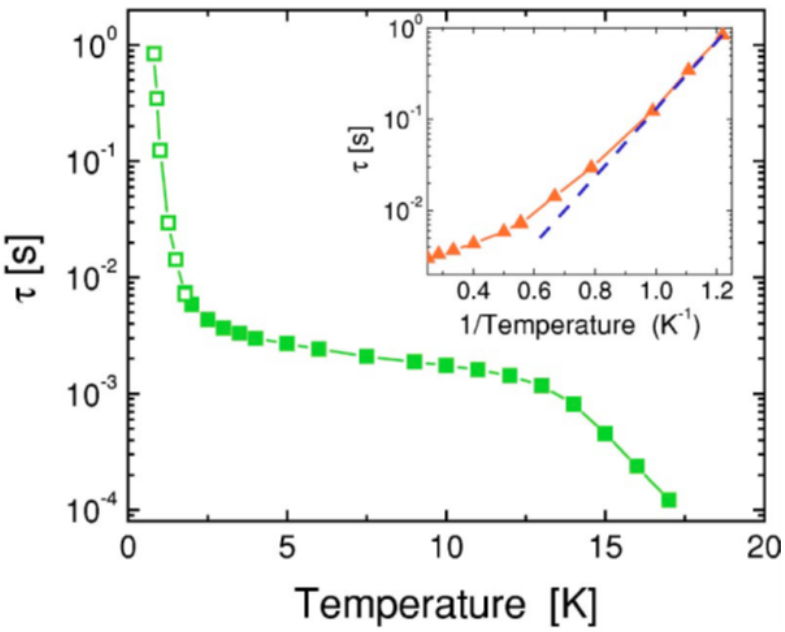


Figure 4.11: Relaxation time of $Dy_2Ti_2O_7$for temperatures $T < 20K$. In the temperature range 5-10 K, the relaxation time has very weak temperature dependence indicating quantum mechanical contribution to the transition between two spin states. From [31]

happen due to quantum mechanical transitions. At the intermediate region, the weak dependence of relaxation time on temperature can be explained as quantum mechanical effects driving the dynamics, and the low temperature relaxation property is determined by the correlated spin dynamics because now spins have to break ice rules in order for the system to relax.

The attempt frequency that we have found corresponds to the relaxation time at the intermediate temperatures where the relaxation time has a plateau and is in good agreement with previous work [31], [101], [94], [102]. Theoretical work has shown that the quantum mechanical transitions are mainly determined by the transverse fields. [14] In these systems the dipolar interaction acts as a transverse field. $Ho_2Ti_2O_7$ has both singlet and doublet energy levels for different orientations of its spins, and the energy gap created by the transverse field is proportional to the square of the field. $Dy_2Ti_2O_7$ on the other hand only has

doublets and all of the matrix elements corresponding to the effects proportional to the square of the field cancel out in it. The dominant contribution of the transverse fields in $Dy_2Ti_2O_7$ is proportional to the cube of the field and is weaker at low field than for $Ho_2Ti_2O_7$. This explains why the attempt frequency is much larger in $Ho_2Ti_2O_7$ compared to $Dy_2Ti_2O_7$.

To explain the difference between the fragility of the supercooled spin liquid in the two materials ($D \approx 14$ for $Dy_2Ti_2O_7$, $D \approx 60$ for $Ho_2Ti_2O_7$; the spin liquid in $Dy_2Ti_2O_7$ is more fragile) we first remind that fragility quantifies the heterogeneity in the supercoled liquid. [2] The liquids with higher fragility parameter have different parts trapped in greater number of different metastable states and relax separately. We can use the dynamics of the monopoles to shed light onto difference in fragility. The monopoles correspond to spin flips from the ice rule following two in two out state. From this definition, we expect that a monopole motion is only guaranteed if a spin can flip in the direction of the monopole motion. However, if a spin flips once for one monopole, this will block all future monopoles from taking the same path. This will result in different parts of the system gradually losing causal connection with each other. Based on the monopole theory, the energy barrier to the creation of monopoles is $\Delta = 5.6K$ in $Dy_2Ti_2O_7$and $\Delta = 8.5K$ in $Ho_2Ti_2O_7$. Such a difference between energy barriers will results in much larger quantity of monopoles in $Dy_2Ti_2O_7$ compared to $Ho_2Ti_2O_7$ in the temperature range of our experiments. The larger density of monopoles will force the spin system in $Dy_2Ti_2O_7$ out of equilibrium faster, and make it more fragile.

CHAPTER 5

# MONOPOLE ANNIHILATION DYNAMICS

So far, we only used the fact that monopoles in $Ho_2Ti_2O_7$ and $Dy_2Ti_2O_7$ will divide the system into distinct regions and make the magnetic liquid heterogeneous and fragile. The predictions of the simple monopole dynamics like exponential decay of magnetization current (which is proportional to EMF generated in the STS) and Debye-like AC susceptibility do not explain the experimental data. This is because the assumptions assume free monopoles that can travel far and possibly reach the edge of the material. The correlations between monopoles, like whether two monopoles can occupy the same tetrahedron or not, and whether two monopoles can travel through the same path or not are ignored in these predictions. These effects must be included to get a self consistent description of the magnetization dynamics and monopole theory simultaneously.

Here we briefly talk about one possible model that can explain the stretched exponential relaxation in time domain, and consequently the HN form of AC susceptibility as the two forms are tied to each other by a Fourier transform [42]. The mainstream theory to describe monopole dynamics is Ryzhkin theory [88], [93], which assumes that monopoles travel to very long distances without any challenges. However, in reality, an initial density of monopoles will decrease with time if these quasiparticles encounter and annihilate with their antiparticles. [108] The energy released from this process will simply go to the heat bath that the system is equilibrated with (the cryostat stage), and the constant contact with the heat bath will make sure there is some thermal density of monopoles at all times as long as the applied external field is not too strong to completely magnetize the material.

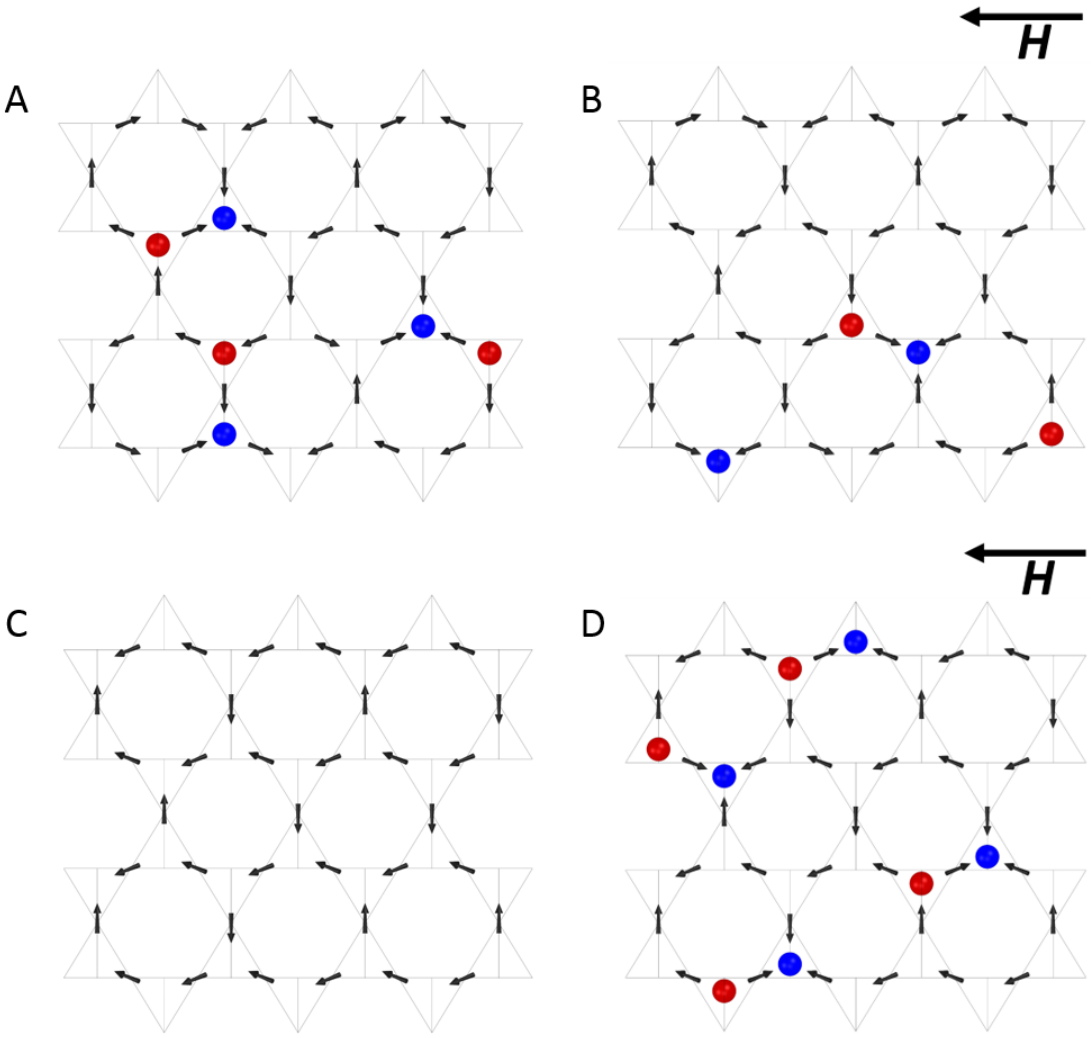


Figure 5.1: Sketch of monopole annihilation dynamics. (A) A possible initial configuration of the system corresponding to some density of positive (blue0 and negative (red) monopoles. (B) Under external field, the monopoles motion will resemble a biased random walk, until a positive and negative monopoles meet and annihilate. (C) A possible final configuration of the system where spins are mostly aligned with the external field. (D) The thermal density of monopoles from the magnetized state will mostly annihilate due to the preferential motion in external field and the contribution to the monopole current in the system will be too small to detect.

We use the model that was originally developed to explain radiation free exciton annihilation in amorphous semiconductors [38], modified to explain the monopole dynamics. In this model, an initial collection of thermal monopoles travel as a random walk until it is annihilated by an antimonopole, (Fig. 5.1). The monopoles will move around in a motion that can be described as random walk, with slight bias due to the external field applied to the system. This process will continue until the materially is magnetized in the direction of the external field. The thermal density of monopoles created from this partially magnetized state will mostly annihilate immediately and not contribute to the monopole current. Assuming a thermal density of monopoles and antimonopoles to be the same (since a spin flip from ice rule following state creates a monopole and antimonopole simultaneously, the density of the two oppositely charged quasiparticles is expected to be the same) and equal to $N_T$, the probability for a monopole to encounter $k$ antimonopoles in a spherical volume $v = C_d R^d$ ($C_d$ is the dimensional coefficient from the calculation of the volume of a sphere in $d$ dimensions, $C_2 = \pi$, $C_3 = 4\pi/3$) will be given with a Poisson distribution

$$P(k) = \frac{N^k}{k!} e^{-N} \tag{5.1}$$

where $N = N_T v = N_T C_d R^d$ is the average number of monopoles or antimonopoles in a volume $v$. Probability of not encountering any annihilation partner, i.e. probability of not annihilating is then

$$E = P(0) = \exp(-N) = \exp(-N_T C_d R^d). \tag{5.2}$$

The probability of the monopoles to be within this sphere of radius $R$ at time $t$ is given by the solution of the diffusion equation [109]

$$P(R,t) = |\phi_0|^2 \exp\Big(-\frac{D}{R^2}\gamma_d t\Big). \tag{5.3}$$

Here $\gamma_d$ is another number that only depends on the dimensionality of the system ($\gamma_2 = 5.78, \gamma_3 = \pi^2$) and $|\phi_0|^2$ is the normalization constant. The survival probability of a monopole that has managed to travel in a sphere of radius $R$ without annihilation is then product of the two expressions above

$$S(R,t) = |\phi_0|^2 \exp\left[ - N_T C_d R^d - \frac{D}{R^2}\gamma_d t \right]. \tag{5.4}$$

To get the limiting distribution at long times, we integrate over all possible paths $R$ in the system

$$S(t) = \int dR S(R,t) \tag{5.5}$$

The integrand will be dominated by the smallest value of the exponent which corresponds to $R = \left(\frac{2\gamma_d}{dC_d}\frac{Dt}{N_t}\right)^{1/(d+2}$, and using the saddle point approximation the dominant time dependence is given by

$$S(t) = S_0 \exp\Big( - \alpha N_T^{\frac{2}{d+2}} (Dt)^{\frac{d}{d+2}} \Big) \tag{5.6}$$

where $\alpha = (1+\frac{2}{d})\gamma_d^{d/(d+2)}(\frac{dC_d}{2})^{d/(d+2)}$ is a convenient way to express all the numbers that only depend on the dimension of the system. The density of the monopoles at time $t$ will be proporional to this survival probability and can be written as

$$n(T,t) = n_0 \exp\Big( - \alpha N_T^{\frac{2}{d+2}} (Dt)^{\frac{d}{d+2}} \Big). \tag{5.7}$$

Here $n_0$ is the initial density of the monopoles that contribute to the current. The analysis followed in later paragraphs shows that the empirically determined density of monopoles which contribute to monopole current is different and much less than the thermal monopole density estimated from the theory and heat capacity experiments. Eqn. 5.7 makes two key predictions about the dynamics of the system determined by the annihilation process. First, the stretching exponent in KWW form only depends on the dimensionality of the system as $\beta = \frac{d}{d+2}$. Second, if we write Eqn. 5.7 as the stretched exponential form

$$n(T,t) = n_0 \exp(-(t/\tau)^\beta) \tag{5.8}$$

then, the relaxation time of the system is determined by the density of the monopoles $\tau \sim N_T^{-2/d}$.

For monopole motion in three dimensional materials similar to the systems we study, one then expects $\beta = 3/5$, however, the above derivation assumed that the particles interact only with short range forces. For a system like the monopole fluid that is expected to interact with long range Coulomb interaction, the dimensionality is halved $d^* = d/2$ and the critical stretching exponent becomes $\beta = 3/7$. [38] For a glassy system described by this theory, at high temperatures the stretching exponent is indistinguishable from unity. As the temperature is reduced, the stretching exponent decreases because the phase space volume becomes more constricted and stabilizes at the topological value $\beta = d/(d+2)$ when the system becomes a glass. [38]

Since the density of the monopoles which contribute to monopole current decreases with time, the conductivity of monopoles that enters Ryzhkin equation in Eqn. 2.14 will also decrease with time resulting in a slower than simple exponential decay. For a general time dependent conductivity $\sigma(t) = n(T,t)Qu$ where $Q$ is the monopole charge and $u$ is the monopole mobility, the Ryzhkin equation can be exactly solved. The resulting expression for the time dependent magnetization and monopole current is

$$M(t) = \chi_T H\left[1 - \exp\left(-\int_0^t \frac{\sigma(t')\mu_0}{\chi_T} dt'\right)\right] \tag{5.9}$$

$$J(t) = \mu_0 \sigma(t) H \exp\left[-\int_0^t \frac{\sigma(t')\mu_0}{\chi_T} dt'\right]. \tag{5.10}$$

In Eqn. 5.10 the time dependence of the monopole current has two contributions, directly from the time dependence of conductivity and from the integral in the exponent. For this reason, in general the relaxation time and the strech-ing exponent used to describe the monopole current will be different from the

relaxation time and the stretching exponent used for the conductivity or the monopole density. Since monopole current is the time derivative of magnetization, the EMF generated in the STS during the time domain measurements is directly proportional to the monopole current.

$$V = -\mu_0 NA\frac{dM}{dt} = -\mu_0 NAJ(t). \tag{5.11}$$

Then, the stretching exponent reported in Fig. 4.2 describes the time dependence of the monopole current as well. To get time dependence of the conductivity and consequently the time dependence of monopole density from the experimentally measured we use the following equation

$$\sigma(t) = -\frac{\chi_T}{\mu_0}\frac{d}{dt}\ln\left[1 - \frac{M(t)}{M(\infty)}\right]. \tag{5.12}$$

$M(\infty) = \chi_T H$ is calculated by integrating all of the measured monopole current data. Figure 5.2 depicts the results for time dependent conductivity for the two materials obtained from the monopole current using Eqn. 5.12. These should also be fitted to the stretched exponential form. We first show the universality plots where monopole conductivity data for both materials is plotted such that the temperature dependence of all the fit parameters is corrected for by the transformations $y = \sigma(t)/\sigma_i$ and $x = (t/\tau)^\beta$. Fig. 5.2(C,D) show that this transformation results in a very good collapse of all the data onto a straight line. This is an evidence that in these materials the conductivity itself decays with time as a stretched exponential.

We calculate the time dependent monopole density from the conductivity data using $n(T,t) = \sigma(t)/Qu$, monopole charge $Q$ is taken from [25] and we use the mobility values reported in [30]. Fig. 5.3 depicts the time dependent monopole density in the two materials. The stretching exponent and the relaxation time describing these decays are the same as those describing the time dependence

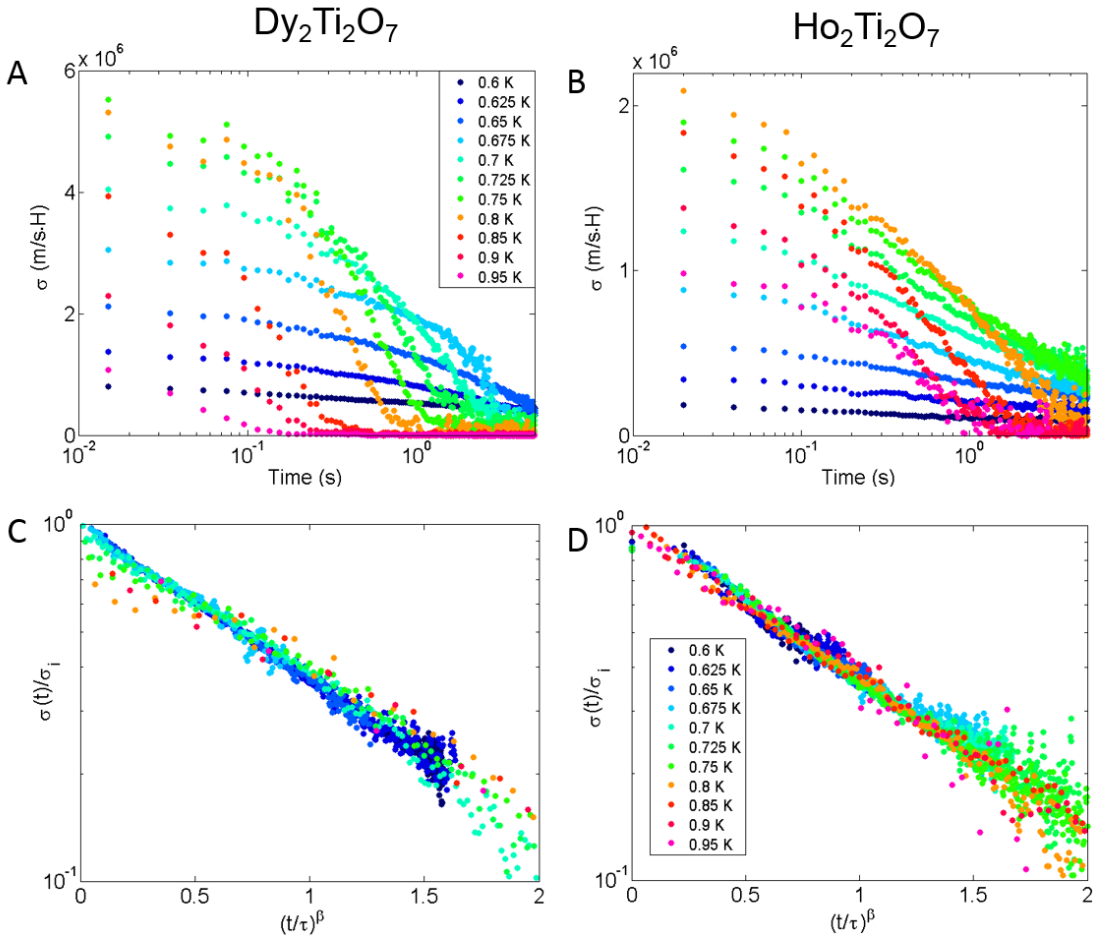


Figure 5.2: (A) Time dependent monopole conductivity after the application of external field in $Dy_2Ti_2O_7$ and (B) in $Ho_2Ti_2O_7$. The universality plots for $Dy_2Ti_2O_7$ (C) and for $Ho_2Ti_2O_7$ (D) show how the conductivity data from all temperatures and times falls onto straight line the describes the stretched exponential form.

of monopole conductivity. The initial density of the monopole that contribute to the monopole current is below 0.1% in both materials. This is quite a bit less than the density estimated from fitting the heat capacity data to Debye-Huckel theory of monopoles which gives the monopole density in the range 0.01-0.1 per rare earth spin in the temperature range of our experiments. [96] This means that not all of the thermal monopoles will contribute to the monopole current. Many of the thermally activated monopoles annihilate locally without closing an an-

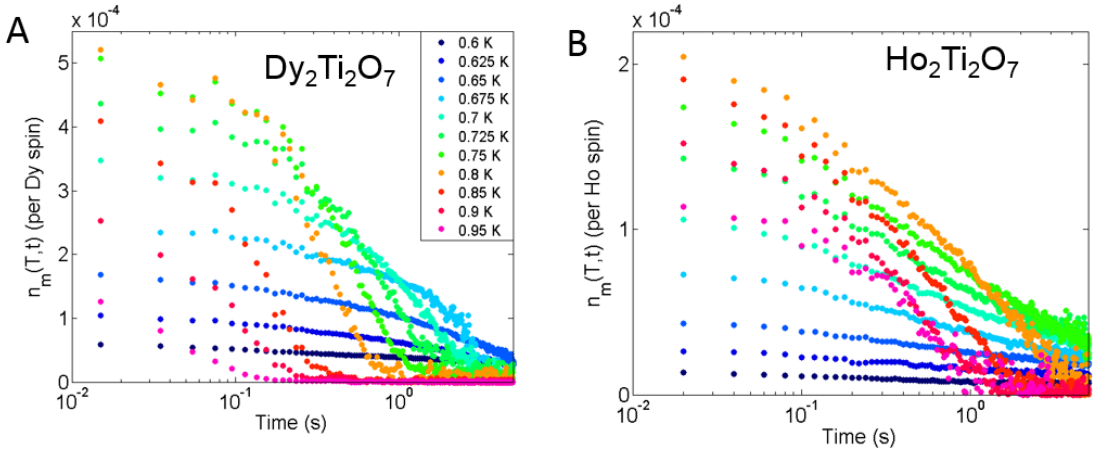


Figure 5.3: (A) Time dependent monopole density in $Dy_2Ti_2O_7$a and in $Ho_2Ti_2O_7$.

nihilation loop that travels through the whole sample, except a small fraction.

Fig. 5.4 depicts the temperature dependence of the stretching exponent obtained from fitting the time dependent conductivity data to the stretched exponential form. We see that, for the monopole liquid in both materials the low temperature value for the stretching exponent stabilizes at $\beta = 3/7$ which is the value predicted by the annihilation theory for the three dimensional system with Coulomb interactions between the monopoles. The glass transition temperature in this model is defined as the temperature at which the stretching exponent reaches this topological value. Then we deduce that the glass temperature in $Dy_2Ti_2O_7$ is lower than that in $Ho_2Ti_2O_7$. This agrees with our results from chapter 4, where we reproted that the liquid in $Dy_2Ti_2O_7$ is more fragile with slightly higher VTF temperature $T_0$ than the liquid in $Ho_2Ti_2O_7$. There is a general correlation of fragility of the liquid $D$ with the ration of glass temperature and VTF temperature $T_g/T_0$ that, in the strong liquid the two temperatures are farther apart than in the fragile liquids. [43] For this reason, the glass temperature in $Ho_2Ti_2O_7$ should be greater since it has stronger liquid than $Dy_2Ti_2O_7$.

To check the power law relation between the relaxation time and the thermal

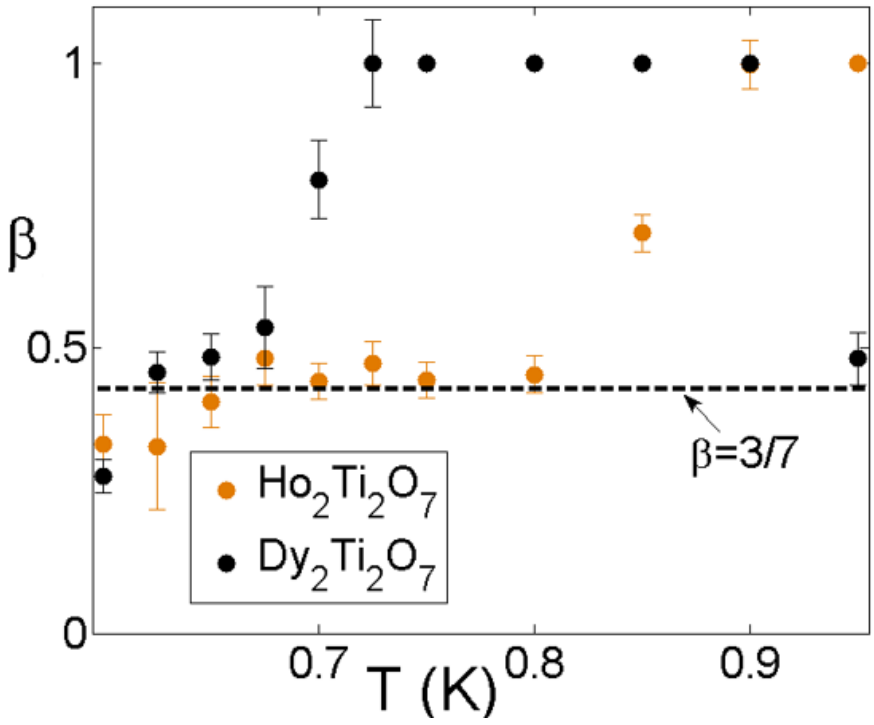


Figure 5.4: Temperature dependence of the stretching exponent used for the fits of conductivity relaxation data. For both systems, the stretching exponent stabilizes at $\beta = 3/7$, the critical value predicted by the annihilation theory, that only depends on the dimensionality of the system.

monopole density, the data obtained from fits at $T \leq 0.8$ K is plotted in Fig. 5.5. Empirically we have access to only the conducting monopole density, which is used as the horizontal axis. This data can be fit very well to a power law form with an exponent $\delta = -0.71 \pm 0.07$ a value very close to the prediction of the annihilation model $\delta$=-2/3. The fits to a power law with the exponent forced to be -2/3 also agree with the data.

The horizontal axis in this diagram is the conducting monopole density, obtained from the coefficient of the time dependent conducting monopole density, while the annihilation theory predicts the power law relation between the relaxation time and the total thermal monopole density, of both conducting and non conducting monopoles. Since we have the same power law relation of relaxation

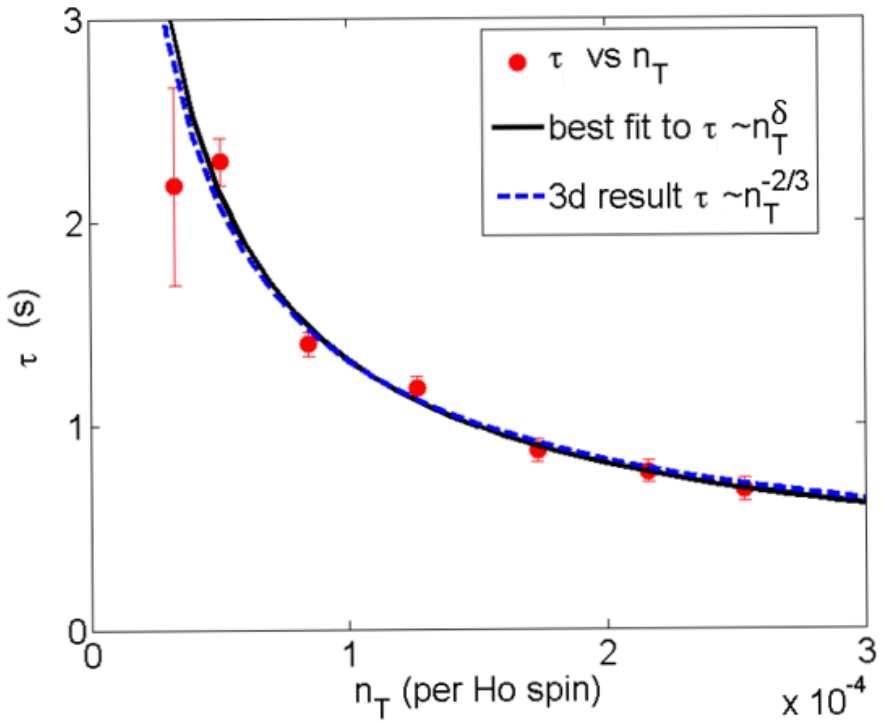


Figure 5.5: Power law relation between the relaxation time and initial conducting monopole density. Red circles are the results of the fits, black line is the fit to an unconstrained power law, and blue dashed line is the fit to a power line with exponent -2/3.

time with the conducting monopole density, we deduce that in the temperature range when the dynamics in the system is determined by the monopole annihilation, the fraction of the thermal monopoles that contribute to the current is independent of the temperature and is about 5% of the thermal monopole density. This is likely to be determined by the geometrical orientation of the crystal axes with respect to the external field applied to the sample.

CHAPTER 6

# CONCLUSION

In this work we have performed low temperature characterization of the dynamics of $Ho_2Ti_2O_7$ and $Dy_2Ti_2O_7$. Our superconducting toroidal solenoid experiments on boundary free torus shaped samples allow us to probe the magnetization dynamics of these materials, and the continuous geometry also removes the effects of the demagnetization effect. The absence of demagnetization effect removes the ambiguity of the data analysis procedure and help us concentrate on the true physics of the system.

The dynamical experiments performed on the so called spin ices, $Ho_2Ti_2O_7$ and $Dy_2Ti_2O_7$, give clear evidence that the magnetic state in these systems should be described as a glass forming liquid. The Kohlrausch-Williams-Watts stretched exponential relaxation in time domain, Havriliak-Negami form of AC susceptibility and divergence of relaxation times along Vogel-Tammann-Fulcher trajectory are dynamical indicators of glass forming liquids and all of them are observed for both magnetic systems. Additionally, the two step relaxation in the time domain which is usually observed for glassy systems [1] was also reported in the time domain characteristics of $Dy_2Ti_2O_7$ at temperatures below 0.6 K [29]. This is an intriguing result, because this is first time an analogue of viscous relaxation in supercooled liquids is observed in a magnetic system.

The VTF temperature is $T_0 \approx 257$ mK in $Dy_2Ti_2O_7$ and $T_0 \approx 191$ mK in $Ho_2Ti_2O_7$. This signifies the lowest temperature at which the system may still behave as a metastable state with higher degree of symmetry, and below this temperature the system will fall out of equilibrium. However, to realize such metastable states, wait times as large as few hundred hours must be accommodated similar to the work in [19]. The numbers for VTF temperature are very similar

for the two systems, compared to the other parameters describing the VTF fit which show large material dependence. This temperature may be determined by the dipolar interaction between the spins in the system. This is because (i) the strength of dipolar interaction is almost identical for the two systems, and (ii) Monte-Carlo studies have shows a low temperature heat capacity peak at $T \sim 200$ mK where the peak position depends only on the strength of the dipolar interaction and does not change with nearest neighbor exchange interaction. [72] This predicted heat capacity peak at low temperature can be related to the possible freezing and glass transition of the spins similar to the peak in heat capacity seen in conventional glass forming liquids [5].

The attempt frequency and the fragility show significant material dependence. We see that the quantum effects are more pronounced in $Ho_2Ti_2O_7$ $\tau_0 \approx 8 \cdot 10^{-10}$ s compared to $Dy_2Ti_2O_7$ $\tau_0 \approx 1.4 \cdot 10^{-4}$s. This is because of the Kramers vs non-Kramers nature of spins between two spins. Since Holmium in $Ho_2Ti_2O_7$ has integer spins, its energy levels are not protected by Kramers degeneracy and there are both doublet and singlet energy levels. Dysprosium ions in $Dy_2Ti_2O_7$ however have total spin $S = 15/2$. The energy levels in $Dy_2Ti_2O_7$are all Kramers doublets. The transverse fields like the dipolar interaction are more efficient in mediating quantum tunneling between ground state configurations in $Ho_2Ti_2O_7$ because the existence of singlets in the energy diagram results in matrix elements which are only quadratic in the transverse field, compared to the Kramers $Dy_2Ti_2O_7$ where the matrix elements are at least cubic in the transverse field.

We also see that the glass forming magnetic liquid in $Ho_2Ti_2O_7 D \approx 60$ is stronger than that in $Dy_2Ti_2O_7$ $D \approx 14$. This results from the effects of monopole motion, or more precisely the abundance of the monopoles. The paths of the magnetic monopoles in these systems is different from say the path of an electron

in a conductor. In the conductor, electrons can as almost free particles and can travel in any direction, and for the most part the correlation between the electrons can be excluded to explain basic conductivity properties of metals. This is because, whether a path was already taken by an electron does not make it unavailable for the next electron. Monopoles in $Ho_2Ti_2O_7$ and $Dy_2Ti_2O_7$ however have stricter requirements for their dynamics. A monopole can only move if it can flip a spin in the direction it is moving. When one monopole takes the path, the spin has now flipped, and the same path cannot be taken by the next monopole. As a result of this, different parts of the system become uncorrelated and relax as separate subsystems. The density of the monopoles then is directly related to the level of heterogeneity and hence the fragility of the magnetic liquid. The greater abundance of the monopoles in the system results in quicker evolution towards the heterogeneous state, and makes the system more fragile. The barrier for the creation of monopole pairs is lower in $Dy_2Ti_2O_7$ 5.6 K compared to that in $Ho_2Ti_2O_7$ 8.5 K. At temperatures where we perform our studies $T \leq 2K$, monopoles are more abundant in $Dy_2Ti_2O_7$ and help the magnetic liquid in $Dy_2Ti_2O_7$ become more heterogeneous and more fragile.

A model developed on the assumption of diffusing monopoles that also includes annihilation of monopoles when they encounter the antimonopoles shows success in explaining the stretched exponential decay of monopole current. This model predicts specific power law decay for the conducting monopole density and hence the monopole conductivity, and fitting the time decay of monopole density to this model shows that the stretching exponent in both materials reaches the critical value of $\beta$=3/7 at some critical temperature. This critical temperature is identified with the glass transition [38] and is higher for the monopole liquid in $Ho_2Ti_2O_7$ than in $Dy_2Ti_2O_7$. This also agrees with the

trend observed in mechanical liquids. Survey of large number of glass forming liquids was reported to show correlation between the ratio of glass temperature to VTF temperature ($T_g/T_0$) and the fragility parameter $D$. [43] The strong liquids have lower VTF temperature and usually hit glass transition at higher temperatures than the fragile liquids. We see the same trend in the supercooled liquids in $Ho_2Ti_2O_7$ and $Dy_2Ti_2O_7$. The liquid in $Dy_2Ti_2O_7$ is more fragile and has lower glass temperature than the liquid in $Ho_2Ti_2O_7$.

## 6.1 Future Work

The first thing we plan to do next is developing a magnetometry circuit based on DC SQUID (Superconducting Quantum Interference Device). SQUIDs operate based on the tunneling of Cooper pairs over insulating or metallic barriers, known as Josephson effect. In a closed circuit composed of two Josephson junctions, the critical current is a strong function of the external flux threading the circuit and changes sign if the flux going through the circuit changes by as little as half of the magnetic flux quantum $\Phi_0 = h/2e$. When tuned with appropriate external bias voltage and operated in a closed feedback cycle, SQUIDs can measure magnetic flux with sensitivity of $\sim \mu\Phi_0/\sqrt{Hz}$. This makes SQUIDs very sensitive magnetic field or magnetization probes. At low temperatures ($T < 0.5K$) in the systems that we study, the magnetization dynamics becomes so slow [19], [94] that changes in magnetization are too small to detect and the sensitivity provided by a SQUID setup becomes important if not necessary. Additionally, unlike the EMF measurements based on Faraday effect that we carry out, the signal measured by SQUID is proportional to the absolute value of magnetization. For Faraday effect based measurements experiments to be useful,

the rate of change of the magnetization with time has to be such that the EMF generated is greater than the noise level of the instrument. However, when the relaxation times of the material become as large as few hours, the signal generated in an STS circuit becomes unobservably small.

Dysprosium Germanate ($Dy_2Ge_2O_7$) and Holmium Germanate ($Ho_2Ge_2O_7$) have recently been synthesized and have similar structure as the spin ices studied in this project. [103], [104] The early characterization has shown the common properties of the other spin ices, the missing entropy between low temperature and intermediate temperature states [105] as well as the pinch points in the diffuse neutron scattering diagram [106]. It is interesting to see whether these materials will also exhibit glass forming spin liquid characteristics as is reported for their close relatives in this work. This will tie the thermodynamic spin ice phase to the dynamical glass forming spin liquid phase and will be a strong step forward in understanding such frustrated magnetic systems. Fitting the heat capacity data to spin ice model gives $J_{nn}/D_{nn} = -0.35$ for $Ho_2Ge_2O_7$ and $J_{nn}/D_{nn} = -0.73$ for $Dy_2Ge_2O_7$. [107] The ratio obtained for $Dy_2Ge_2O_7$ in particular is very close to the critical value of -0.91 predicted from den Hertog-Gingras theory [22] as the boundary between long range antiferromagnetically ordered phase and the spin ice phase. It is very interesting to see how the proximity to such a critical point will affect the glass forming liquid dynamics, whether the glass forming spin liquid dynamics is still a good description in the vicinity of a quantum critical point and whether the fragility has strong dependence on the proximity to such a critical point.

Another avenue of progress is to use the monopole theory in greater detail to explain the glass forming liquid dynamics. Including the effects of monopole correlations in the form of monopole-antimonopole annihilation showed good

agreement between the theory and data, and correct predictions for the specific exponents in the stretched exponential decay. This model should be developed further to predict the divergence of relaxation times along VTF trajectory.

## BIBLIOGRAPHY


[1] Andrea Cavagna. Supercooled liquids for pedestrians. *Physics Reports*, 476(46):51 – 124, 2009.

[2] M. D. Ediger, C. A. Angell, and Sidney R. Nagel. Supercooled liquids and glasses. *The Journal of Physical Chemistry*, 100(31):13200–13212, 1996.

[3] Ethan R. Kassner, Azar B. Eyvazov, Benjamin Pichler, Timothy J. S. Munsie, Hanna A. Dabkowska, Graeme M. Luke, and J. C. Seamus Davis. Supercooled spin liquid state in the frustrated pyrochlore dy2ti2o7. *Proceedings of the National Academy of Sciences*, 112(28):8549–8554, 2015.

[4] C. A. Angell. Formation of glasses from liquids and biopolymers. *Science*, 267(5206):1924–1935, 1995.

[5] Vassiliy Lubchenko and Peter G. Wolynes. Theory of structural glasses and supercooled liquids. *Annual Review of Physical Chemistry*, 58(1):235–266, 2007. PMID: 17067282.

[6] P. G. Debenedetti et. al. Supercooled liquids and the glass transition. *Nature*, 410:259, 2001.

[7] C.A Angell. Relaxation in liquids, polymers and plastic crystals strong/fragile patterns and problems. *Journal of Non-Crystalline Solids*, 131:13 – 31, 1991.

[8] C.A. Angell. Perspective on the glass transition. *Journal of Physics and Chemistry of Solids*, 49(8):863 – 871, 1988.

[9] J A Mydosh. Spin glasses: redux: an updated experimental/materials survey. *Reports on Progress in Physics*, 78(5):052501, 2015.

[10] J A Mydosh. *Spin glasses : an experimental introduction*. Taylor and Francis, 1 edition, 1993.

[11] V. Cannella and J. A. Mydosh. Magnetic ordering in gold-iron alloys. *Phys. Rev. B*, 6:4220–4237, Dec 1972.

[12] Shoichi Nagata, P. H. Keesom, and H. R. Harrison. Low-dc-field susceptibility of CuMn spin glass. *Phys. Rev. B*, 19:1633–1638, Feb 1979.

[13] http://www.chemtube3d.com/solidstate/SS Pyrochlore.htm. Pyrochlore. 2008-2015.

[14] Bruno Tomasello, Claudio Castelnovo, Roderich Moessner, and Jorge Quintanilla. Single-ion anisotropy and magnetic field response in the spin-ice materials $ho_2ti_2o_7$ and $dy_2ti_2o_7$. *Phys. Rev. B*, 92:155120, Oct 2015.

[15] A. P. Ramirez et. al. Zero-point entropy in 'spin ice'. *Nature*, 399:333, 1999.

[16] S. T. Bramwell, M. J. Harris, B. C. den Hertog, M. J. P. Gingras, J. S. Gardner, D. F. McMorrow, A. R. Wildes, A. L. Cornelius, J. D. M. Champion, R. G. Melko, and T. Fennell. Spin correlations in $ho_2ti_2O_7$: A dipolar spin ice system. *Phys. Rev. Lett.*, 87:047205, Jul 2001.

[17] A. L. Cornelius and J. S. Gardner. Short-range magnetic interactions in the spin-ice compound $ho_2ti_2o_7$. *Phys. Rev. B*, 64:060406, Jul 2001.

[18] Steven T. Bramwell and Michel J. P. Gingras. Spin ice state in frustrated magnetic pyrochlore materials. *Science*, 294(5546):1495–1501, 2001.

[19] D. Pomaranski et. al. Absence of paulings residual entropy in thermally equilibrated dy2ti2o7. *Nature Physics*, 9:353, 2013.

[20] M.J. Harris, S.T. Bramwell, T. Zeiske, D.F. McMorrow, and P.J.C. King. Magnetic structures of highly frustrated pyrochlores. *Journal of Magnetism and Magnetic Materials*, 177:757 – 762, 1998.

[21] R. Siddharthan, B. S. Shastry, and A. P. Ramirez. Spin ordering and partial ordering in holmium titanate and related systems. *Phys. Rev. B*, 63:184412, Apr 2001.

[22] Byron C. den Hertog and Michel J. P. Gingras. Dipolar interactions and origin of spin ice in ising pyrochlore magnets. *Phys. Rev. Lett.*, 84:3430–3433, Apr 2000.

[23] T. Fennell, P. P. Deen, A. R. Wildes, K. Schmalzl, D. Prabhakaran, A. T. Boothroyd, R. J. Aldus, D. F. McMorrow, and S. T. Bramwell. Magnetic coulomb phase in the spin ice ho2ti2o7. *Science*, 326(5951):415–417, 2009.

[24] Taras Yavors'kii, Tom Fennell, Michel J. P. Gingras, and Steven T. Bramwell. $dy_2ti_2o_7$. *Phys. Rev. Lett.*, 101:037204, Jul 2008.

[25] R Moessner C. Castelnovo and S. L. Sondhi. Magnetic monopoles in spin ice. *Nature*, 451:42, 2008.

[26] Hidekazu Aoki, Toshiro Sakakibara, Kazuyuki Matsuhira, and Zenji Hiroi. Magnetocaloric effect study on the pyrochlore spin ice compound dy2ti2o7 in a [111] magnetic field. *Journal of the Physical Society of Japan*, 73(10):2851–2856, 2004.

[27] D. Slobinsky, C. Castelnovo, R. A. Borzi, A. S. Gibbs, A. P. Mackenzie, R. Moessner, and S. A. Grigera. Unconventional magnetization processes and thermal runaway in spin-ice $dy_2ti_2o_7$. *Phys. Rev. Lett.*, 105:267205, Dec 2010.

[28] S. T. Bramwell et. al. Measurement of the charge and current of magnetic monopoles in spin ice. *Nature*, 461:956, 2009.

[29] H. M. Revell et. al. Evidence of impurity and boundary effects on magnetic monopole dynamics in spin ice. *Nature Physics*, 9:34–37, 2013.

[30] L. Bovo et. al. Brownian motion and quantum dynamics of magnetic monopoles in spin ice. *Nature Communications*, 4:2551, 2013.

[31] J. Snyder, B. G. Ueland, J. S. Slusky, H. Karunadasa, R. J. Cava, and P. Schiffer. Low-temperature spin freezing in the $dy_2ti_2o_7$ spin ice. *Phys. Rev. B*, 69:064414, Feb 2004.

[32] L. D. C. Jaubert et. al. Signature of magnetic monopole and dirac string dynamics in spin ice. *Nature Physics*, 5:258, 2009.

[33] Frank Pobell. *Matter and Methods at Low Temperatures*, volume 1. Springer, 2007.

[34] David Turnbull. Under what conditions can a glass be formed? *Contemporary Physics*, 10(5):473–488, 1969.

[35] D. Turnbull and J. C. Fisher. Rate of nucleation in condensed systems. *The Journal of Chemical Physics*, 17(1):71–73, 1949.

[36] Michael C Weinberg, W.Howard Poisl, and Laszlo Granasy. Crystal growth and classical nucleation theory. *Comptes Rendus Chimie*, 5(11):765 – 771, 2002.

[37] Walter. Kauzmann. The nature of the glassy state and the behavior of liquids at low temperatures. *Chemical Reviews*, 43(2):219–256, 1948.

[38] J C Phillips. Stretched exponential relaxation in molecular and electronic glasses. *Reports on Progress in Physics*, 59(9):1133, 1996.

[39] Graham Williams and David C. Watts. Non-symmetrical dielectric relaxation behaviour arising from a simple empirical decay function. *Trans. Faraday Soc.*, 66:80–85, 1970.

[40] Kenneth S. Cole and Robert H. Cole. Dispersion and absorption in dielectrics i. alternating current characteristics. *The Journal of Chemical Physics*, 9(4):341–351, 1941.

[41] S. Havriliak and S. Negami. A complex plane representation of dielectric and mechanical relaxation processes in some polymers. *Polymer*, 8:161 – 210, 1967.

[42] F. Alvarez, A. Alegra, and J. Colmenero. Relationship between the time-domain kohlrausch-williams-watts and frequency-domain havriliak-negami relaxation functions. *Phys. Rev. B*, 44:7306–7312, Oct 1991.

[43] C.A Angell. Entropy and fragility in supercooling liquids. *Journal of Research of the National Institute of Standards and Technology*, 102:171 – 185, 1997.

[44] Gerold Adam and Julian H. Gibbs. On the temperature dependence of cooperative relaxation properties in glassforming liquids. *The Journal of Chemical Physics*, 43(1):139–146, 1965.

[45] Gene F. Mazenko and Joonhyun Yeo. Density nonlinearities and a field theory for the dynamics of simple fluids. *Journal of Statistical Physics*, 74(5):1017–1032, 1994.

[46] N. J. Tao, G. Li, and H. Z. Cummins. Self-similar light-scattering spectra of $\beta$ relaxation near the liquid-glass transition. *Phys. Rev. Lett.*, 66:1334–1337, Mar 1991.

[47] F. Mezei, W. Knaak, and B. Farago. Neutron spin echo study of dynamic correlations near the liquid-glass transition. *Phys. Rev. Lett.*, 58:571–574, Feb 1987.

[48] T. R. Kirkpatrick, D. Thirumalai, and P. G. Wolynes. Scaling concepts for the dynamics of viscous liquids near an ideal glassy state. *Phys. Rev. A*, 40:1045–1054, Jul 1989.

[49] T. R. Kirkpatrick and P. G. Wolynes. Connections between some kinetic and equilibrium theories of the glass transition. *Phys. Rev. A*, 35:3072–3080, Apr 1987.

[50] V K Anand, D A Tennant, and B Lake. Investigations of the effect of nonmagnetic ca substitution for magnetic dy on spin-freezing in dy 2 ti 2 o 7. *Journal of Physics: Condensed Matter*, 27(43):436001, 2015.

[51] Hui Liu, Youming Zou, Lei Zhang, Langsheng Ling, Hongyan Yu, Lei He, Changjin Zhang, and Yuheng Zhang. Magnetic order and dynamical properties of the spin-frustrated magnet dy2xybxti2o7. *Journal of Magnetism and Magnetic Materials*, 349:173 – 179, 2014.

[52] Hui Liu, Youming Zou, Langsheng Ling, Lei Zhang, Changjin Zhang, and Yuheng Zhang. Enhanced ferromagnetism and emergence of spin-glass-like transition in pyrochlore compound dy2ti2xvxo7. *Journal of Magnetism and Magnetic Materials*, 388:135 – 142, 2015.

[53] J. Matt Farmer, Lynn A. Boatner, Bryan C. Chakoumakos, Mao-Hua Du, Michael J. Lance, Claudia J. Rawn, and Jeff C. Bryan. Structural and crystal chemical properties of rare-earth titanate pyrochlores. *Journal of Alloys and Compounds*, 605:63 – 70, 2014.

[54] Jason S. Gardner, Michel J. P. Gingras, and John E. Greedan. Magnetic pyrochlore oxides. *Rev. Mod. Phys.*, 82:53–107, Jan 2010.

[55] H. Van Kempen, A.R. Miedema, and W.J. Huiskamp. Heat capacities of the metals terbium and holmium below 1k. *Physica*, 30(1):229 – 236, 1964.

[56] Dennis J. Flood. Magnetization and magnetic entropy of dy2ti2o7. *Journal of Applied Physics*, 45(9):4041–4044, 1974.

[57] G. Brunhart, H. Postma, and V. L. Sailor. Determination of spins of neutron resonances and the hyperfine coupling constant in $ho^{165}$. *Phys. Rev.*, 137:B1484–B1490, Mar 1965.

[58] D. Liu, L. Lin, M. F. Liu, Z. B. Yan, S. Dong, and J.-M. Liu. Multiferroicity

in spin ice ho2ti2o7: An investigation on single crystals. *Journal of Applied Physics*, 113(17):17D901, 2013.

[59] L. Lin, Y. L. Xie, Z. Y. Zhao, J. J. Wen, Z. B. Yan, S. Dong, and J.-M. Liu. Enhanced magnetism-generated ferroelectricity in highly frustrated fe-doped ho2ti2o7. *Journal of Applied Physics*, 117(17):17D915, 2015.

[60] C. P. Grams et. al. Critical speeding-up in the magnetoelectric response of spin-ice near its monopole liquidgas transition. *Nature Communications*, 5:4853, 2014.

[61] L Lin, Y L Xie, J-J Wen, S Dong, Z B Yan, and J-M Liu. Experimental observation of magnetoelectricity in spin ice dy 2 ti 2 o 7. *New Journal of Physics*, 17(12):123018, 2015.

[62] T. Katsufuji and H. Takagi. Magnetocapacitance and spin fluctuations in the geometrically frustrated magnets $R_2ti_2o_7$ ($r$ = rareearth). *Phys. Rev. B*, 69:064422, Feb 2004.

[63] L D C Jaubert and P C W Holdsworth. Magnetic monopole dynamics in spin ice. *Journal of Physics: Condensed Matter*, 23(16):164222, 2011.

[64] S. Rosenkranz, A. P. Ramirez, A. Hayashi, R. J. Cava, R. Siddharthan, and B. S. Shastry. Crystal-field interaction in the pyrochlore magnet ho2ti2o7. *Journal of Applied Physics*, 87(9):5914–5916, 2000.

[65] Y. M. Jana and D. Ghosh. Crystal-field studies of magnetic susceptibility, hyperfine, and specific heat properties of a $ho_2ti_2o_7$ single crystal. *Phys. Rev. B*, 61:9657–9664, Apr 2000.

[66] Y.M. Jana, A. Sengupta, and D. Ghosh. Estimation of single ion anisotropy in pyrochlore dy2ti2o7, a geometrically frustrated system, using crystal field theory. *Journal of Magnetism and Magnetic Materials*, 248(1):7 – 18, 2002.

[67] G. Ehlers, E. Mamontov, M. Zamponi, K. C. Kam, and J. S. Gardner. Direct observation of a nuclear spin excitation in $ho_2ti_2\mathbf{o}_7$. *Phys. Rev. Lett.*, 102:016405, Jan 2009.

[68] Linus Pauling. The structure and entropy of ice and of other crystals with some randomness of atomic arrangement. *Journal of the American Chemical Society*, 57(12):2680–2684, 1935.

[69] J. D. Bernal and R. H. Fowler. A theory of water and ionic solution, with particular reference to hydrogen and hydroxyl ions. *The Journal of Chemical Physics*, 1(8):515–548, 1933.

[70] J.F. Nagle. Theory of the dielectric constant of ice. *Chemical Physics*, 43(3):317 – 328, 1979.

[71] D. J. Adams. Theory of the dielectric constant of ice. *Nature*, 193:447, 1981.

[72] Roger G. Melko, Byron C. den Hertog, and Michel J. P. Gingras. Long-range order at low temperatures in dipolar spin ice. *Phys. Rev. Lett.*, 87:067203, Jul 2001.

[73] P. W. Anderson. Ordering and antiferromagnetism in ferrites. *Phys. Rev.*, 102:1008–1013, May 1956.

[74] M. J. Harris, S. T. Bramwell, D. F. McMorrow, T. Zeiske, and K. W. Godfrey. Geometrical frustration in the ferromagnetic pyrochlore $ho_2ti_2O_7$. *Phys. Rev. Lett.*, 79:2554–2557, Sep 1997.

[75] T. Fennell, O. A. Petrenko, B. Fk, J. S. Gardner, S. T. Bramwell, and B. Ouladdiaf. Neutron scattering studies of the spin ices $ho_2ti_2o_7$ and $dy_2ti_2o_7$ in applied magnetic field. *Phys. Rev. B*, 72:224411, Dec 2005.

[76] M JP Gingras and B C den Hertog. Origin of spin-ice behavior in ising pyrochlore magnets with long-range dipole interactions: an insight from mean-field theory. *Canadian Journal of Physics*, 79(11-12):1339–1351, 2001.

[77] Christopher L. Henley. Order by disorder and gaugelike degeneracy in a quantum pyrochlore antiferromagnet. *Phys. Rev. Lett.*, 96:047201, Jan 2006.

[78] S. V. Isakov, R. Moessner, and S. L. Sondhi. Why spin ice obeys the ice rules. *Phys. Rev. Lett.*, 95:217201, Nov 2005.

[79] Frederic Mila Claudine Lacroix, Phillippe Mendels. *Introduction to Frustrated Magnetism*, volume 1 of *164*. Springer, 1 edition, 2011.

[80] L. E. Bove, S. Klotz, A. Paciaroni, and F. Sacchetti. Anomalous proton dynamics in ice at low temperatures. *Phys. Rev. Lett.*, 103:165901, Oct 2009.

[81] P. A. M. Dirac. Quantised singularities in the electromagnetic field. *Pro-*

*ceedings of the Royal Society of London A: Mathematical, Physical and Engineering Sciences*, 133(821):60–72, 1931.

[82] Blas Cabrera. First results from a superconductive detector for moving magnetic monopoles. *Phys. Rev. Lett.*, 48:1378–1381, May 1982.

[83] Anna Palau, Sergio Valencia, Nuria Del-Valle, Carles Navau, Matteo Cialone, Ashima Arora, Florian Kronast, D. Alan Tennant, Xavier Obradors, Alvaro Sanchez, and Teresa Puig. Encoding magnetic states in monopole-like configurations using superconducting dots. *Advanced Science*, 3(11):1600207–n/a, 2016. 1600207.

[84] Xiao-Liang Qi, Rundong Li, Jiadong Zang, and Shou-Cheng Zhang. Inducing a magnetic monopole with topological surface states. *Science*, 323(5918):1184–1187, 2009.

[85] D. I. Khomskii. Magnetic monopoles and unusual dynamics of magnetoelectrics. *Nature Communications*, 5:4793, 2014.

[86] G. J. Conduit. Line of dirac monopoles embedded in a bose-einstein condensate. *Phys. Rev. A*, 86:021605, Aug 2012.

[87] M. W. Ray et. al. Observation of dirac monopoles in a synthetic magnetic field. *Nature*, 505:657, 2014.

[88] I. A. Ryzhkin. Magnetic relaxation in rare-earth oxide pyrochlores. *Journal of Experimental and Theoretical Physics*, 101(3):481–486, 2005.

[89] L. J. Chang et. al. Low-temperature muon spin rotation studies of the monopole charges and currents in y doped ho2ti2o7. *Scientific Reports*, 3:1881, 2013.

[90] S. R. Dunsiger, A. A. Aczel, C. Arguello, H. Dabkowska, A. Dabkowski, M.-H. Du, T. Goko, B. Javanparast, T. Lin, F. L. Ning, H. M. L. Noad, D. J. Singh, T. J. Williams, Y. J. Uemura, M. J. P. Gingras, and G. M. Luke. Spin ice: Magnetic excitations without monopole signatures using muon spin rotation. *Phys. Rev. Lett.*, 107:207207, Nov 2011.

[91] Stephen J. Blundell. Monopoles, magnetricity, and the stray field from spin ice. *Phys. Rev. Lett.*, 108:147601, Apr 2012.

[92] C. Jaccard. Thermodynamics of irreversible processes applied to ice. *Physik der kondensierten Materie*, 3(2):99–118, 1964.

[93] Steven T. Bramwell. Generalized longitudinal susceptibility for magnetic monopoles in spin ice. *Philosophical Transactions of the Royal Society of London A: Mathematical, Physical and Engineering Sciences*, 370(1981):5738–5766, 2012.

[94] L. R. Yaraskavitch, H. M. Revell, S. Meng, K. A. Ross, H. M. L. Noad, H. A. Dabkowska, B. D. Gaulin, and J. B. Kycia. Spin dynamics in the frozen state of the dipolar spin ice material $dy_2ti_2o_7$. *Phys. Rev. B*, 85:020410, Jan 2012.

[95] Hiroshi Takatsu, Kazuki Goto, Hiromi Otsuka, Ryuji Higashinaka, Kazuyuki Matsubayashi, Yoshiya Uwatoko, and Hiroaki Kadowaki. Ac susceptibility of the dipolar spin ice dy2ti2o7: Experiments and monte carlo simulations. *Journal of the Physical Society of Japan*, 82(10):104710, 2013.

[96] C. Castelnovo, R. Moessner, and S. L. Sondhi. Debye-hückel theory for spin ice at low temperature. *Phys. Rev. B*, 84:144435, Oct 2011.

[97] S. R. Giblin et. al. Creation and measurement of long-lived magnetic monopole currents in spin ice. *Nature Physics*, 7:252, 2011.

[98] Kazuyuki Matsuhira, Carley Paulsen, Elsa Lhotel, Chihiro Sekine, Zenji Hiroi, and Seishi Takagi. Spin dynamics at very low temperature in spin ice dy2ti2o7. *Journal of the Physical Society of Japan*, 80(12):123711, 2011.

[99] J. A. Quilliam, L. R. Yaraskavitch, H. A. Dabkowska, B. D. Gaulin, and J. B. Kycia. Dynamics of the magnetic susceptibility deep in the coulomb phase of the dipolar spin ice material $ho_2ti_2o_7$. *Phys. Rev. B*, 83:094424, Mar 2011.

[100] Hui Liu, Youming Zou, Langsheng Ling, Lei Zhang, Wei Tong, Changjin Zhang, and Yuheng Zhang. Frustrated magnetism and dynamical properties in pyrochlore-type magnet dy2ti2xfexo7. *Journal of Magnetism and Magnetic Materials*, 369:107 – 113, 2014.

[101] J. P. Clancy, J. P. C. Ruff, S. R. Dunsiger, Y. Zhao, H. A. Dabkowska, J. S. Gardner, Y. Qiu, J. R. D. Copley, T. Jenkins, and B. D. Gaulin. Revisiting static and dynamic spin-ice correlations in $ho_2ti_2o_7$ with neutron scattering. *Phys. Rev. B*, 79:014408, Jan 2009.

[102] K Matsuhira, Y Hinatsu, K Tenya, and T Sakakibara. Low temperature magnetic properties of frustrated pyrochlore ferromagnets ho 2 sn 2 o 7 and ho 2 ti 2 o 7. *Journal of Physics: Condensed Matter*, 12(40):L649, 2000.

[103] E. Morosan, J. A. Fleitman, Q. Huang, J. W. Lynn, Y. Chen, X. Ke, M. L. Dahlberg, P. Schiffer, C. R. Craley, and R. J. Cava. Structure and magnetic properties of the $ho_2ge_2o_7$ pyrogermanate. *Phys. Rev. B*, 77:224423, Jun 2008.

[104] X. Ke, M. L. Dahlberg, E. Morosan, J. A. Fleitman, R. J. Cava, and P. Schiffer. Magnetothermodynamics of the ising antiferromagnet $dy_2ge_2o_7$. *Phys. Rev. B*, 78:104411, Sep 2008.

[105] H. D. Zhou et. al. High pressure route to generate magnetic monopole dimers in spin ice. *Nature Communications*, 2:1483, 2011.

[106] A. M. Hallas, J. A. M. Paddison, H. J. Silverstein, A. L. Goodwin, J. R. Stewart, A. R. Wildes, J. G. Cheng, J. S. Zhou, J. B. Goodenough, E. S. Choi, G. Ehlers, J. S. Gardner, C. R. Wiebe, and H. D. Zhou. Statics and dynamics of the highly correlated spin ice $ho_2ge_2o_7$. *Phys. Rev. B*, 86:134431, Oct 2012.

[107] H. D. Zhou, J. G. Cheng, A. M. Hallas, C. R. Wiebe, G. Li, L. Balicas, J. S. Zhou, J. B. Goodenough, J. S. Gardner, and E. S. Choi. Chemical pressure effects on pyrochlore spin ice. *Phys. Rev. Lett.*, 108:207206, May 2012.

[108] A. Farhan et. al. Thermodynamics of emergent magnetic charge screening in artificial spin ice. *Nature Communications*, 7:12635, 2016.

[109] Peter Grassberger and Itamar Procaccia. The long time properties of diffusion in a medium with static traps. *The Journal of Chemical Physics*, 77(12):6281–6284, 1982.